

ISOGEOMETRIC ANALYSIS AND PATCHWISE REPRODUCING
POLYNOMIAL PARTICLE METHOD FOR PLATES

by

Hyunju Kim

A dissertation submitted to the faculty of
The University of North Carolina at Charlotte
in partial fulfillment of the requirements
for the degree of Doctor of Philosophy in
Applied Mathematics

Charlotte

2013

Approved by:

Dr. Hae-Soo Oh

Dr. Wei Cai

Dr. Stanislav Molchanov

Dr. Jim Bowen

© 2013
Hyunju Kim
ALL RIGHTS RESERVED

ABSTRACT

HYUNJU KIM. Isogeometric Analysis and Patchwise Reproducing Polynomial Particle Method for Plates.

(Under the direction of DR. HAE-SOO OH)

Isogeometric analysis (IGA) ([8, 16, 27]) is designed to combine two tasks, design by Computer Aided Design (CAD) and Finite Element Analysis (FEA), so that it drastically reduces the error in the representation of the computational domain and the re-meshing by the use of “exact” CAD geometry directed at the coarsest level of discretization. This is achieved by using B-splines or non-uniform rational B-splines (NURBS) for the description of geometries as well as for the representation of unknown solution fields.

In order to handle the singularities arising in the PDEs, Babuška and Oh [7] introduced mapping techniques, called the Method of Auxiliary Mapping (MAM), into conventional p -version of Finite Element Methods (FEM). In a similar spirit to MAM, it is possible to construct a novel NURBS geometrical mapping that generates singular functions resembling the singularities. The proposed mapping technique is concerned with constructions of unconventional novel geometrical mappings by which push-forward of B-spline functions defined on the parameter space generates singular functions in a physical domain that resemble the given point singularities. In other words, the pull-back of the singularity into the parameter space by the non standard NURBS mapping becomes highly smooth.

However, the mapping technique is not able to handle in the framework of IGA. Thus, we consider how to use the proposed mapping method in IGA of elliptic problems and elasticity containing singularities without changing the design mapping. For this end, we embed the mapping method into the standard IGA that uses NURBS basis functions for which $h-p-k$ -refinements are applicable for improved computa-

tional solution. In other words, the mapping method will be used to enrich NURBS basis functions around neighborhood of singularities so that they can capture singular behaviors of the solution to be approximated.

Finally, Reproducing Polynomial Particle Method (RPPM) is one of meshless methods that use meshes minimally or do not use meshes at all. In this dissertation, the RPPM is employed for free vibration and buckling of the first order shear deformation model (FSDT), called the Reissner-Mindlin plate, and for analysis of boundary layer of the Reissner-Mindlin plate. For numerical implementation, we use flat-top partition of unity functions, introduced by Oh et al, and patchwise RPPM in which approximation functions have high order polynomial reproducing property and shape functions satisfying the Kronecker delta property. Also, we demonstrate that our method is more effective than other existing methods in dealing with Reissner-Mindlin plates with various material properties and boundary conditions.

DEDICATION

To my loving family

ACKNOWLEDGMENTS

I would like to express my sincere gratitude and appreciation to my advisor, Dr. Hae-Soo Oh, for his guidance, and for ensuring financial support throughout my studies. He was not only a great teacher but also a wonderful mentor, and model. Without his encouragement and guidance this dissertation would not have materialized. I am also grateful to the members of my committee for taking the time to guide me through my dissertation. Especially I would like to express special thanks to Dr. Stanislav Molchanov who showed me the beauty of applied probability and for his insightful remarks, and valuable comments. I am also grateful to Dr. Wei Cai who taught me the theory of electromagnetic. Dr. Jim Bowen has generously given his time and expertise to better my work. I wish to express my profound thanks to my wife Haesun Lee for her selfless sacrifices that they made in allowing me to pursue my education. Also, there is no question about that my kids Esther Yerim, Joshua Yejun, and Ariel Yein who are the most beloved God's presents, made me to complete the study. Special thanks goes to Dr. Jae Woo Jeong and Dr. Bongsoo Jang for vastly advising me about research. Also, I thank Pastor Paul Cho, his wife Grace Lee, and his whole family, for providing a constant source of encouragement and support, and for their prayer.

TABLE OF CONTENTS

LIST OF FIGURES	x
LIST OF TABLES	xvii
CHAPTER 1: INTRODUCTION	1
CHAPTER 2: PRELIMINARIES	7
2.1 B-splines and NURBS	7
2.1.1 B-splines	7
2.1.2 NURBS	11
2.1.3 Perspective Map	13
2.2 Refinement	16
2.2.1 Knot Insertion	16
2.2.2 Degree Elevation	17
2.2.3 Degree and continuity elevation: k -refinement	22
2.3 Closed-form Partition of Unity with flat-top	24
2.3.1 Partition of Unity with flat-top in one-dimension	28
2.4 Weak solution in Sobolev space	30
2.5 Elasticity	31
CHAPTER 3: MAPPING TECHNIQUES FOR IGA	34
3.1 NURBS geometrical mappings by which push-forward of B-spline functions generate singular functions	34
3.1.1 Mapping methods to handle singularities	34
3.1.2 Error estimates	39
3.2 Numerical tests	41
3.2.1 The wedge shaped plates	41
3.2.2 The curved domain	43
3.2.3 The single edge cracked elastic domain	46

CHAPTER 4: ENRICHMENT OF NURBS BASIS FUNCTIONS FOR IGA	53
4.1 Enrichment of NURBS for IGA with singular functions generated by NURBS geometric mapping	53
4.2 Numerical tests	62
4.2.1 The Motz problem	63
4.2.2 The cracked unit disk	68
4.2.3 The L -shaped domain	70
4.3 Blending NURBS and B-splines through Partition of Unity (PU) with flat-top	72
4.3.1 Two dimensional Partition of Unity with flat-top	72
4.3.2 A design of a singular mapping that maps onto a neighborhood of a crack	74
4.3.3 Numerical test	82
CHAPTER 5: PATCHWISE RPPM FOR THICK PLATES	86
5.1 Formulations for free vibration and buckling	86
5.1.1 Governing equations and variational formulation of Reissner- Mindlin plates	86
5.1.2 Patchwise RPP approximation form	88
5.2 Numerical results	92
5.2.1 A square Reissner-Mindlin plate in bending	92
5.2.2 Reissner-Mindlin plates in free vibration and buckling	93
5.3 Reissner-Mindlin plate with boundary layer	101
5.3.1 Reissner-Mindlin Model with Boundary Layer on semi-infinite Plate	101
CHAPTER 6: CONCLUDING REMARKS AND FUTURE CHALLENGES	106
REFERENCES	109
APPENDIX A: TABLES OF NUMERICAL DATA	114

A.1	Numerical data (Tables A.1, A.2, A.3) for relative errors of the Motz problem shown in Fig. 4.3	114
A.2	Numerical data (Tables A.4, A.5, A.6) for relative errors of the Laplace equation in the cracked unit disk shown in Fig. 4.9	114
A.3	Numerical data (Tables A.7, A.8, A.9) for relative errors of the elasticity equation in the L -shaped domain shown in Fig. 4.11	114
APPENDIX B: FIGURES OF NUMERICAL DATA		120
B.1	The wedge-shaped domain in Example 3.2.1	120
APPENDIX C: TABLES OF CONTROL POINTS AND WEIGHTS		123
C.1	The wedge-shaped domain in Example 3.2.1	123
C.2	The curved domain in Example 3.2.2	123
C.3	The single edge cracked domain in Example 3.2.3	123

LIST OF FIGURES

FIGURE 2.1: B-spline functions $N_{i,3}(\xi)$, $i = 1, 2, \dots, 7$ of order $k = 3$ corresponding to the knot vector $\Xi = \{0, 0, 0, 0.3, 0.3, 0.5, 0.6, 1, 1, 1\}$. 8

FIGURE 2.2: (a) B-spline curve and control points on the open knot vector $\{0, 0, 0, 0.25, 0.6, 0.8, 0.8, 1, 1, 1\}$. (b) B-spline functions corresponding to the B-spline curve shown in (a). 10

(a) B-spline curve and control points 10

(b) B-spline basis functions 10

FIGURE 2.3: (a) A quadratic curve on the knot vector $\Xi = \{0, 0, 0, 0.1, 0.2, 0.3, 0.4, 0.5, 0.6, 0.7, 0.8, 0.9, 1, 1, 1\}$. (b) A 11th degree B-spline curve using the same control points with (a) defined on $\Xi = \{0, 0, 0, 0, 0, 0, 0, 0, 0, 0, 0, 1, 1, 1, 1, 1, 1, 1, 1, 1, 1, 1, 1\}$ 12

(a) quadratic B-spline curve 12

(b) 11th degree B-spline curve 12

FIGURE 2.4: B-spline surface and control net 13

FIGURE 2.5: NURBS surface of prow in a ship and control net 14

FIGURE 2.6: A representation of Euclidean points on the hyperplane $W = 1$ through the perspective map H 15

FIGURE 2.7: (a) The initial quadratic B-spline basis functions corresponding the open knot vector $\Xi = \{0, 0, 0, 1, 1, 1\}$. (b) Quadratic B-spline basis functions after knot insertion, corresponding the open knot vector $\bar{\Xi} = \{0, 0, 0, 0.3, 0.6, 1, 1, 1\}$ 18

(a) Initial quadratic B-spline basis functions 18

(b) Quadratic B-spline basis functions after knot insertion 18

FIGURE 2.8:	(a) The initial quadratic B-spline basis functions corresponding the open knot vector $\Xi = \{0, 0, 0, 1, 1, 1\}$.	
	(b) Quartic B-spline basis functions after degree elevation of the quadratic B-spline basis functions, corresponding the open knot vector $\bar{\Xi} = \{0, 0, 0, 0, 0, 1, 1, 1, 1, 1\}$	19
(a)	Initial quadratic B-spline basis functions	19
(b)	Quartic B-spline basis functions after degree elevation	19
FIGURE 2.9:	(a) The initial quadratic B-spline basis functions corresponding the open knot vector $\Xi = \{0, 0, 0, 1, 1, 1\}$.	
	(b) Quartic B-spline basis functions after k -refinement of the quadratic B-spline basis functions, corresponding the open knot vector $\bar{\Xi} = \{0, 0, 0, 0, 0, 0.3, 0.6, 1, 1, 1, 1, 1\}$	23
(a)	Initial quadratic B-spline basis functions	23
(b)	Quartic B-spline basis functions after k -refinement	23
FIGURE 2.10:	k -refinement versus p -refinement strategy (a) Starting with one Bézier segment, (b) & (d) Classic p -refinement strategy: (b) knot insertion is performed first to create many low-order Bézier segments. (d) Subsequent order elevation will preserve the C^0 -continuity across Bézier segment boundaries. (c) & (e) New k -refinement strategy: (c) order elevation is performed on the coarsest discretization. (e) Subsequent knot insertion will result in a basis which is C^{p-1} across the newly created segment boundaries.	25
(a)	$\Xi = \{0, 0, 1, 1\}$, $p = 1$	25
(b)	Knot insertion, $\Xi = \{0, 0, 0.2, 0.4, 0.6, 0.8, 1, 1\}$, $p = 1$	25
(c)	Order elevation: 1st step in k -refinement process, $\Xi = \{0, 0, 0, 0, 1, 1, 1, 1\}$, $p = 3$	25

(d) Order elevation, $\Xi = \{0, 0, 0, 0, 0.2, 0.2, 0.2, 0.4, 0.4, 0.4, 0.6, 0.6, 0.6, 0.8, 0.8, 0.8, 1, 1, 1, 1\}$, $p = 3$ 25

(e) Knot insertion: 2nd step in k -refinement process, $\Xi = \{0, 0, 0, 0, 0.2, 0.4, 0.6, 0.8, 1, 1, 1, 1\}$, $p = 3$ 25

FIGURE 3.1: The parameter space and the physical domain for the NURBS mapping \mathbf{F} . 39

FIGURE 3.2: (a) The relative errors in the energy norm $\times 100$ versus the h -sizes with $p_\xi = 2$ fixed. (b) The relative errors in the energy norm $\times 100$ versus polynomial degree p_ξ (number of degrees of freedom) with $h = 1/2$ fixed. 44

(a) Rel error in energy norm vs h -size: 44

(b) Rel error in energy norm vs polynomial degree: 44

FIGURE 3.3: The control points for the wedge-shaped domain. 45

FIGURE 3.4: Curved physical domain and control net 46

FIGURE 3.5: (a) The relative error (%) in the maximum norm and L_2 -norm of computed displacement field $\{u, v\}^T$ of the elasticity (3.18) in curved domain. (b) The relative error (%) in the maximum norm of computed stress field $\{\sigma_x, \sigma_y, \tau_{xy}\}^T$ of the elasticity (3.18) in curved domain. 47

(a) Rel. error of the u and v in curved domain 47

(b) Rel. error of the σ_x , σ_y , and τ_{xy} in curved domain 47

FIGURE 3.6: The relative error (%) in the strain energy norm of computed displacement field $\{u, v\}^T$ of the elasticity (3.18) in curved domain. 48

FIGURE 3.7: (a) The physical domain and control points of the single edge cracked elastic domain (b) The relative error in the maximum norm for stress field and energy norm versus number of degrees of freedom of computed solutions of the equation of elasticity in the single edge cracked domain Ω . 51

(a) plane stress plate with single edge crack and control points . . . 51

(b) Relative error (%) in max-norm and energy norm 51

FIGURE 4.1: \mathbf{G} is a design mapping and $\mathbf{F}_k, k = 0, 1, 2$, are the singular geometrical mappings for the enrichment to capture corner singularities. 54

FIGURE 4.2: The NURBS geometrical mapping that generates singular functions on $\Omega_0 = [0, r_0] \times [0, 3/2\pi]$ from the parameter space $\hat{\Omega}_0 = [0, 1] \times [0, 1]$ to the singular zone Ω_0 . Note that μ is fixed real number with $0.5 \leq \mu \leq 0.9$. 56

FIGURE 4.3: Relative errors (%) of the Motz problem in L_∞, L_2 , and energy norms: (a) Enriched IGA (solid lines) and un-enriched IGA (dotted lines); (b) Enriched IGA (solid lines) and IGA with 5-radical mesh (dotted lines). 64

(a) Rel errors (%) of enriched IGA (solid lines), IGA with no enrichment (dotted lines) 64

(b) Rel errors (%) of enriched IGA (solid lines), IGA with 5-radical mesh (dotted lines) 64

FIGURE 4.4: (a) The 5-radical mesh for the Motz problem, (b) The 5-radical mesh for the Laplace equation in the cracked unit disk and (c) The 5-radical mesh for the Laplace equation in the L -shaped domain. 65

(a) Motz problem 65

(b) Unit circle 65

(c) L -shaped domain 65

FIGURE 4.5: Condition numbers of constrained Stiffness matrices for IGA, enriched IGA, and IGA with radical mesh, respectively. 66

FIGURE 4.6: Diagram of the Enriched area for Motz problem and control points. 66

FIGURE 4.7: The domain of the Motz problem and boundary conditions. Here $g = u$ and $h = \frac{\partial u}{\partial n}$. 67

FIGURE 4.8: Diagram of the Enriched area for the cracked unit disk and control points. 68

FIGURE 4.9: Relative errors (%) of the computed solutions of the Laplace equation in the cracked unit disk in L_∞, L_2 , and energy norms: (a) Enriched IGA (solid lines) and un-enriched IGA (dotted lines); (b) Enriched IGA (solid lines) and IGA with 5-radical mesh [66] (dotted lines). 70

(a) Rel errors (%) of enriched IGA (solid lines), IGA without enrichment (dotted lines) 70

(b) Rel errors (%) of enriched IGA (solid lines), IGA with 5-radical mesh (dotted lines) 70

FIGURE 4.10: Diagram of the Enriched area for the L -shaped domain and control points 71

FIGURE 4.11: Relative errors (%) of the computed solutions of the Laplace equation in the L -shaped domain in L_∞, L_2 , and energy norms: (a) Enriched IGA (solid lines) and un-enriched IGA (dotted lines); (b) Enriched IGA (solid lines) and IGA with 5-radical mesh [66] (dotted lines) 73

(a)	Rel errors (%) of enriched IGA (solid lines), IGA without enrichment (dotted lines)	73
(b)	Rel errors (%) of enriched IGA (solid lines), IGA with 5-radical mesh (dotted lines)	73

FIGURE 4.12: (a) An examples of PU functions with flat-top $\hat{\Psi}^{in}$ and (b) $\hat{\Psi}^{out}$ in the domain shown in Fig. 4.16 with $b = 1$ 75

(a)	An example of PU function $\hat{\Psi}^{in}$	75
(b)	An example of PU function $\hat{\Psi}^{out}$	75

FIGURE 4.13: Integral areas of the PU function $\hat{\Psi}^{in}$ on the singular zone 77

FIGURE 4.14: An example of $\hat{Q}_{\mathbf{G},k}^{nft}$ for given $Q_{\mathbf{F}_1,k}^{nft}$, $k = 1, \dots, 5$ 78

FIGURE 4.15: Integral areas of $\Omega_{\mathbf{F}_1}$ and $\hat{\Omega}_{\mathbf{F}_1}$ 78

FIGURE 4.16: The physical domain and control points for each maps \mathbf{F}_1 and \mathbf{G} of Example 4.3.1. 84

FIGURE 4.17: Integral areas on the parameter space $\hat{\Omega}_{\mathbf{F}_1}$ of the newly designed singular mapping \mathbf{F}_1 . Note that $\Omega_{\mathbf{F}_1}$ corresponding to $\hat{\Omega}_{\mathbf{F}_1}$ is the singular zone including non flat-top area of PU functions in the physical domain. 84

FIGURE 4.18: Relative errors (%) of the computed solutions of the Laplace equation in Example 4.3.1 in L_∞, L_2 , and energy norm. 85

FIGURE 5.1: Deformation of a transverse normal according to Kirchoff (classical), Reissner-Mindlin (first order), and third order plate theories 89

FIGURE 5.2: (a) Maximum deflection of transverse displacement w occurs at the center of the plate (b) The rotational displacement ϕ_y is zero at the pair of two edges corresponding to the lines $y = 0$ and $y = 1$ because of the simply supported boundary conditions (c) It occurs in skew symmetric for the twisting moment because of simply supported boundary conditions 94

(a) Deformed shape of the plate along the displacement w 94

(b) Deformed shape of the plate along the displacement ϕ_y 94

(c) Twisting moment M_{xy} of the plate 94

FIGURE 5.3: (a) Partition of rectangular plate into four patches (b) Simply supported rectangular plates subjected to uniaxial compression 95

(a) Patches of plate 95

(b) Rectangular plate subjected to in-plane compression loading . . 95

FIGURE 5.4: Partition of of rectangular plate into three patches 102

FIGURE B.1: Relative errors (%) in maximum norm of displacement u versus the h -sizes with various intensity factors and $p_\xi = 3$ fixed. 121

FIGURE B.2: Relative errors (%) in maximum norm of displacement v versus the h -sizes with various intensity factors and $p_\xi = 2$ fixed. 121

FIGURE B.3: Relative errors (%) in L_2 -norm of displacement u versus the h -sizes with various intensity factors and $p_\xi = 2$ fixed. 122

FIGURE B.4: Relative errors (%) in L_2 -norm of displacement v versus the h -sizes with various intensity factors and $p_\xi = 3$ fixed. 122

LIST OF TABLES

TABLE 3.1: Control points $\mathbf{B}_{i,j}$ and weights $w_{i,j}$.	36
TABLE 3.2: The relative error in the maximum norm as well as in the L_2 -norm of the computed displacement u and the relative error in the maximum norm of the computed stress σ_x of the elasticity (3.18) in the curved domain Fig. 3.4. The degrees are the polynomial degrees of B-spline functions. Note that the p -refinement is made in the ξ -direction as well as in the η -direction.	48
TABLE 3.3: The relative error in the maximum norm as well as in the L_2 -norm of the computed displacement v and the relative error in the maximum norm of the computed stress σ_y of the elasticity (3.18) in the curved domain 3.4. The degrees are the polynomial degrees of B-spline functions. Note that the p -refinement is made in the ξ -direction as well as in the η -direction.	49
TABLE 3.4: The relative error(%) in the maximum norm, of the computed stress field (with respect to a p -refinement) of the single edge cracked plate problem are listed.	50
TABLE 3.5: The relative error(%) in the energy norm (with respect to a p -refinement) of the single edge cracked plate problem are listed. Note that $\{u\} = \{u_x, u_y\}^T$ is the displacement field.	52
TABLE 4.1: Control points $\mathbf{B}_{i,j}$ and weights $w_{i,j}$. μ is a fixed real number with $0.5 \leq \mu \leq 0.9$.	58

TABLE 5.1: non dimensional transverse displacement \hat{w} of a square Reissner-Mindlin plate for two different ratios of a/h and boundary conditions under uniform transverse pressure ($q = 1$). \hat{w}_k means RPP approximate solution with order of RPP k . Exact solutions, \hat{w}_{exact} 's are Navier solutions with 1000×1000 terms for each solutions [60].	93
TABLE 5.2: Fundamental frequency parameters $\bar{\omega}_{mn}$ for a CCCC square Reissner-Mindlin plate with $h/a = 0.1$, $k_s = 0.8601$, $\nu = 0.3$	96
TABLE 5.3: Fundamental frequency parameters $\bar{\omega}_{mn}$ for a CCCC square Reissner-Mindlin plate with $h/a = 0.01$, $k_s = 0.8601$, $\nu = 0.3$	96
TABLE 5.4: Fundamental frequency parameters $\bar{\omega}_{mn}$ for a SSSS square Reissner-Mindlin plate with $h/a = 0.1$, $k_s = 0.833$, $\nu = 0.3$	97
TABLE 5.5: Fundamental frequency parameters $\bar{\omega}_{mn}$ for a SSSS square Reissner-Mindlin plate with $h/a = 0.01$, $k_s = 0.833$, $\nu = 0.3$	98
TABLE 5.6: Fundamental frequency parameters $\bar{\omega}_{mn}$ for a SCSC square Reissner-Mindlin plate with $h/a = 0.1$, $k_s = 0.822$, $\nu = 0.3$	99
TABLE 5.7: Fundamental frequency parameters $\bar{\omega}_{mn}$ for a SCSC square Reissner-Mindlin plate with $h/a = 0.01$, $k_s = 0.822$, $\nu = 0.3$	99
TABLE 5.8: The critical buckling factors, K_b , of simply supported rectangular plates with different length-to-width ratios a/b , and thickness-to-width ratios, t/b , subjected to uniaxial compression	100
TABLE 5.9: Solution of the Reissner-Mindlin model of the semi-infinite plate problem with $q = c_0 \cos(x/L)$ ([2])	103
TABLE 5.10: Absolute maximum norm error of displacement field (w_0, ϕ_x, ϕ_y) and energy norm error with soft simply supported boundary condition. B-splines with Shishkin type knot refinement are employed.	104

- TABLE 5.11: Absolute maximum norm error in displacement field (w_0, ϕ_x, ϕ_y) and absolute energy norm error with free boundary condition. B-splines with Shishkin type knot refinement are employed. 105
- TABLE A.1: The relative errors (%) of enriched IGA for the Motz problem: (i) The first column " (p_{nurb}, C^k) " stands for polynomial degree of NURBS for un-enriched IGA and the regularity of NURBS, respectively. For each k -refinement for IGA, only one knot is inserted. We use two patches for the Motz domain. (ii) The second column " p_{rich} " stands for the polynomial degree of B-spline functions in ξ as well as η for the enriched basis functions. (iii) The last row " ∞ " indicates the strain energy of the true solution. 115
- TABLE A.2: The relative errors (%) of un-enriched IGA for the Motz problem: The computed strain energy and their relative errors (%) of IGA of the Motz problem. The first column is the number of polynomial degree and the number of knot insertions with multiplicity 1 in the k -refinement of NURBS. 115
- TABLE A.3: The relative errors (%) of IGA with 5-radical mesh for the Motz problem: The computed strain energy obtained by the 5-radical mesh and their relative errors (%) of IGA of the Motz problem. The first column is the number of polynomial degree and the number of knot insertions with multiplicity 1 in the k -refinement of NURBS. 116

- TABLE A.4: The relative errors (%) of enriched IGA: The computed strain energy and the relative errors (%) of the Laplace equation in the cracked unit disk. The entries of the first column are the polynomial degrees of NURBS and regularities at the only one inside knot in the k -refinement. The entries of the second column are the polynomial degrees of the B-spline functions in both variables for the enrichment functions. 116
- TABLE A.5: The relative errors (%) of un-enriched IGA: The computed strain energy and their relative errors (%) of IGA of the Laplace equation on the cracked unit disk. The first column is the number of polynomial degree and the number of knot insertions with multiplicity 1 in the k -refinement of NURBS. 117
- TABLE A.6: The relative errors (%) of IGA with 5-radical mesh: The computed strain energy obtained by the 5-radical mesh and their relative errors (%) of IGA of the Poisson equation in the L -shaped domain. The first column is the number of polynomial degree and the number of knot insertions with multiplicity 1 in the k -refinement of NURBS. 117
- TABLE A.7: The relative errors (%) of enriched IGA: The computed strain energy and the relative errors (%) of the Laplace equation in the L -shaped domain. The entries of the first column are the polynomial degrees of NURBS and regularities at the only one inside knot in the k -refinement. The entries of the second column are the polynomial degrees of the B-spline functions in both variables for the enrichment functions. 118

TABLE A.8: The relative errors (%) of un-enriched IGA: The computed strain energy and their relative errors (%) of IGA of the Laplace equation on the L -shaped domain. The first column is the number of polynomial degree and the number of knot insertions with multiplicity 1 in the k -refinement of NURBS. 118

TABLE A.9: The relative errors (%) of IGA with 5-radical mesh: The computed strain energy obtained by the 5-radical mesh and their relative errors (%) of IGA of the Poisson equation in the L -shaped domain. The first column is the number of polynomial degree and the number of knot insertions with multiplicity 1 in the k -refinement of NURBS. 119

TABLE C.1: Geometric setting for wedge-shaped domain $\Omega^{(\pm\alpha)}$ (Example 3.2.1). (a) The degree of polynomials and knot vectors for variables ξ and η , respectively. Note that there are $p + 1$ zeros and $p + 1$ ones are presented in the knot vector Ξ_η . (b) Control points and corresponding weights. 124

- (a) Knot vectors 124
- (b) Control points and weights 124

TABLE C.2: Geometric data to construct the NURBS mapping to deal with the elasticity containing singularity in the curved domain (Example 3.2.2). (a) The open knot vectors. (b) Control points and corresponding weights for $j = 1, 2, 3$. (c) Control points and corresponding weights for $j = 4, 5$. Here, $\beta = \tan(\pi/8)$ and $w_0 = \cos(\pi/8)$. 125

- (a) Knot vectors 125
- (b) Control points and weights for $j = 1, 2, 3$ 125
- (c) Control points and weights for $j = 4, 5$ 125

TABLE C.3: Geometric setting for the single edge cracked plate (Example 3.2.3). (a) The degree of polynomials and knot vectors for variables ξ and η , respectively. (b) Control points and corresponding weights for $j = 1, 3, 5$. Here, $\beta = \tan(\pi/8)$ and $w_0 = \cos(\pi/8)$.	126
(a) Knot vectors	126
(b) Control points and weights for $j = 1, 3, 5$	126

CHAPTER 1: INTRODUCTION

Practical engineering problems involve analysis of engineering structures such as vehicles, airplanes, rockets, appliances, nuclear power plants and so on. Most of these structures are designed by Computer Aided Design (CAD). To analyze solid models which are newly designed by CAD, by means of Finite Element Analysis (FEA), it is necessary to communicate with CAD description of geometries. For models having complex geometry, converting data including information of geometric configuration between CAD and FEA packages wastes most of time in the process of engineering analysis. In order to resolve this major engineering bottleneck, most recently, introducing non-uniform rational B-splines (NURBS) basis functions to FEA, Hughes et al. [27] developed a new numerical method called Isogeometric Analysis (IGA). That is, IGA is a framework bridging the gap between FEA and CAD.

IGA [8, 16, 27] are designed to combine two tasks: CAD and FEA as mentioned above, so that it is drastically reduced the error in the representation of the computational domain for analysis by providing more accurate modeling of complex geometry and exactly represent common engineering shapes such as conic sections. IGA makes brief mesh refinement of compound geometries by the use of the “exact” CAD geometry directly at the coarsest level of discretization. Also, it has been introduced new refinement sequence called “ k -refinement” that increases the smoothness of basis functions by using less degrees of freedom beyond the conventional \mathcal{C}^0 -continuity of FEA. The k -refinement results in the improvement of accuracy and efficiency compared with conventional p -refinement analogue. These are archived by using B-splines or NURBS that are briefly introduced in Chapter 2, for the description of geometry

as well as for the representation of the unknown solution fields.

In order to handle the singularities arising in the PDEs, Babuška and Oh [7] introduced the mapping techniques called the Method of Auxiliary Mapping (MAM) into conventional p -FEM. In a similar spirit to MAM, it is possible to construct a novel NURBS geometrical mapping that generates singular functions resembling the singularities. The mapping technique proposed in [30] is concerned with constructions of unconventional novel geometrical mapping by which push-forward functions of B-spline functions defined on the parameter space into physical domain generate singular functions that resemble the given point singularities. In other words, the pull-back of the singularity into the parameter space by the non standard NURBS mapping becomes highly smooth. In Chapter 3, we generalize the proposed mapping techniques introduced in [30] and apply them to elasticity containing singularities.

In Chapter 3, we use NURBS basis functions only for the constructions of geometrical mappings that precisely map the parameter space onto a physical domain, however we employ B-spline basis functions (continuous piecewise polynomials) that are interpolants at each knot for analysis.

It is important to note that the mapping technique proposed in [30] is not properly working with neither the B-spline functions elevated by the k -refinement nor the NURBS functions. It means that the p -refinement of B-spline piecewise polynomials is most suitable for the mapping method. Since NURBS functions used in IGA are generally non-polynomial rational functions, and the mapping method uses the B-spline functions (piecewise polynomials), a direct use of the mapping method in IGA is not expected to yield optimal results. In practice, moreover, the cracks are appeared later because of accumulated fatigues, wear, corrosion, and so on, of the structures. Thus NURBS basis functions generated by the design mapping are not suitable to capture the singularity behavior of the solution along the crack faces.

In Chapter 4, we thus consider how to use the proposed mapping method in IGA of

elliptic problems containing singularities without changing the design mapping. For this end, we embed the mapping methods into the standard IGA that use NURBS basis functions for which $h-p-k$ -refinements introduced in Chapter 2, are applicable for improved computational solution. In other words, the mapping methods are used to enrich NURBS basis functions around neighborhood of singularities so that they can capture the singular behaviors of the function to be approximated.

For solid models originated propagating cracks, several methods have been developed, to deal with the propagating cracks. Some of these methods are based on meshfree methods such as [4, 9, 10, 40] and incorporation of the extended FEM (XFEM) with IGA, called eXtended IsoGeometric Analysis (XIGA) such as [12, 44]. In particular, XIGA framework [12] has shown the potential possibility of XFEM that can be extended to analysis based on B-spline basis. In methodologies that adopt the idea of XFEM [9, 12, 44], discontinuity across a crack is represented by Heaviside functions and crack tip displacement field is reproduced by crack tip enrichment functions. In Chapter 4, we introduce a methodology combining the proposed mapping method with flat-top Partition of Unity (PU) functions. This methodology has features of meshfree methods that are no use of re-meshing or rearranging of the nodal points. Also, it is not required to alter design mapping, use Heaviside functions and crack tip enrichment functions.

In Chapter 5, meshfree particle method are applied for analysis of thick plates, is considered . In the early period, most of the reports concentrated on thin plates, for which the transverse shear influences were not considered. The classical plate theories (CPT) based on the Kirchhoff hypothesis, are often used for thin plates. But these classical theories are inadequate to predict the gross response characteristics of moderately thick laminated composite plates as well as plates with high anisotropy. Usually in thicker plates, the vibration solutions are un-conservatively high. The inaccuracy is caused by ignoring the transverse shear and normal strains in the plates.

Thus, many shear deformation plate theories were developed to improve the analysis of the vibration of plates, and these had led to more accurate results. The first order shear deformation plate theory (FSDT) extends the kinematics of the CPT, in which transverse normal and shear stresses are neglected by relaxing the normality restriction and allowing for arbitrary but constant rotation of transverse normals. Numerous papers and books have been published on the vibration analysis of plates using various plate theories [37, 47, 59, 65].

The buckling analysis of plates is another class of eigenvalue problem. As is well known, a plate may lose its ability to withstand the external loadings, when the in-plane strain reaches a critical level. This phenomenon is the buckling of the plate, and the corresponding critical load at which the plate starts to become unstable, is termed the buckling load.

To analyze the buckling behavior of a thin plate, the CPT is often used. However, similar to the vibration of plates, when the thickness of the plate increases, the transverse shear-deformation effects will significantly influence the results of the buckling analysis. Thus the CPT is not applicable, and FSDTs [60, 32] are often resorted to analyze the buckling behavior instead of the CPT. Furthermore, the use of CPT may result in a different buckling mode shape compared with those of other plate theories, such as 3D elasticity theory, FSDT or higher order shear-deformation theory (HSDT).

Many methodologies have been implemented for various plate buckling and free vibration problems. These methods include analytical and numerical techniques, such as the Ritz method [17, 31], differential quadrature method [13, 68], finite strip methods [19], the finite element method [26, 61], and meshfree methods [36, 38] etc.

Meshless methods [3, 5, 6, 11, 34, 38, 63, 64] have several advantages over the conventional finite element method [14, 15, 48]. Their flexibility and wide applicability have gained attention from scientists and engineers to these dynamic research areas [22, 23, 24]. Meshless methods employ flexible smooth base functions and use no mesh

or use minimal background meshes. Actually, meshless methods have been referred to as meshfree methods [3, 5, 6], Reproducing Kernel Particle Methods (RKPM) [25, 34, 40, 41, 42], Reproducing Kernel Element Methods (RKEM) [34, 35, 39], Generalized Finite Element Methods (GFEM) (Partition or Unity Finite Element Methods (PUFEM)) [46, 63, 64], $h-p$ Cloud Method [20] and Element Free Galerkin Method (EFGM) [3].

Although these approaches are applicable in solving many difficult science and engineering problems, they have some difficulties: (1) The popular partitions of unity, an essential ingredient of GFEM, is complicated (such as Shepard type PU functions) or leads to singular stiffness matrix (when linear finite element bases functions are used as PU functions); (2) These popular PU functions have limited regularities; (3) When enriched local approximation functions are introduced, the integrations for these functions require much longer computing times; (4) These popular PU functions do not satisfy the Kronecker delta property except for hat functions. They have difficulties in implementing non-homogeneous essential boundary conditions.

To overcome these difficulties, encountered in meshless methods, Oh et al introduced three closed- form partition of unity (PU) functions that have flat-top: (1) Convolution partition of unity [55] for any partition of a given domain; Using convolution partition of unity, Oh et al. introduced several meshless methods that are called patchwise RPPM, adaptive RPPM, and RSPM (Reproducing Singularity Particle Method) in [51, 54, 55, 57]. Note that RPPM is similar to RKPM [5, 25, 34, 35, 39, 40, 41, 42]. (2) Almost everywhere partition of unity [52] that satisfies partition of unity property except at corner points. (3) Generalized product partition of unity [53]. Using PU functions with flat-top gives relatively small matrix condition numbers.

In Chapter 5, we apply PU function with flat-top to construct smooth local approximation functions that have the reproducing polynomial property and the Kronecker delta property, and then effectiveness of the patchwise reproducing poly-

mial particle method (Patchwise RPPM) is demonstrated with various aspect ratio of plates. Also, the potential of the patchwise RPPM with B-splines for boundary layer problems is referred at the last section in Chapter 5.

Finally, we concluding remarks and future works are discussed at the last Chapter in this dissertation.

CHAPTER 2: PRELIMINARIES

2.1 B-splines and NURBS

In this section, we briefly review definitions and terminologies about B-splines and NURBS that are used throughout this dissertation. We follow those in the books [16, 62, 58], and we thus refer to these texts for details.

2.1.1 B-splines

A **knot vector** $\Xi = \{\xi_1, \xi_2, \dots, \xi_m\}$ is a nondecreasing sequence of real numbers in the parameter space $[0, 1]$, and the components ξ_i are called **knots**. An **open knot vector of order** $p + 1$ is a knot vector that satisfies

$$\xi_1 = \dots = \xi_{p+1} < \xi_{p+2} \leq \dots \leq \xi_{m-p-1} < \xi_{m-p} = \dots = \xi_m,$$

in which the first and the last $p + 1$ knots are repeated and the interior knots can be repeated at most p times.

The **B-spline functions** $N_{i,k}(\xi)$ **of order** $k = p + 1$ corresponding to the knot vector $\Xi = \{\xi_1, \xi_2, \dots, \xi_m\}$ are piecewise polynomials of degree p which are constructed recursively by the formula (*Cox-de Boor*):

$$N_{i,1}(\xi) = \begin{cases} 1 & \text{if } \xi_i \leq \xi < \xi_{i+1}, \\ 0 & \text{otherwise,} \end{cases} \quad \text{for } 1 \leq i \leq m - 1,$$
$$N_{i,t}(\xi) = \frac{\xi - \xi_i}{\xi_{i+t-1} - \xi_i} N_{i,t-1}(\xi) + \frac{\xi_{i+t} - \xi}{\xi_{i+t} - \xi_{i+1}} N_{i+1,t-1}(\xi), \quad \text{for } 1 \leq i \leq m - 1, 2 \leq t \leq k.$$

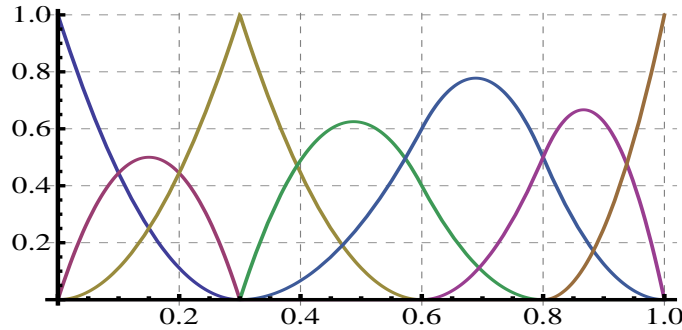


Figure 2.1: B-spline functions $N_{i,3}(\xi)$, $i = 1, 2, \dots, 7$ of order $k = 3$ corresponding to the knot vector $\Xi = \{0, 0, 0, 0.3, 0.3, 0.5, 0.6, 1, 1, 1\}$.

(There is a terminology conflict between the design and analysis community. Designers will say a quadratic polynomial has degree 2 and order 3 [28, 62]). B-spline of degree p have up to $p-1$ continuous derivatives. A repeated knot will reduce the number of continuous derivatives by 1. When the multiplicity equals p , the B-spline function is interpolant or nodal. For example, the piecewise quadratic polynomial B-spline functions $N_{i,3}(\xi)$ corresponding to the knot vector $\Xi = \{0, 0, 0, 0.3, 0.3, 0.5, 0.6, 1, 1, 1\}$ are depicted in Fig. 2.1.

The B-spline functions are useful in design as well as finite element analysis because they have the following properties:

1. Non-negativity: $N_{i,k}(\xi) \geq 0$, for all i, k and $0 \leq \xi \leq 1$.
2. There are $p + 1$ nonzero functions on a knot span $[\xi_i, \xi_{i+1})$.
3. B-spline functions satisfy the partition of unity. i.e. $\sum_{i=1}^{m-k} N_{i,k}(\xi) = 1$.
4. B-spline functions are linearly independent.
5. $N_{1,k}(0) \equiv N_{m-1,k}(1) \equiv 1$.
6. A B-spline function $N_{i,k}(\xi)$ has a compact support $[\xi_i, \xi_{i+k})$. It means that higher order B-spline functions have support across larger portions of the domain.

A **B-spline curve** is defined as follows:

$$\mathbf{C}(\xi) = \sum_{i=1}^{m-k} N_{i,k}(\xi) \mathbf{B}_i,$$

where \mathbf{B}_i are control points that make B-spline functions draw a desired curve as shown in Fig. 2.2(a) and corresponding B-splines 2.2(b).

B-spline curves possess the following important properties:

1. The properties of the B-spline curve follow directly from the properties of the B-splines.
2. Moving a single control point does not affect more than $p + 1$ B-splines of the curve, because the compact support of the B-splines gets passed on to the curve.
3. Non-negativity of the B-splines leads to the convex hull property. i.e. If $\xi \in [\xi_i, \xi_{i+1})$, then $\mathbf{C}(\xi)$ lies within the convex hull of the control points $\mathbf{P}_{i-p}, \dots, \mathbf{P}_i$.
4. Affine invariance property is satisfied by the partition of unity property. Let \mathbf{x} be a point in \mathbb{R}^3 , and affine transformation be denoted by \mathbf{f} , maps from \mathbb{R}^3 to \mathbb{R}^3 , defined by

$$\mathbf{f}(\mathbf{x}) = M\mathbf{x} + \mathbf{v},$$

where M is a 3×3 matrix and \mathbf{v} is a vector. For a given B-spline curve $\mathbf{C}(\xi)$ with $\mathbf{B}_i \in \mathbb{R}^3$, then

$$\begin{aligned} \mathbf{f}(\mathbf{C}) &= M \left(\sum_{i=1}^{m-k} N_{i,k}(\xi) \mathbf{B}_i \right) + \mathbf{v} \\ &= \sum_{i=1}^{m-k} N_{i,k}(\xi) M \mathbf{B}_i + \sum_{i=1}^{m-k} N_{i,k}(\xi) \mathbf{v}, \quad (\because \sum_{i=1}^{m-k} N_{i,k} = 1) \\ &= \sum_{i=1}^{m-k} N_{i,k} (M \mathbf{B}_i + \mathbf{v}) = \sum_{i=1}^{m-k} N_{i,k} \mathbf{f}(\mathbf{B}_i) \end{aligned}$$

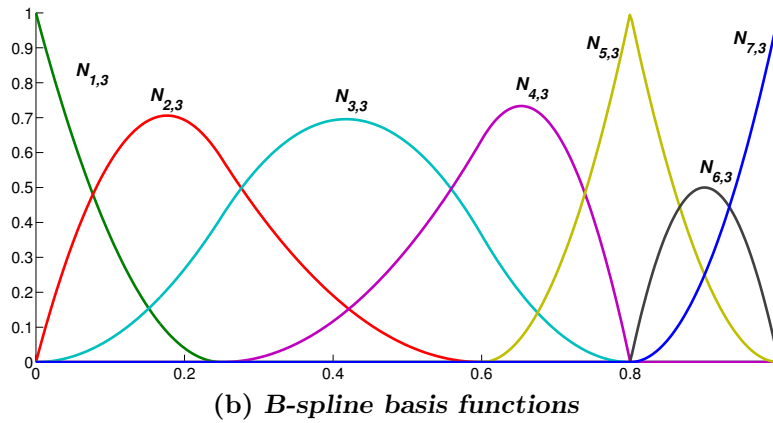
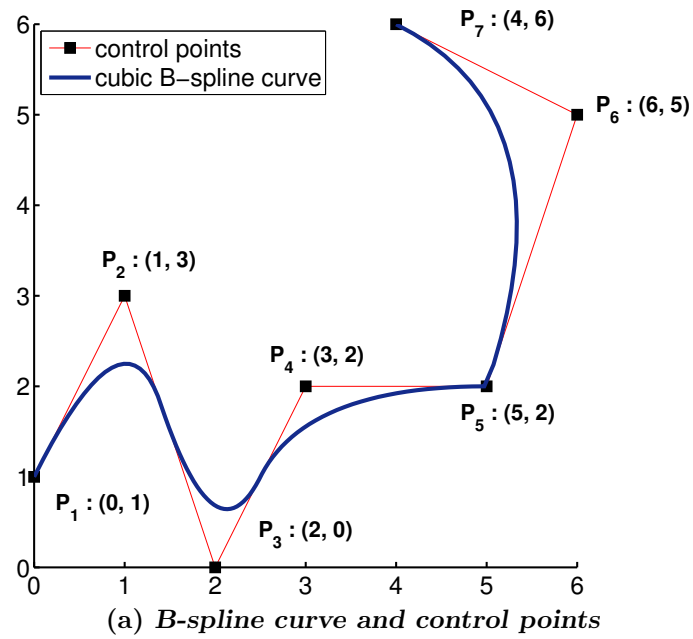


Figure 2.2: (a) B-spline curve and control points on the open knot vector $\{0, 0, 0, 0.25, 0.6, 0.8, 0.8, 1, 1, 1\}$. (b) B-spline functions corresponding to the B-spline curve shown in (a).

5. Variation diminishing property: no plane (line) has more intersections with the three-dimensional (two-dimensional) curve than with the control polygon. An example is shown in Fig. 2.3 for two-dimensional case.

Let $\Xi_\eta = \{\eta_1, \dots, \eta_n\}$ be an open knot vector and let p_η and $k' = p_\eta + 1$, respectively, be the polynomial degree and order of B-spline functions $M_{j,k'}(\eta)$. Then a **B-spline surface** is defined by

$$\mathbf{S}(\xi, \eta) = \sum_{i=1}^{m-k} \sum_{j=1}^{n-k'} N_{i,k}(\xi) M_{j,k'}(\eta) \mathbf{B}_{i,j},$$

where $\mathbf{B}_{i,j}$ are control points that make a bidirectional control net as shown in Fig. 2.4.

2.1.2 NURBS

Let $\{w_i : i = 1, \dots, m - k\}$ be the set of weights. Then the corresponding **NURBS** basis functions are defined by

$$R_{i,k}(\xi) = \frac{N_{i,k}(\xi)w_i}{W(\xi)}, \quad W(\xi) = \sum_{s=1}^{m-k} N_{s,k}(\xi)w_s > 0.$$

The NURBS basis functions are now piecewise rational functions and inherit their properties from the B-spline basis functions like continuity across knots, local support and non-negativity.

A **NURBS curve** corresponding to the control points $\{\mathbf{B}_i : i = 1, \dots, m - k\}$, NURBS basis functions $\{R_{i,k}(\xi) : i = 1, \dots, m - k\}$, and the weights $\{w_i : i = 1, \dots, m - k\}$ is

$$\mathbf{C}(\xi) = \sum_{i=1}^{m-k} R_{i,k}(\xi) \mathbf{B}_i. \quad (2.1)$$

Let $\{w_{i,j} : i = 1, \dots, m - k, j = 1, \dots, n - k'\}$ be the set of weights. Then **NURBS** basis functions corresponding to the open knot vectors Ξ_ξ and Ξ_η and the

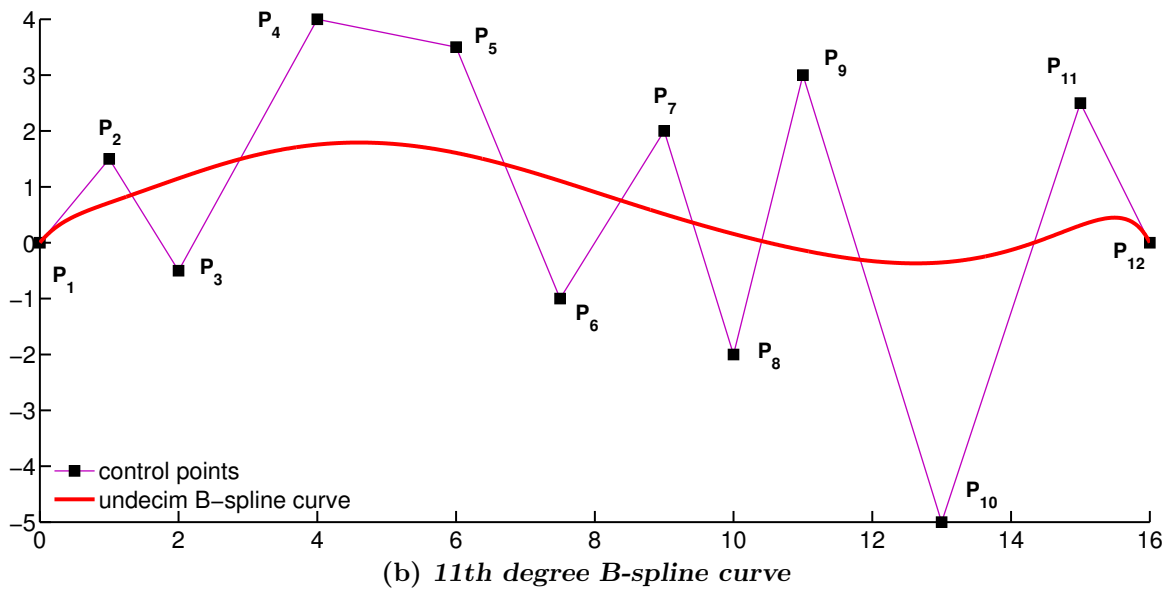
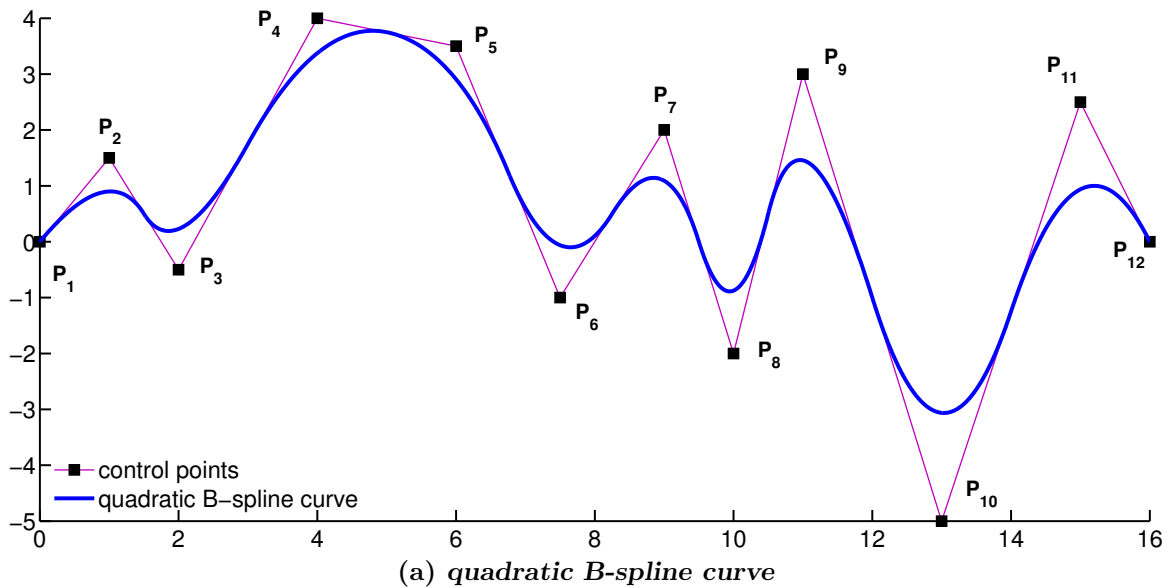


Figure 2.3: (a) A quadratic curve on the knot vector $\Xi = \{0, 0, 0, 0.1, 0.2, 0.3, 0.4, 0.5, 0.6, 0.7, 0.8, 0.9, 1, 1, 1\}$. (b) A 11th degree B-spline curve using the same control points with (a) defined on $\Xi = \{0, 0, 0, 0, 0, 0, 0, 0, 0, 0, 0, 1, 1, 1, 1, 1, 1, 1, 1, 1, 1, 1\}$

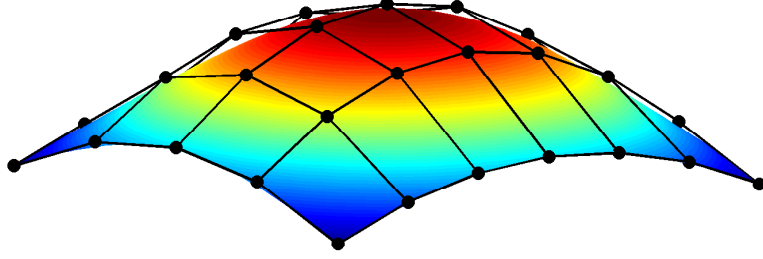


Figure 2.4: B-spline surface and control net

weights $\{w_{i,j}\}$ are defined by

$$R_{i,j}(\xi, \eta) = \frac{N_{i,k}(\xi)M_{j,k'}(\eta)w_{i,j}}{W(\xi, \eta)},$$

where

$$W(\xi, \eta) = \sum_{s=1}^{m-k} \sum_{t=1}^{n-k'} N_{s,k}(\xi)M_{t,k'}(\eta)w_{s,t} > 0.$$

Let $\{\mathbf{B}_{i,j} : i = 1, \dots, m - k, j = 1, \dots, n - k'\}$ be a set of control points in \mathbb{R}^d , $d \geq 2$. Then a **NURBS surface** corresponding to the control points $\{\mathbf{B}_{i,j}\}$, NURBS basis functions $\{R_{i,j}(\xi, \eta)\}$, and the weights $\{w_{i,j}\}$ is

$$\mathbf{S}(\xi, \eta) = \sum_{i=1}^{m-k} \sum_{j=1}^{n-k'} R_{i,j}(\xi, \eta)\mathbf{B}_{i,j}.$$

An example of the NURBS surface is shown in Fig. 2.5.

2.1.3 Perspective Map

In this subsection, we will represent a NURBS (rational B-spline) curve or surface in three-dimensional space as a non-rational (piecewise polynomial) B-spline curve in four-dimensional space using homogeneous coordinates and perspective map for the efficient processing of algorithm and compact data storage of control points and

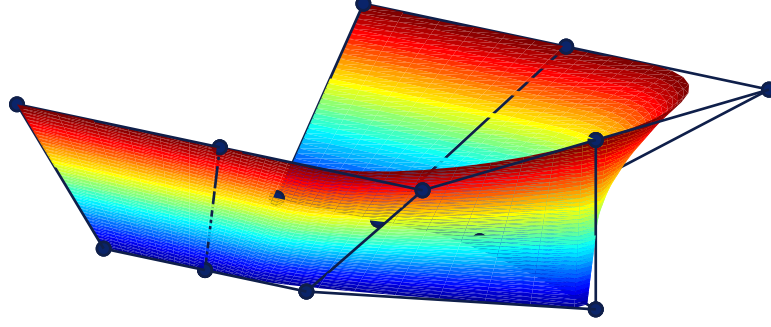


Figure 2.5: NURBS surface of prow in a ship and control net

weights. Let us start with a point in three-dimensional Euclidean space, $\mathbf{B} = (x, y, z)$. Then \mathbf{B} is written as $\mathbf{B}^w = (wx, wy, wz, w) = (X, Y, Z, W)$ in four-dimensional space, $w \neq 0$. Now we introduce a perspective map $H\{\mathbf{B}^w\}$ from four-dimensional space to the hyperplane $W = 1$, defined by

$$H\{\mathbf{B}^w\} = H\{(X, Y, Z, W)\} = \begin{cases} \left(\frac{X}{W}, \frac{Y}{W}, \frac{Z}{W}\right) & \text{if } W \neq 0 \\ \text{direction } (X, Y, Z) & \text{if } W = 0 \end{cases}$$

Then \mathbf{B} is obtained from \mathbf{B}^w through the perspective map H . Note that the perspective map H can be interpreted by that a map from the origin to the hyperplane $W = 1$ as shown in Fig. 2.6 for two-dimensional case, $\mathbf{B} = (x, y)$.

Now for a given set of control points \mathbf{B}_i , and weights, $\{w_i\}$, construct the weighted control points, $\mathbf{B}_i^w = (w_i x_i, w_i y_i, w_i z_i, w_i)$. Then we define the non-rational (polynomial) B-spline curve in four-dimensional space as

$$\mathbf{C}^w(\xi) = \sum_{i=1}^{m-k} N_{i,k}(\xi) \mathbf{B}_i^w \quad (2.2)$$

Then applying the perspective map, H , to $\mathbf{C}^w(\xi)$ yields the corresponding rational B-spline curve of Eq. (2.1), that is, writing out the coordinate functions of Eq. (2.2),

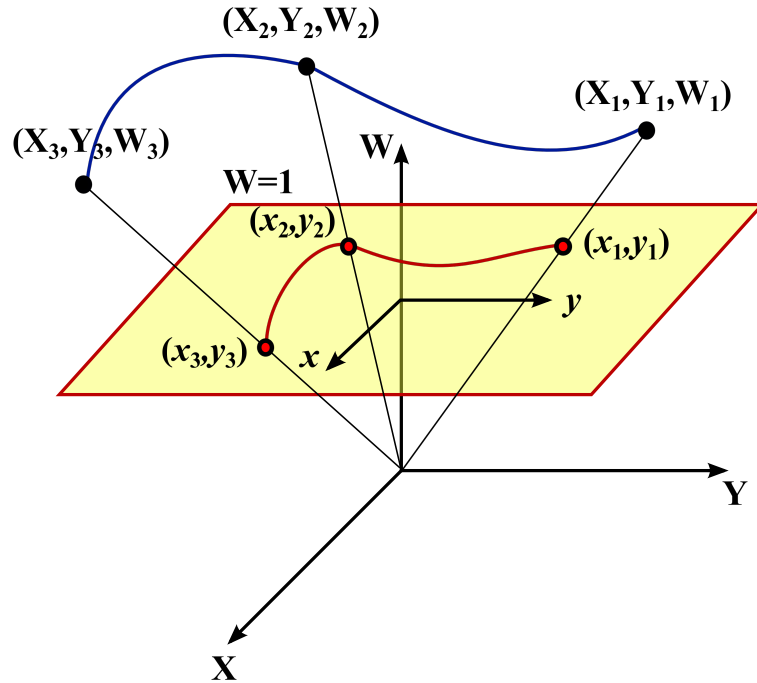


Figure 2.6: A representation of Euclidean points on the hyperplane $W = 1$ through the perspective map H

we get

$$\begin{aligned} X(\xi) &= \sum_{i=1}^{m-k} N_{i,k}(\xi) w_i x_i, & Y(\xi) &= \sum_{i=1}^{m-k} N_{i,k}(\xi) w_i y_i, \\ Z(\xi) &= \sum_{i=1}^{m-k} N_{i,k}(\xi) w_i z_i, & W(\xi) &= \sum_{i=1}^{m-k} N_{i,k}(\xi) w_i, \end{aligned}$$

Locating the curve in three-dimensional space yields

$$\begin{aligned} x(\xi) &= \frac{X(\xi)}{W(\xi)} = \frac{\sum_{i=1}^{m-k} N_{i,k}(\xi) w_i x_i}{\sum_{i=1}^{m-k} N_{i,k}(\xi) w_i} \\ y(\xi) &= \frac{Y(\xi)}{W(\xi)} = \frac{\sum_{i=1}^{m-k} N_{i,k}(\xi) w_i y_i}{\sum_{i=1}^{m-k} N_{i,k}(\xi) w_i} \\ z(\xi) &= \frac{Z(\xi)}{W(\xi)} = \frac{\sum_{i=1}^{m-k} N_{i,k}(\xi) w_i z_i}{\sum_{i=1}^{m-k} N_{i,k}(\xi) w_i} \end{aligned}$$

Using vector notation, we get

$$\begin{aligned}
H\{\mathbf{C}^w(\xi)\} &= H\{X(\xi), Y(\xi), Z(\xi), W(\xi)\} \\
&= (x(\xi), y(\xi), z(\xi)) \\
&= \frac{\sum_{i=1}^{m-k} N_{i,k}(\xi) w_i (x_i, y_i, z_i)}{\sum_{i=1}^{m-k} N_{i,k}(\xi) w_i} \\
&= \frac{\sum_{i=1}^{m-k} N_{i,k}(\xi) w_i \mathbf{B}_i}{\sum_{i=1}^{m-k} N_{i,k}(\xi) w_i} \\
&= \mathbf{C}(\xi).
\end{aligned}$$

The perspective map will be used to enrich B-spline basis functions which were used to construct a geometry, by refinement in order to compute new control points and weights. For the strategy of refinement, we will see it in next section.

2.2 Refinement

The B-spline basis can be enriched by three types of refinement of which have an analogue in standard FEM bases. These are knot insertion, degree elevation (or order elevation) and degree and continuity elevation. The first two are equivalent to h - and p -refinement respectively, the last one is dubbed k -refinement that does not exist in standard FEM. In this Section, these mechanisms are discussed and examples are shown.

2.2.1 Knot Insertion

The first mechanism by which one can enrich the basis is **knot insertion**. Let

$$\mathbf{C}^w(\xi) = \sum_{i=1}^{m-k} N_{i,k}(\xi) \mathbf{B}_i^w$$

be a NURBS (rational B-spline) curve defined on $\Xi = \{\xi_1, \dots, \xi_m\}$. Let $\bar{\xi} \in [\xi_s, \xi_{s+1})$ and insert $\bar{\xi}$ into Ξ to form the new knot vector

$$\bar{\Xi} = \{\bar{\xi}_1 = \xi_1, \dots, \bar{\xi}_s = \xi_s, \bar{\xi}_{s+1} = \bar{\xi}, \bar{\xi}_{s+2} = \xi_{s+1}, \dots, \bar{\xi}_{m+1} = \xi_m\}.$$

Then $\mathbf{C}^w(\xi)$ has a representation on $\bar{\Xi}$ of the form

$$\mathbf{C}^w(\xi) = \sum_{i=1}^{m-k+1} \bar{N}_{i,k}(\xi) \mathbf{Q}_i^w, \quad (2.3)$$

where

$$\mathbf{Q}_i^w = \alpha_i \mathbf{B}_i^w + (1 - \alpha_i) \mathbf{B}_{i-1}^w, \quad \alpha_i = \begin{cases} 1, & \text{if } i \leq s - p \\ \frac{\bar{\xi} - \xi_i}{\xi_{i+p} - \xi_i}, & \text{if } s - p + 1 \leq i \leq s, \\ 0, & \text{if } i \geq s + 1 \end{cases}$$

and the $\{\bar{N}_{i,k}(\xi)\}$ are the p th-degree B-spline basis functions on $\bar{\Xi}$. The detailed process of determining $\{\bar{N}_{i,k}(\xi)\}$ is in [58]. Note that knot insertion is just a change of vector space basis; the curve is not changed, either geometrically or parametrically.

2.2.2 Degree Elevation

The second mechanism by which one can enrich the basis is degree elevation. As its name implies, the process involves raising the B-spline basis functions used to represent the geometry. If the basis has $p - m_i$ continuous derivatives across element boundaries where m_i is a multiplicity of i th knot value, it is clear that when p is increased, m_i must also be increased if we are to preserve the discontinuities in the various derivatives already existing in the original curve. During degree elevation, the multiplicity of each knot value is increased by one, but no new knot values are added. As with knot insertion, neither the geometry nor the parameterization are changed.

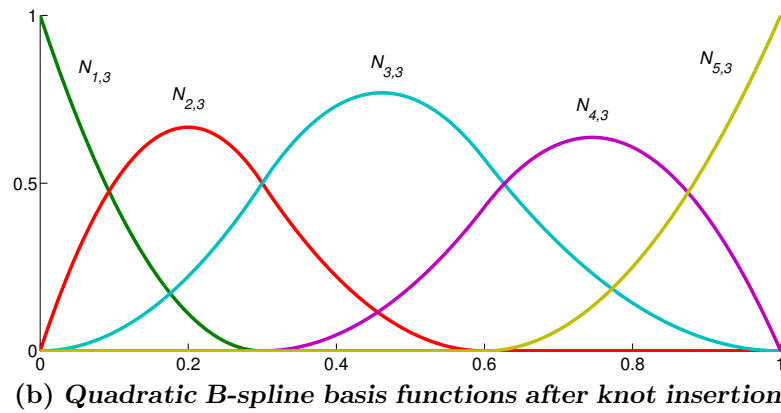
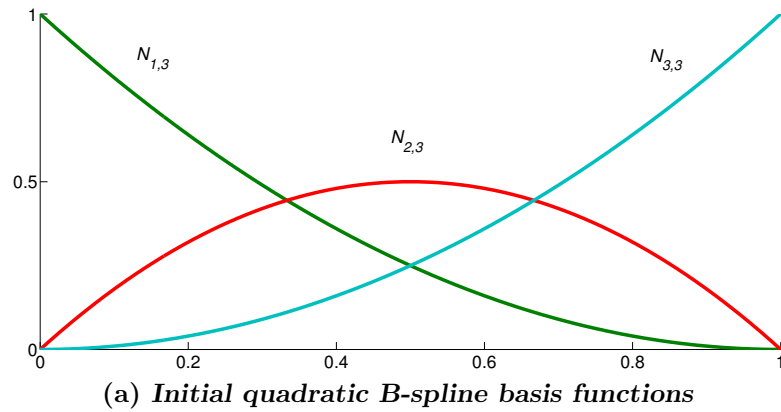


Figure 2.7: (a) The initial quadratic B-spline basis functions corresponding the open knot vector $\Xi = \{0, 0, 0, 1, 1, 1\}$. (b) Quadratic B-spline basis functions after knot insertion, corresponding the open knot vector $\bar{\Xi} = \{0, 0, 0, 0.3, 0.6, 1, 1, 1\}$

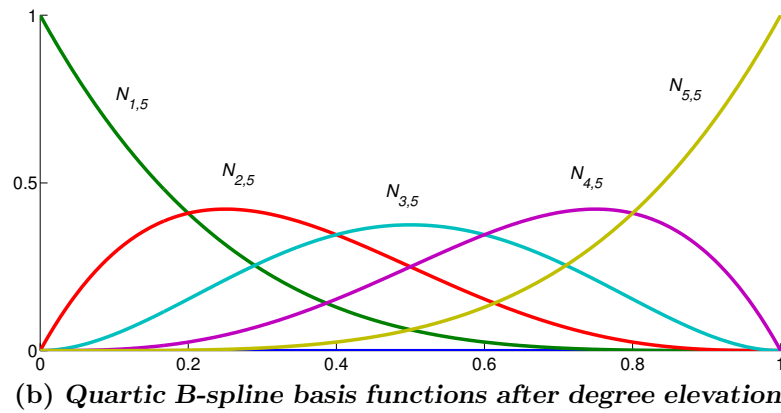
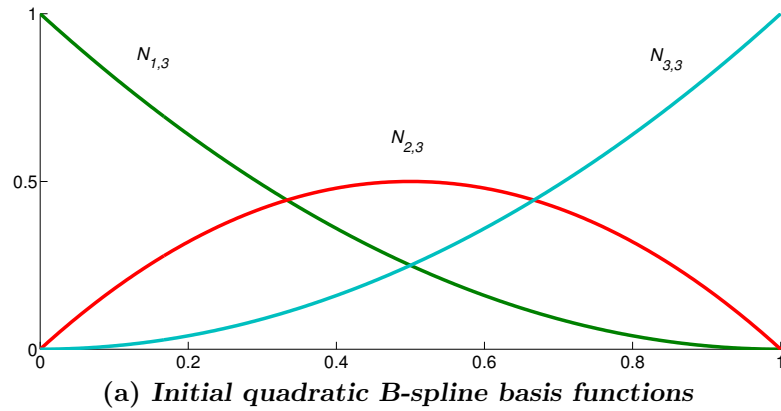


Figure 2.8: (a) The initial quadratic B-spline basis functions corresponding the open knot vector $\Xi = \{0, 0, 0, 1, 1, 1\}$. (b) Quartic B-spline basis functions after degree elevation of the quadratic B-spline basis functions, corresponding the open knot vector $\bar{\Xi} = \{0, 0, 0, 0, 0, 1, 1, 1, 1, 1\}$

For the case of Bézier curve (or Bézier segment), it is simply derived to determine new control points and weights.

Lemma 2.2.1. For the given open knot vector $\Xi = \underbrace{\{\xi_1 = 0, \dots, 0\}}_{k=p+1}, \underbrace{1, \dots, \xi_m = 1}_{k=p+1}$,

Let

$$\mathbf{C}^{\mathbf{w}}(\xi) = \sum_{i=1}^{p+1} N_{i,k}(\xi) \mathbf{B}_i^{\mathbf{w}} \quad (2.4)$$

be a p th degree Bézier curve (or Bézier segment) on the open knot vector Ξ . If we increase the order of the B-spline basis functions, p by $p+1$ in the curve Eq. (2.4), then $\mathbf{C}^{\mathbf{w}}(\xi)$ has a representation on $\bar{\Xi} = \underbrace{\{\bar{\xi}_1 = 0, \dots, 0\}}_{p+2}, \underbrace{1, \dots, \bar{\xi}_{m+2} = 1}_{p+2}$ of the form

$$\mathbf{C}^{\mathbf{w}}(\xi) = \sum_{i=1}^{p+2} N_{i,k+1}(\xi) \mathbf{Q}_i^{\mathbf{w}}, \quad (2.5)$$

where

$$\mathbf{Q}_i^{\mathbf{w}} = \begin{cases} \mathbf{B}_1^{\mathbf{w}}, & \text{if } i = 1 \\ \frac{(p+1-i)w_i \mathbf{B}_i^{\mathbf{w}} + i w_{i-1} \mathbf{B}_{i-1}^{\mathbf{w}}}{p+1}, & \text{if } 2 \leq i \leq p+1 \\ \mathbf{B}_{p+1}^{\mathbf{w}}, & \text{if } i = p+2 \end{cases} \quad (2.6)$$

Note that $\{N_{i,k}\}$ are also called Bernstein polynomials of degree p which are special instances of B-spline corresponding to the open knot vector Ξ and defined by

$$N_{i,k}(\xi) = \binom{p}{i-1} \xi^{i-1} (1-\xi)^{p-i+1} \text{ for } i = 1, \dots, p+1. \quad (2.7)$$

Proof. Since the open knot vector Ξ is consist of only 0 and 1, the number of B-spline functions (Bernstein polynomials) is $p+1$. In order to determine $\{\mathbf{Q}_i^{\mathbf{w}}\}$ in Eq. (2.5), we equate (2.4) and (2.5);

$$\mathbf{C}^{\mathbf{w}}(\xi) = \sum_{i=1}^{p+1} N_{i,k}(\xi) \mathbf{B}_i^{\mathbf{w}} = \sum_{i=1}^{p+2} N_{i,k+1}(\xi) \mathbf{Q}_i^{\mathbf{w}} \quad (2.8)$$

Rewriting the left hand side of the Eq. (2.8) by using the definition of Bernstein polynomial, we obtain

$$\begin{aligned}
\mathbf{C}^{\mathbf{w}}(\xi) &= \sum_{i=1}^{p+1} N_{i,k}(\xi) \mathbf{B}_i^{\mathbf{w}} = [(1-\xi) + \xi] \sum_{i=1}^{p+1} N_{i,k}(\xi) \mathbf{B}_i^{\mathbf{w}} \\
&= \sum_{i=1}^{p+1} (1-\xi) N_{i,k}(\xi) \mathbf{B}_i^{\mathbf{w}} + \sum_{i=2}^{p+2} \xi N_{i-1,k}(\xi) \mathbf{B}_{i-1}^{\mathbf{w}} \\
&= \sum_{i=1}^{p+1} (1-\xi) \binom{p}{i-1} (1-\xi)^{p+1-i} \xi^{i-1} \mathbf{B}_i^{\mathbf{w}} + \\
&\quad \sum_{i=2}^{p+2} \xi \binom{p}{i-2} (1-\xi)^{p+1-(i-1)} \xi^{i-2} \mathbf{B}_{i-1}^{\mathbf{w}} \\
&= \sum_{i=1}^{p+1} \binom{p}{i-1} (1-\xi)^{p+2-i} \xi^{i-1} \mathbf{B}_i^{\mathbf{w}} + \sum_{i=2}^{p+2} \binom{p}{i-2} (1-\xi)^{p+2-i} \xi^{i-1} \mathbf{B}_{i-1}^{\mathbf{w}} \\
&= \binom{p}{0} \mathbf{B}_1^{\mathbf{w}} (1-\xi)^{p+1} \xi^0 + \left[\binom{p}{1} \mathbf{B}_2^{\mathbf{w}} + \binom{p}{0} \mathbf{B}_1^{\mathbf{w}} \right] (1-\xi)^p \xi^1 + \dots + \\
&\quad \left[\binom{p}{i-1} \mathbf{B}_i^{\mathbf{w}} + \binom{p}{i-2} \mathbf{B}_{i-1}^{\mathbf{w}} \right] (1-\xi)^{p+2-i} \xi^{i-1} + \dots + \\
&\quad \left[\binom{p}{p} \mathbf{B}_{p+1}^{\mathbf{w}} + \binom{p}{p-1} \mathbf{B}_p^{\mathbf{w}} \right] (1-\xi) \xi^p + \\
&\quad \binom{p}{p} \mathbf{B}_{p+2}^{\mathbf{w}} (1-\xi)^0 \xi^{p+1} \tag{2.9}
\end{aligned}$$

Since the Eq. (2.9) must be equal to the right hand of Eq. (2.8), we obtain the following result

$$\begin{aligned}
\mathbf{Q}_1^{\mathbf{w}} &= \mathbf{B}_1^{\mathbf{w}} \\
\mathbf{Q}_i^{\mathbf{w}} &= \left[\binom{p}{i-1} \mathbf{B}_i^{\mathbf{w}} + \binom{p}{i-2} \mathbf{B}_{i-1}^{\mathbf{w}} \right], \quad 2 \leq i \leq p+1 \\
\mathbf{Q}_{p+2}^{\mathbf{w}} &= \mathbf{B}_{p+1}^{\mathbf{w}}
\end{aligned} \tag{2.10}$$

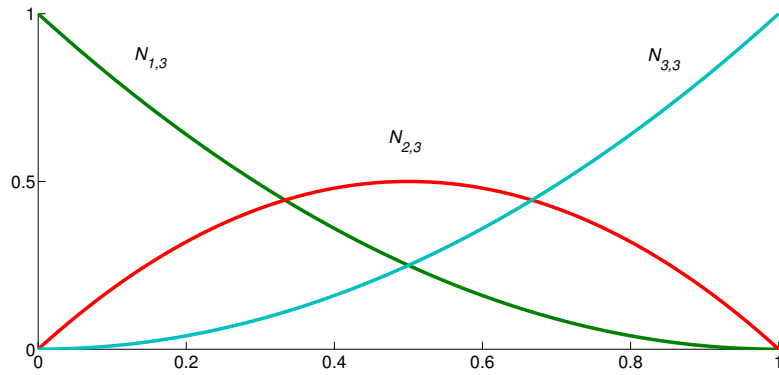
The Eq. (2.10) can be expressed as the Eq. (2.6). □

2.2.3 Degree and continuity elevation: k -refinement

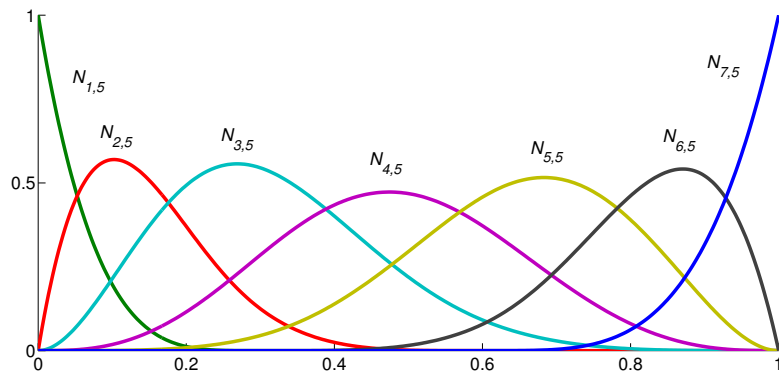
We have seen the two primitive refinement strategies for B-splines are knot insertion and degree elevation similar to h - and p - refinement, respectively in classical FEM.

A potentially more powerful type of refinement which is unique to the B-spline basis is k - refinement. Basically k -refinement is a different degree elevation strategy taking advantage of the fact that knot insertion and degree elevation do not commute. Inserting a unique knot value $\bar{\xi}$ between two distinct knots in a knot vector Ξ corresponding to B-spline curve $\mathbf{C}(\xi)$ of degree p , the basis corresponding to the unique knot value $\bar{\xi}$ is in \mathcal{C}^{p-1} space. Let us note that elevating the degree to q , using the process of Section 2.2.2, increases the multiplicity of each knot so that discontinuities in the p th derivative of the basis are preserved. Hence the basis is still in \mathcal{C}^{p-1} space. Whereas if the above process is turned around by first elevating the curve degree to q and then inserting the unique knot $\bar{\xi}$, then the basis is in \mathcal{C}^{q-1} space. This process is called k -refinement, see also Fig. 2.9.

Enriching the basis by k -refinement saves a significant amount of degrees of freedom. Let us consider a Bézier segment of degree p (similar to element in classical FEM), and n be a total number of B-spline basis functions. Obviously, then, the Bézier segment has $n = p + 1$ basis functions. If we perform knot insertion to arrive at $a + 1$ Bézier segments where a represents the number of new distinct knot values which have the multiplicity p , then the total number of B-spline basis functions n becomes $(a + 1)p + 1$ because the number of knot values is $2(p + 1) + ap$. Like before we elevate the degree of the B-spline basis functions up to q keeping the continuity by increasing the multiplicity of each knot by one. This adds a basis functions per Bézier segment, hence the total number of basis functions n is now $(a + 1)q + 1$.



(a) *Initial quadratic B-spline basis functions*



(b) *Quartic B-spline basis functions after k -refinement*

Figure 2.9: (a) The initial quadratic B-spline basis functions corresponding the open knot vector $\Xi = \{0, 0, 0, 1, 1, 1\}$. (b) Quartic B-spline basis functions after k -refinement of the quadratic B-spline basis functions, corresponding the open knot vector $\bar{\Xi} = \{0, 0, 0, 0, 0, 0.3, 0.6, 1, 1, 1, 1, 1\}$

Whereas if we follow k -refinement, that means we elevate the degree of the B-spline basis functions up to q first, then n becomes $q + 1$. After q degree elevation, we insert a new and distinct knot values which have the multiplicity 1 into the knot vector, then n will be $q + a + 1$. aq is a larger number than q because in practice the number of Bézier segments surpasses the polynomial degree by multiple order of magnitude. An example is shown in Fig. 2.10.

2.3 Closed-form Partition of Unity with flat-top

Let $\bar{\Omega}$ is the closure of $\Omega \subset \mathbb{R}^d$. We define the vector space $\mathcal{C}(\bar{\Omega})$ to consist of all those functions $\varphi \in \mathcal{C}^m(\bar{\Omega})$ for which $D^\alpha \varphi (= \partial^{\alpha_1} \partial^{\alpha_2} \dots \partial^{\alpha_d} \varphi)$ is bounded and uniformly continuous on Ω for $|\alpha| = \alpha_1 + \dots + \alpha_d \leq m$. In the following, a function $\varphi \in \mathcal{C}^m(\bar{\Omega})$ is said to be a \mathcal{C}^m -function. If Ψ is a function defined on Ω , we define the **support** of Ψ as

$$\text{supp}\Psi = \overline{\{x \in \Omega | \Psi(x) \neq 0\}}.$$

A family $\{U_k : k \in \mathcal{D}\}$ of open subsets of \mathbb{R}^d is said to be a **point finite open covering** of $\Omega \subseteq \mathbb{R}^d$ if there is an integer M such that any $x \in \Omega$ lies in at most M of the open sets U_k and $\Omega \subseteq \bigcup_k U_k$.

For a point finite open covering $\{U_k : k \in \mathcal{D}\}$ of a domain Ω , suppose there is a family $\{\varphi_k : k \in \mathcal{D}\}$ of Lipschitz functions on Ω satisfying the following conditions:

1. For $k \in \mathcal{D}$, $0 \leq \varphi_k(x) \leq 1$, $x \in \mathbb{R}^d$.
2. The support of φ_k is contained in \bar{U}_k , for each $k \in \mathcal{D}$.
3. $\sum_{k \in \mathcal{D}} \varphi_k(x) = 1$ for each $x \in \Omega$.

Then $\{\varphi_k : k \in \mathcal{D}\}$ is called a **partition of unity (PU)** subordinate to the covering $\{U_k : k \in \mathcal{D}\}$. The covering sets $\{U_k\}$ are called **patches**.

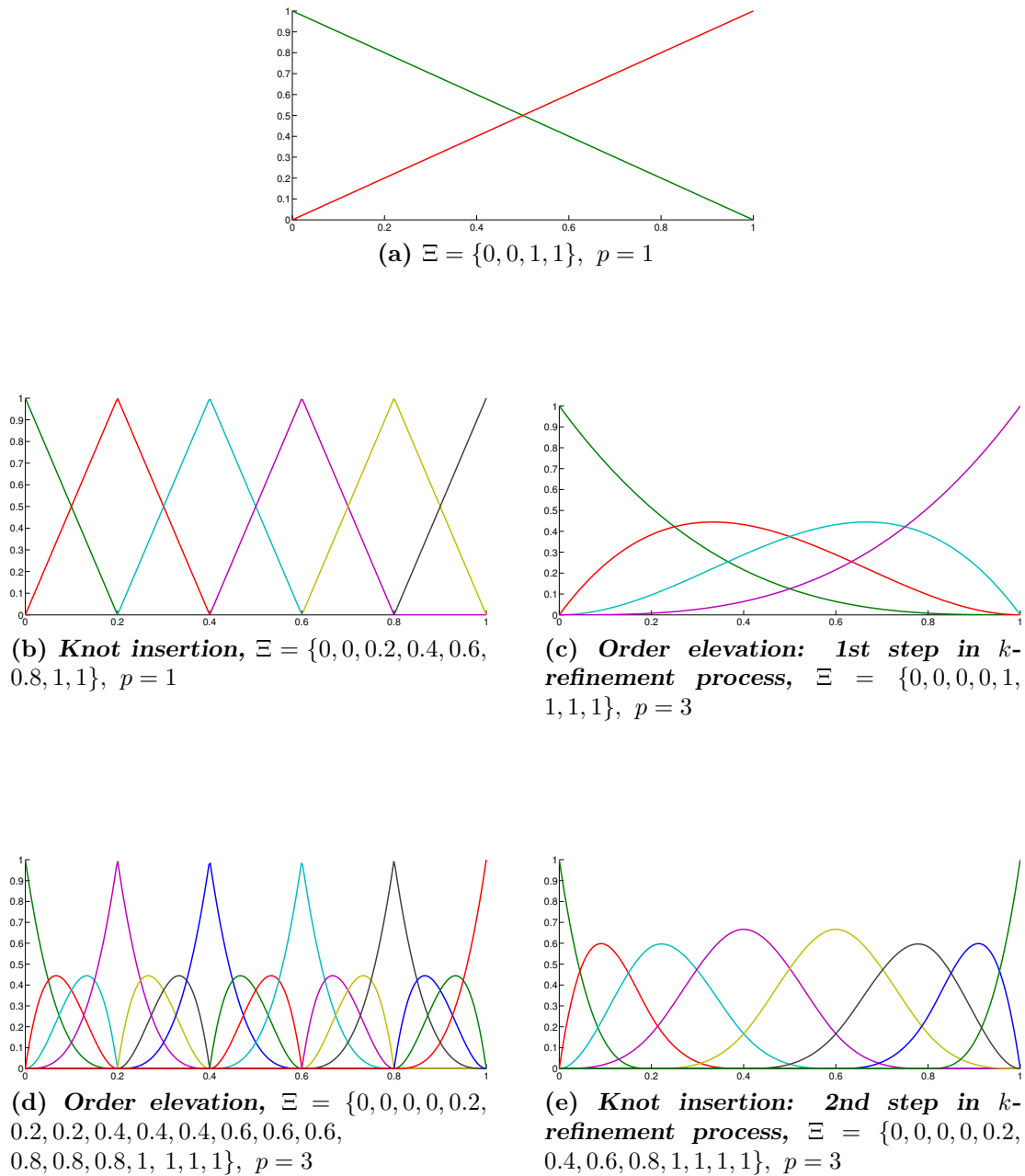


Figure 2.10: k -refinement versus p -refinement strategy (a) Starting with one Bézier segment, (b) & (d) Classic p -refinement strategy: (b) knot insertion is performed first to create many low-order Bézier segments. (d) Subsequent order elevation will preserve the C^0 -continuity across Bézier segment boundaries. (c) & (e) New k -refinement strategy: (c) order elevation is performed on the coarsest discretization. (e) Subsequent knot insertion will result in a basis which is C^{p-1} across the newly created segment boundaries.

By **almost everywhere partition of unity**, we mean $\{\varphi_k : k \in \mathcal{D}\}$ such that the condition 3 of a partition of unity is not satisfied only at finitely many points (2D) or lines (3D) on a part of the boundary.

Let $Q = \text{supp}(\varphi)$. Then $Q^{flt} = \{x \in Q : \varphi(x) = 1\}$ and $Q^{n-flt} = \overline{\{x \in Q : 0 < |\varphi(x)| < 1\}}$ are called the **flat-top** part and the **non flat-top** part of Q , respectively. The function φ is said to be a **function with flat-top** if the interior of Q^{flt} is non-void. Moreover, $\{\varphi_k : k \in \mathcal{D}\}$ is called a **partition of unity with flat-top** whenever it is partition of unity and φ_k is a function with flat-top for each $k \in \mathcal{D}$.

Notice that if f_1, \dots, f_n are linearly independent on $Q^{flt} \neq \emptyset$, the product functions, $\varphi \cdot f_1, \dots, \varphi \cdot f_n$, are also linearly independent on Q . However, if $Q^{flt} = \emptyset$, the product functions, $\varphi \cdot f_1, \dots, \varphi \cdot f_n$, could be linearly dependent. The hat functions of the conventional finite element are PU functions without flat-top.

Let Λ be a finite index set and Ω denotes a bounded domain in \mathbb{R}^d . Let $\{x_j : j \in \Lambda\}$ be a set of a finite number of uniformly or non-uniformly spaced points in \mathbb{R}^d , that are called **particles**.

The reproducing polynomial particle method (RPPM) is a Galerkin approximation method associated with use of reproducing polynomial shape functions for local approximation functions. Referring to [56], we introduce the following two definitions.

Definition 2.3.1. (*Reproducing Polynomial Property*)

Let Ω be a domain in \mathbb{R}^n , and $k \geq 0$ be an integer. The particle shape function ψ_j corresponding to the particle $x_j \in \mathbb{R}^n$, $j \in \Lambda$, is called reproducing polynomial of order k on Ω (or simply, reproducing of order k on Ω) if for any $x \in \Omega$,

$$p(x) = \sum_{j \in \Lambda} p(x_j) \psi_j(x) \text{ for any } p \in P_k(\Omega),$$

where $P_k(\Omega)$ is the space of all polynomials of degree up to k on Ω and Λ is an index set.

Definition 2.3.2. (*RPP Shape Function*) Let $k \geq 0$ be an integer. Let X be a set of particles in \mathbb{R}^n with the index set Λ . Then the function ψ_j associated with the particles x_j , $j \in \Lambda$, are called reproducing polynomial particle (RPP) shape functions with the reproducing property of order k (or simply, of reproducing order k) if and only if they are piecewise polynomials and satisfy the following:

For any $x \in \Omega \subseteq \mathbb{R}^n$,

$$\sum_{j \in \Lambda} (x - x_j)^\beta \psi_j(x) = \delta_{|\beta|,0}, \text{ for all } \beta \leq k. \quad (2.11)$$

Note that we assume that the RPP shape functions are translation invariant on the uniformly distributed particles, unless stated otherwise.

The piecewise polynomial RPP shape functions have several features different from Reproducing Kernel Particle (RKP) shape functions. The piecewise polynomial RPP shape functions are constructed by solving the system (2.11) without using window function, whereas the RKP shape functions are constructed by solving the system

$$\psi_j(x) = w(x - x_j) \sum_{0 \leq |\alpha| \leq k} (x - x_j)^\alpha b_\alpha(x),$$

with respect to a specific window function $w(x)$. Therefore, the RKP shape functions are not piecewise polynomials in general. It means that the RPP shape functions have no relevance to any specific window functions. However, both RPP and RKP shape functions are constructed to have the polynomial reproducing property.

Although there are particles on the boundaries because of the selected window function, the resulting RKP shape functions are not piecewise polynomial, so that can not be piecewise polynomial shape functions. Also, the support of the piecewise polynomial RPP shape functions are bounded by the particles, whereas the support of the RKP shape functions are bounded by points between two particles. Moreover, RKP shape functions do not satisfy the Kronecker delta property, and hence they

have difficulties in dealing with Dirichlet boundary conditions. Whereas RPP shape functions satisfy the Kronecker delta property. Hence we do not need additional numerical scheme to impose essential boundary conditions. (See [56, 57] for more details.)

2.3.1 Partition of Unity with flat-top in one-dimension

First, we define one-dimensional PU functions without flat-top, and then we modify the PU functions to have flat-top.

For any positive integer n , \mathcal{C}^{n-1} - piecewise polynomial basic PU functions are constructed as follows: For integer $n \geq 1$, we define a piecewise polynomial function by

$$\varphi_{g_n}^{(pp)}(x) = \begin{cases} \varphi_{g_n}^L(x) := (1+x)^n g_n(x) & \text{if } x \in [-1, 0], \\ \varphi_{g_n}^R(x) := (1-x)^n g_n(-x) & \text{if } x \in [0, 1], \\ 0 & \text{if } |x| \geq 1, \end{cases}$$

where $g_n(x) = a_0^{(n)} + a_1^{(n)}(-x) + a_2^{(n)}(-x)^2 + \dots + a_{n-1}^{(n)}(-x)^{n-1}$ whose coefficients are inductively constructed by the following recursion formula:

$$a_k^{(n)} = \begin{cases} 1 & \text{if } k = 0, \\ \sum_{j=0}^k a_j^{(n-1)} & \text{if } 0 < k \leq n-2, \\ 2(a_{n-2}^{(n)}) & \text{if } k = n-1. \end{cases} \quad (2.12)$$

Using the recurrence relation (2.12), $g_n(x)$ is as follows:

$$\begin{aligned}
 g_1(x) &= 1 \\
 g_2(x) &= 1 - 2x \\
 g_3(x) &= 1 - 3x + 6x^2 \\
 g_4(x) &= 1 - 4x + 10x^2 - x^3 \\
 g_5(x) &= 1 - 5x + 15x^2 - 35x^3 + 70x^4 \\
 &\vdots \qquad \qquad \qquad \vdots
 \end{aligned}$$

Then, $\varphi_{g_n}^{(pp)}$ has the following properties whose proofs can be found in [55].

- $\varphi_{g_n}^{(pp)}(x) + \varphi_{g_n}^{(pp)}(x - 1) = 1$ for all $x \in [0, 1]$. Hence, $\{\varphi_{g_n}^{(pp)}(x - j) \mid j \in \mathbb{Z}\}$ is a partition of unity on \mathbb{R} .
- $\varphi_{g_n}^{(pp)}(x)$ is a \mathcal{C}^{n-1} - function.
- The gradient of the scaled basis PU function is bounded as follows:

$$\frac{d}{dx}[\varphi_{g_n}^{(pp)}(\frac{x}{2\delta})] \leq \frac{C}{\delta}$$

Note that the constant C is ≤ 0.9 for $n \leq 3$

Using the basis PU function $\varphi_{g_n}^{(pp)}$, we construct a \mathcal{C}^{n-1} - PU function with flat-top whose support is $[a - \delta, b + \delta]$ with $(a + \delta) < b - \delta$ as follows:

$$\Phi_{[a,b]}^{(\delta,n-1)}(x) = \begin{cases} \varphi_{g_n}^L(\frac{x-(a+\delta)}{2\delta}) & \text{if } x \in [a - \delta, a + \delta] \\ 1 & \text{if } x \in [a + \delta, b - \delta] \\ \varphi_{g_n}^R(\frac{x-(b-\delta)}{2\delta}) & \text{if } x \in [b - \delta, b + \delta] \\ 0 & \text{if } x \notin [a - \delta, b + \delta]. \end{cases} \quad (2.13)$$

Note that we assume that $\delta \leq \frac{b-a}{3}$ to make a PU function have a flat-top.

2.4 Weak solution in Sobolev space

For an integer $k \geq 0$, we also use the usual Sobolev space denoted by $H^k(\Omega)$. For $u \in H^k(\Omega)$, the norm and the semi-norm, respectively, are

$$\|u\|_{k,\Omega} = \left(\sum_{|\alpha| \leq k} \int_{\Omega} |\partial^{\alpha} u|^2 dx \right)^{1/2}, \quad \|u\|_{k,\infty,\Omega} = \max_{|\alpha| \leq k} \{ \text{ess.sup} |\partial^{\alpha} u(x)| : x \in \Omega \};$$

$$|u|_{k,\Omega} = \left(\sum_{|\alpha|=k} \int_{\Omega} |\partial^{\alpha} u|^2 dx \right)^{1/2}, \quad |u|_{k,\infty,\Omega} = \max_{|\alpha|=k} \{ \text{ess.sup} |\partial^{\alpha} u(x)| : x \in \Omega \}.$$

Suppose we are concerned with an elliptic boundary value problem on a domain Ω with Dirichlet boundary condition $g(x, y)$ along the boundary $\partial\Omega$. Let

$$\mathcal{W} = \{w \in H^1(\Omega) : w|_{\partial\Omega} = g\} \text{ and } \mathcal{V} = \{w \in H^1(\Omega) : w|_{\partial\Omega} = 0\}.$$

The variational formulation of the Dirichlet boundary value problem can be written as: Find $u \in \mathcal{W}$ such that

$$\mathcal{B}(u, v) = \mathcal{L}(v), \text{ for all } v \in \mathcal{V}, \quad (2.14)$$

where \mathcal{B} is a continuous bilinear form that is \mathcal{V} -elliptic ([15]) and \mathcal{L} is a linear functional. The solution to (2.14) is called a **weak solution** which is equivalent to the strong (classical) solution corresponding elliptic PDE whenever u is smooth enough. The energy norm of the trial function u is defined by

$$\|u\|_{\text{eng}} = \left[\frac{1}{2} \mathcal{B}(u, u) \right]^{1/2}. \quad (2.15)$$

Let $\mathcal{W}^h \subset \mathcal{W}$, $\mathcal{V}^h \subset \mathcal{V}$ be finite dimensional subspaces. Since the NURBS basis

functions do not satisfy the Kronecker delta property, in this paper we approximate the non-homogeneous Dirichlet boundary condition by the least squares method as follows: $g^h \in \mathcal{W}^h$ such that

$$\int_{\partial\Omega} |g - g^h|^2 d\gamma = \text{minimum.}$$

We can write the Galerkin form (a discrete variational equation) of (2.14) as follows: Given g^h , find $u^h = w^h + g^h$, where $w^h \in \mathcal{V}^h$, such that

$$\mathcal{B}(u^h, v^h) = \mathcal{L}(v^h), \text{ for all } v^h \in \mathcal{V}^h,$$

which can be rewritten as: Find the trial function $w^h \in \mathcal{V}^h$ such that

$$\mathcal{B}(w^h, v^h) = \mathcal{L}(v^h) - \mathcal{B}(g^h, v^h), \text{ for all test functions } v^h \in \mathcal{V}^h. \quad (2.16)$$

For the relative error (%) of the computed solutions in L_∞ and L_2 -norm, we define them as follow:

$$\|u - u^h\|_{\infty, \text{rel}}(\%) = \frac{\|u - u^h\|_\infty}{\|u\|_\infty} \times 100, \quad \|u - u^h\|_{L_2, \text{rel}}(\%) = \frac{\|u - u^h\|_{L_2}}{\|u\|_{L_2}} \times 100, \quad (2.17)$$

2.5 Elasticity

In this section, we briefly introduce the notations and equilibrium equations for elastic materials. In elasticity, the displace field is denoted by $\{u\} = \{u_x(x, y), u_y(x, y)\}^T$ and the stress field is denoted by $\{\sigma\} = \{\sigma_x, \sigma_y, \tau_{xy}\}^T$. Let $\{\varepsilon\} = \{\varepsilon_x, \varepsilon_y, \gamma_{xy}\}^T$ be the strain field. Then the strain-displacement and the stress-strain relations are given by

$$\{\varepsilon\} = [D]\{u\}, \quad \{\sigma\} = [E]\{\varepsilon\}, \quad (2.18)$$

respectively, where $[D]$ is the differential operator matrix,

$$[D] = \begin{bmatrix} \frac{\partial}{\partial x} & 0 \\ 0 & \frac{\partial}{\partial y} \\ \frac{\partial}{\partial y} & \frac{\partial}{\partial x} \end{bmatrix}$$

and $[E]$ is the 3×3 symmetric positive definite matrix of material constants. Material constants are classified by the property of the material. For an isotropic elastic body,

$$[E] = \frac{E}{1-\nu^2} \begin{bmatrix} 1 & \nu & 0 \\ \nu & 1 & 0 \\ 0 & 0 & \frac{1-\nu}{2} \end{bmatrix} \quad \text{for plane stress,}$$

$$[E] = \begin{bmatrix} \zeta + 2\mu & \zeta & 0 \\ \zeta & \zeta + 2\mu & 0 \\ 0 & 0 & \mu \end{bmatrix} \quad \text{for plane strain.}$$

Here,

$$\mu = \frac{E}{2(1+\nu)}, \quad \zeta = \frac{\nu E}{(1+\nu)(1-2\nu)},$$

where E is the Young's modulus of elasticity and ν ($0 \leq \nu \leq 1/2$) is Poisson's ratio.

The equilibrium equations of elasticity are

$$[D]^T \{\sigma\}(x, y) + \{f\}(x, y) = 0, \quad (x, y) \in \Omega, \quad (2.19)$$

where $\{f\} = \{f_x(x, y), f_y(x, y)\}^T$ is the vector of internal sources representing the body force per unit area.

The equilibrium equations (2.19) can be expressed in terms of the displacement field $\{u\}$ through the relations (2.18). Then we consider the following system of

elliptic differential equations in terms of the displacement field,

$$[D]^T[E][D]\{u\}(x, y) + \{f\}(x, y) = 0, \quad (x, y) \in \Omega, \quad (2.20)$$

subject to the boundary conditions,

$$[N] \{\sigma\}(s) = \{\tilde{T}\}(s) = \{\bar{T}\}(s) = \{\bar{T}_x(s), \bar{T}_y(s)\}^T, \quad s \in \Gamma_N, \quad (2.21)$$

$$\{u\}(s) = \{\bar{u}\}(s) = \{\bar{u}_x(s), \bar{u}_y(s)\}^T, \quad s \in \Gamma_D, \quad (2.22)$$

where $\Gamma_N \cup \Gamma_D = \partial\Omega$,

$$[N] = \begin{bmatrix} n_x & 0 & n_y \\ 0 & n_y & n_x \end{bmatrix},$$

$\{n_x, n_y\}^T$ is a unit vector normal to the boundary $\partial\Omega$ of the domain Ω .

For the Galerkin approximation to the equilibrium equations in terms of displacement field (2.20), the variational form of (2.20) through (2.21) is:

find the vector $\{u\}$ such that $u_x, u_y \in H^1(\Omega)$, $\{u\} = \{\bar{u}\}$ on Γ_D , and

$$\mathcal{B}(\{u\}, \{v\}) = \mathcal{F}(\{v\}), \quad \text{for all } \{v\} \in H_0^1(\Omega), \quad (2.23)$$

where

$$\begin{aligned} \mathcal{B}(\{u\}, \{v\}) &= \int_{\Omega} ([D]\{v\})^T [E]([D]\{u\}) dx dy, \\ \mathcal{F}(\{v\}) &= \int_{\Omega} \{v\}^T \{f\} dx dy + \oint_{\Gamma_N} \{v\}^T \{\bar{T}\} ds \end{aligned}$$

The finite element approximation of the solution of (2.23) is to construct approximations of each component of the vector $\{u\}$.

CHAPTER 3: MAPPING TECHNIQUES FOR IGA

3.1 NURBS geometrical mappings by which push-forward of B-spline functions generate singular functions

In this section, we construct a NURBS geometrical mapping to deal with monotone singularity of type $r^q\psi(\theta)$, where q is a rational number with $0 < q < 1$, $\psi(\theta)$ is a piecewise smooth function, (r, θ) is the polar coordinates. The construction presented in this section is similar to those in [29]. We refer to this reference for the details.

3.1.1 Mapping methods to handle singularities

The geometrical mappings we are concerned with are the NURBS surfaces defined in Chapter 2. Suppose the physical domain Ω is a unit disk with a crack along the positive x -axis as shown in Fig. 3.1. We now consider a NURBS geometrical mapping from the parameter space $\widehat{\Omega} = [0, 1] \times [0, 1]$ to the physical domain Ω . Consider the knot vectors:

$$\Xi_\xi = \left\{ 0, 0, 0, \frac{1}{4}, \frac{1}{4}, \frac{1}{2}, \frac{1}{2}, \frac{3}{4}, \frac{3}{4}, 1, 1, 1 \right\}, \quad \Xi_\eta = \underbrace{\{0, 0, \dots, 0\}}_{p_\eta+1}, \underbrace{\{1, 1, \dots, 1\}}_{p_\eta+1}.$$

Here, if the function to be approximated has a singularity of type $\mathcal{O}(r^q)$ with $0 < q = n_q/m_q < 1$, where $n_q, m_q \in \mathbb{Z}$, then the polynomial degree of B-spline functions corresponding to Ξ_η is $p_\eta = m_q$.

Let $N_{i,3}(\xi)$, $i = 1, \dots, 9$ be the B-splines corresponding to the knot vector Ξ_ξ and let $M_{j,p_\eta+1}(\eta)$, $j = 1, \dots, p_\eta + 1$ be the B-splines corresponding to the knot vector

Ξ_η . Then these B-spline functions are

$$\begin{aligned}
N_{1,3}(\xi) &= \begin{cases} (1-4\xi)^2 & \text{if } \xi \in [0, \frac{1}{4}] \\ 0 & \text{if } \xi \notin [0, \frac{1}{4}] \end{cases} & N_{2,3}(\xi) &= \begin{cases} 8\xi(1-4\xi) & \text{if } \xi \in [0, \frac{1}{4}] \\ 0 & \text{if } \xi \notin [0, \frac{1}{4}] \end{cases} \\
N_{3,3}(\xi) &= \begin{cases} (4\xi)^2 & \text{if } \xi \in [0, \frac{1}{4}] \\ (2-4\xi)^2 & \text{if } \xi \in [\frac{1}{4}, \frac{1}{2}] \\ 0 & \text{if } \xi \notin [0, \frac{1}{2}] \end{cases} & N_{4,3}(\xi) &= \begin{cases} 2(4\xi-1)(2-4\xi) & \text{if } \xi \in [\frac{1}{4}, \frac{1}{2}] \\ 0 & \text{if } \xi \notin [\frac{1}{4}, \frac{1}{2}] \end{cases} \\
N_{5,3}(\xi) &= \begin{cases} (4\xi-1)^2 & \text{if } \xi \in [\frac{1}{4}, \frac{1}{2}] \\ (3-4\xi)^2 & \text{if } \xi \in [\frac{1}{2}, \frac{3}{4}] \\ 0 & \text{if } \xi \notin [\frac{1}{4}, \frac{3}{4}] \end{cases} & N_{6,3}(\xi) &= \begin{cases} 2(4\xi-2)(3-4\xi) & \text{if } \xi \in [\frac{1}{2}, \frac{3}{4}] \\ 0 & \text{if } \xi \notin [\frac{1}{2}, \frac{3}{4}] \end{cases} \\
N_{7,3}(\xi) &= \begin{cases} (4\xi-2)^2 & \text{if } \xi \in [\frac{1}{2}, \frac{3}{4}] \\ (4-4\xi)^2 & \text{if } \xi \in [\frac{3}{4}, 1] \\ 0 & \text{if } \xi \notin [\frac{1}{2}, 1] \end{cases} & N_{8,3}(\xi) &= \begin{cases} 8(4\xi-3)(1-\xi) & \text{if } \xi \in [\frac{3}{4}, 1] \\ 0 & \text{if } \xi \notin [\frac{3}{4}, 1] \end{cases} \\
N_{9,3}(\xi) &= \begin{cases} (4\xi-3)^2 & \text{if } \xi \in [\frac{3}{4}, 1] \\ 0 & \text{if } \xi \notin [\frac{3}{4}, 1] \end{cases}
\end{aligned} \tag{3.1}$$

$$M_{j,p_\eta+1}(\eta) = \binom{p_\eta}{j-1} \eta^{j-1} (1-\eta)^{p_\eta-j+1} \text{ for } j = 1, \dots, p_\eta + 1, \quad \eta \in [0, 1]. \tag{3.2}$$

Here, the B-spline functions $M_{j,p_\eta+1}$, $j = 1, \dots, p_\eta + 1$, corresponding to the open knot vector Ξ_η are also called the Bernstein polynomials of degree p_η .

Consider the control points $\mathbf{B}_{i,j}$ and the weights $w_{i,j}$ for $1 \leq i \leq 9$, $1 \leq j \leq p_\eta + 1$, that are listed in Table 3.1. With the B-spline functions shown in (3.1) and (3.2), the $9(p_\eta + 1)$ control points and weights, we now construct a NURBS geometrical mapping from the parameter space $\widehat{\Omega}$ onto Ω as follows:

$$\mathbf{F}(\xi, \eta) = \sum_{i=1}^9 \sum_{j=1}^{p_\eta+1} R_{i,j}(\xi, \eta) \mathbf{B}_{i,j}.$$

Table 3.1: Control points $\mathbf{B}_{i,j}$ and weights $w_{i,j}$.

	$1 \leq j \leq p_\eta$		$j = p_\eta + 1$	
i	$\mathbf{B}_{i,j}$	$w_{i,j}$	$\mathbf{B}_{i,j}$	$w_{i,j}$
1	(0, 0)	1	(1, 0)	1
2	(0, 0)	$\frac{1}{\sqrt{2}}$	(1, -1)	$\frac{1}{\sqrt{2}}$
3	(0, 0)	1	(0, -1)	1
4	(0, 0)	$\frac{1}{\sqrt{2}}$	(-1, -1)	$\frac{1}{\sqrt{2}}$
5	(0, 0)	1	(-1, 0)	1
6	(0, 0)	$\frac{1}{\sqrt{2}}$	(-1, 1)	$\frac{1}{\sqrt{2}}$
7	(0, 0)	1	(0, 1)	1
8	(0, 0)	$\frac{1}{\sqrt{2}}$	(1, 1)	$\frac{1}{\sqrt{2}}$
9	(0, 0)	1	(1, 0)	1

Here $R_{i,j}(\xi, \eta)$, $1 \leq i \leq 9$, $1 \leq j \leq p_\eta + 1$, are NURBS basis functions defined by

$$R_{i,j}(\xi, \eta) = \frac{N_{i,3}(\xi)M_{j,p_\eta+1}(\eta)w_{i,j}}{W(\xi, \eta)},$$

where

$$W(\xi, \eta) = \sum_{s=1}^9 \sum_{t=1}^{p_\eta+1} N_{s,3}(\xi)M_{t,p_\eta+1}(\eta)w_{s,t}.$$

Noting that from Table 3.1, $w_{s,j} = 1$ if $s = 1, 3, 5, 7, 9$ and $w_{s,j} = 1/\sqrt{2}$ if $s = 2, 4, 6, 8$, and using the partition of unity property: $\sum_{t=1}^{p_\eta+1} M_{t,p_\eta+1}(\eta) = 1$, we have

$$\begin{aligned} W(\xi, \eta) &= \sum_{s=1}^9 N_{s,3}(\xi) \left[\sum_{t=1}^{p_\eta+1} M_{t,p_\eta+1}(\eta)w_{s,t} \right] \\ &= [N_{2,3}(\xi) + N_{4,3}(\xi) + N_{6,3}(\xi) + N_{8,3}(\xi)] / \sqrt{2} \\ &\quad + [N_{1,3}(\xi) + N_{3,3}(\xi) + N_{5,3}(\xi) + N_{7,3}(\xi) + N_{9,3}(\xi)] \\ &\equiv w(\xi), \end{aligned} \tag{3.3}$$

which becomes a function of ξ only. Since $\mathbf{B}_{i,j} = (0, 0)$ for all i and $j \leq p_\eta$ from Table

3.1, we have

$$\mathbf{F}(\xi, \eta) = \eta^{p_\eta} \sum_{i=1}^9 \frac{N_{i,3}(\xi)w_{i,3}}{w(\xi)} \mathbf{B}_{i,p_\eta+1} := (x(\xi, \eta), y(\xi, \eta)),$$

where the coordinate functions are as follows:

$$\begin{cases} x(\xi, \eta) = \frac{\eta^{p_\eta}}{w(\xi)} \left[N_{1,3} + N_{2,3}/\sqrt{2} - N_{4,3}/\sqrt{2} - N_{5,3} - N_{6,3}/\sqrt{2} + N_{8,3}/\sqrt{2} + N_{9,3} \right] (\xi) \\ \quad = \eta^{p_\eta} \left(\frac{X(\xi)}{w(\xi)} \right), \\ y(\xi, \eta) = \frac{\eta^{p_\eta}}{w(\xi)} \left[-N_{2,3}/\sqrt{2} - N_{3,3} - N_{4,3}/\sqrt{2} + N_{6,3}/\sqrt{2} + N_{7,3} + N_{8,3}/\sqrt{2} \right] (\xi) \\ \quad = \eta^{p_\eta} \left(\frac{Y(\xi)}{w(\xi)} \right). \end{cases} \quad (3.4)$$

Moreover, by substituting (3.1) into (3.3), one can show that the total weight function $W(\xi, \eta)$ is bounded away from zero:

$$\frac{2 + \sqrt{2}}{4} \leq W(\xi, \eta) \equiv w(\xi) \leq 1. \quad (3.5)$$

Lemma 3.1 of [29] is now generalized as follows:

Lemma 3.1.1. *Suppose $u(r, \theta) = r^q \psi(\theta)$ for a positive rational number $q = n_q/m_q$, where n_q and m_q are integers, and for a smooth function ψ , where (r, θ) is the polar coordinates. If we choose $p_\eta = m_q$ for the geometrical mapping \mathbf{F} of (3.4), then we have the following:*

1. $r^q \circ \mathbf{F}(\xi, \eta) = \eta^{n_q}$ is a polynomial in η .
2. Let $\Psi(\xi) = \psi \circ \mathbf{F}(\xi, \eta)$. Then $\Psi(\xi) \in \mathcal{C}^0[0, 1]$ and $\Psi(\xi) \in \mathcal{C}^\infty(0, 1)$ unless $\xi = 1/4, 1/2, 3/4$.
3. $|\det(J(\mathbf{F}))| \leq 8p_\eta$.

Proof. 1: From the control points $B_{i,j}$ and the weights $w_{i,j}$ in Table 3.1 and section 2.4.1.1 of [27], we have

$$1 = \left(\frac{X(\xi)}{w(\xi)} \right)^2 + \left(\frac{Y(\xi)}{w(\xi)} \right)^2, \quad (3.6)$$

From (3.6), the pull-back of r^q onto $\widehat{\Omega}$ becomes

$$r^q \circ \mathbf{F}(\xi, \eta) = \eta^{n_q} \left[\left(\frac{X(\xi)}{w(\xi)} \right)^2 + \left(\frac{Y(\xi)}{w(\xi)} \right)^2 \right]^{q/2} = \eta^{n_q}.$$

2: The proof of the second part is similar to that of [29].

3: By (3.4), we have

$$\begin{aligned} |\det(J(\mathbf{F}))| &= \left| \frac{\partial x}{\partial \xi} \frac{\partial y}{\partial \eta} - \frac{\partial x}{\partial \eta} \frac{\partial y}{\partial \xi} \right| = \frac{p_\eta \eta^{2p_\eta - 1}}{w(\xi)^2} |X'(\xi)Y(\xi) - X(\xi)Y'(\xi)|, \\ X'(\xi)Y(\xi) - X(\xi)Y'(\xi) &= \sum_{i=0}^3 [(X'(\xi)Y(\xi) - X(\xi)Y'(\xi))\chi_{[i/4, (i+1)/4]}(\xi)]. \end{aligned} \quad (3.7)$$

By (3.1), we have

$$2(1+\sqrt{2}) \leq |(X'(\xi)Y(\xi) - X(\xi)Y'(\xi))\chi_{[i/4, (i+1)/4]}(\xi)| \leq 4\sqrt{2}, \text{ for } i = 0, 1, 2, 3. \quad (3.8)$$

Applying the lower bound of $w(\xi)$ of (3.5) and the upper bound (3.8) to the bound of determinant (3.7), we obtain

$$|\det(J(\mathbf{F}))| \leq 32p_\eta\sqrt{2}(3 - 2\sqrt{2}) \leq 8p_\eta. \quad (3.9)$$

□

Lemma 3.1.1 shows that the pull-back of a singular function $r^q\psi(\theta)$ by the NURBS mapping \mathbf{F} becomes a piecewise smooth function on the parameter space $\widehat{\Omega}$.

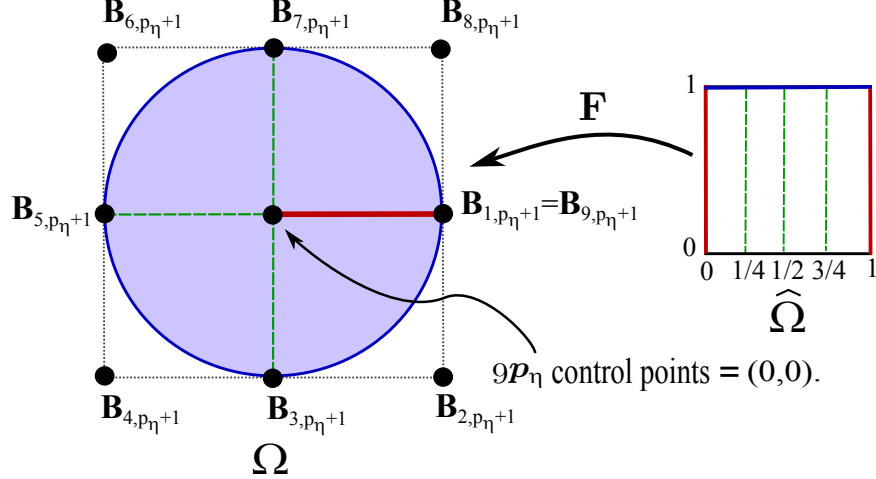


Figure 3.1: The parameter space and the physical domain for the NURBS mapping \mathbf{F} .

3.1.2 Error estimates

The NURBS geometrical mapping $\mathbf{F} : \hat{\Omega} \rightarrow \Omega$ constructed with coarse mesh on $\hat{\Omega} = [0, 1] \times [0, 1]$ in the previous subsection (Fig. 3.1) does not change as the mesh on $\hat{\Omega}$ is further refined. Let

$$\begin{aligned}
 \mathcal{S}^h &\equiv \mathcal{S}(\Xi_\xi, \Xi_\eta, p_\xi^h, p_\eta^h) = \text{span}\{N_{i,p_\xi^h+1}(\xi)M_{j,p_\eta^h+1}(\eta) | 1 \leq i \leq m, 1 \leq j \leq n\}, \\
 \mathcal{S}_\xi^h &\equiv \mathcal{S}(\Xi_\xi, p_\xi^h) = \text{span}\{N_{i,p_\xi^h+1}(\xi) | 1 \leq i \leq m\}, \\
 \mathcal{V}^h &= \text{span}\{[N_{i,p_\xi^h+1}(\xi)M_{j,p_\eta^h+1}(\eta)] \circ \mathbf{F}^{-1} | 1 \leq i \leq m, 1 \leq j \leq n\},
 \end{aligned} \tag{3.10}$$

where $m + (p_\xi^h + 1)$ is the number of knot values in Ξ_ξ and n is similar. Here p_ξ^h and p_η^h , respectively, are the polynomial degrees of B-spline basis functions in the ξ - and the η -directions that are for approximation spaces for IGA of physical domain, whereas in the construction of the geometrical mapping \mathbf{F} , $m = 9$, $n = p_\eta + 1$, $p_\xi = 2$, are fixed. In this section, we assume the following:

- u is the weak solution of (2.14) and u^h is the Galerkin approximate solution of (2.16). Each knot value of the open knot Ξ_ξ has multiplicity p_ξ^h . That is, each

member in \mathcal{S}_ξ^h is a \mathcal{C}^0 -function.

The following error estimates for the mapping method was proved in [29], to which we refer for details:

Theorem 3.1.1. *Let $0 < \lambda = 1/p_\eta \leq 1$. Suppose $u(r, \theta) = \sum_{k=0}^N c_k r^{(\lambda+k)} \psi_k(\theta)$ with smooth functions $\psi_k(\theta)$ solves the Poisson equation in a cracked unit disk. Assume that each node in the open knot vector Ξ_ξ for the approximation space \mathcal{S}_ξ^h has the multiplicity p_ξ . Let $u^h \in \mathcal{V}^h$ be an isogeometric finite element solution of u obtained by the mapping method. Then under some assumptions on mesh size h , polynomial degrees p_ξ, p_η , we have*

$$\|u - u^h\|_{1,\Omega} \leq C_1 h^p \left[\sum_{l=0}^N c_l (|\Psi_l|_{p+1,\infty} + |\Psi_l|_{p+2,\infty}) \right] / (p!). \quad (3.11)$$

$$|u - u^h|_{\infty,\Omega} \leq C_\infty h^{p+1} \left[\sum_{l=0}^N c_l (|\Psi_l|_{p+1,\infty} + |\Psi_l|_{p+2,\infty}) \right] / (p!), \quad (3.12)$$

$$\|u - u^h\|_{0,\Omega} \leq C_0 h^{p+1} \left[\sum_{l=0}^N c_l (|\Psi_l|_{p+1,\infty} + |\Psi_l|_{p+2,\infty}) \right] / (p!). \quad (3.13)$$

$\Psi_l = \psi_l \circ \mathbf{F}$, and $|\Psi_l|_{p+i,\infty} := \sum_k |\Psi_l|_{p+i,\infty,I_k}$, where Ψ_l is smooth on I_k , for each k and $\cup_k I_k = [0, 1]$. Here $p = p_\xi^h$ is the polynomial degree of $N_{i,p+1}(\xi)$ for an approximation of the angular direction (the polynomial degree $p_\eta^h \geq 2$ for an approximation of the radial direction is held fixed), and $h = \max\{|\xi_{i+1} - \xi_i|\}$ is the maximum length of knot spans of the open knot vector Ξ_ξ and the constants C_∞, C_0, C_1 are independent of h and p .

3.2 Numerical tests

3.2.1 The wedge shaped plates

Tests of the mapping method to the Laplace equation in the wedge domains [29] are extended to the following elasticity equation.

Example 3.2.1. *Consider a load free linear elasticity equation in a wedge-shaped domain as shown in Fig. 3.3,*

$$\Omega^{\pm\alpha} = \{(r, \theta) : r \leq 2, -\alpha \leq \theta \leq \alpha\}, \quad 0 \leq \alpha \leq 90^\circ,$$

which is isotropic with Young's modulus $E = 1000$ and Poisson ratio $\nu = 0.3$ ([49]). The displacement field given below in polar coordinate satisfies the equations of elasticity in the domain $\Omega_2^{\pm\alpha}$.

$$\begin{aligned} u_r(r, \theta) &= \frac{r^\lambda}{2G} \{-(\lambda + 1)\phi(\theta)\} \\ u_\theta(r, \theta) &= \frac{r^\lambda}{2G} \{\phi'(\theta)\} \end{aligned} \tag{3.14}$$

where

$$\lambda = 90^\circ/\alpha - 1, \quad \phi(\theta) = \sin(\lambda + 1)\theta, \quad G = \frac{E}{2(1 + \nu)}.$$

For the construction of the singular geometrical mapping from the parameter space $\hat{\Omega} = [0, 1] \times [0, 1]$ onto the wedge domain $\Omega^{(\pm\alpha)}$, we use the NURBS corresponding to the knot vectors, the control points, and the weights listed in Table C.1 in Appendix, which is similar to Table 15 of [29]. The computational results by the mapping method are plotted in Fig. 3.2, in which the relative errors in energy norm is followed by (2.15).

From the test of the mapping method to these elasticity problems containing singularities with various intensity, we have the following:

1. Similarly to the results obtained by MAM shown in [49], the mapping methods yield highly accurate solutions no matter how strong singularity the problems have.
2. By the error estimates (3.11), (3.12), and (3.13) of the mapping method, we have

$$\log \|u - u^h\|_{1,\Omega} \approx p \log h + C_1 \quad (3.15)$$

$$\log |u - u^h|_\infty \approx (p + 1) \log h + \log C_\infty, \quad (3.16)$$

$$\log \|u - u^h\|_0 \approx (p + 1) \log h + \log C_0. \quad (3.17)$$

Actually, if we plot relative errors of displacement functions in the energy norm versus mesh size h , the convergence profile has a slope $p = 2$ as shown in Fig. 3.2(a). Thus, this numerical results follow the error estimate (3.11). On the other hand, if the relative errors of displacement functions in then energy norm are plotted with respect to p -degrees, the slope become $\log h = -0.30103$, $h = 0.5$, as shown on Fig. 3.2(b). In other words, the numerical results support the theory (3.11).

3. Also, relative errors of displacement functions in the maximum norm and L_2 -norm versus mesh size h are depicted in Figs. B.2 and B.3 with $p = 2$, and Figs. B.1 and B.4 with $p = 3$. The convergence profiles have slopes 3 and 4 as shown in Figs. B.2, B.3 and Figs. B.1, B.4, respectively. From these figures, therefore, we can see that our numerical results support the error estimate (3.12) and (3.13).
4. In Fig. 3.2, if the elasticity problem has a crack singularity ($\lambda = 1/2$), then the computed strain energy is virtually the true strain every up to the machine error when the p -degree is 14 (note: $100 \times (\text{the true energy} - \text{the computed energy})^{1/2} =$

10^{-5}).

The mapping method presented above is effective when approximation functions are non-rational B-splines. Moreover, the mapping method may not be effective for the h -refinement.

The solution method for Example 3.2.1 is actually not a genuine IGA, but a conventional finite element analysis (FEA) using B-spline approximation functions. In the following section, using the mapping method for the construction of auxiliary enrichment functions, we combine the mapping method with IGA so that the genuine IGA with k -refinement can effectively handle the corner singularities as well as the jump boundary data singularities.

Next we test our mapping methods to other prominent singularity problems. However, the error analysis of Theorem 3.1.1 is not applicable to these cases because we use two Bézier segments in the η -direction when we construct NURBS geometrical mappings, and apply p -refinement to not only ξ -direction but also η -direction. Nevertheless, we observe that numerical results of these examples have good accuracies.

3.2.2 The curved domain

In this subsection, we consider an elasticity with more practical geometry containing singularity of the type $r^{\frac{1}{2}}\psi(\theta)$. The control net and the physical elements are illustrated in Fig. 3.4. In order to capture the behavior of the singularity, we construct a NURBS geometrical mapping by choosing quadratic B-spline functions in the η -direction.

The control points and the corresponding weights to construct the geometrical mapping for the curved domain are listed in Table C.2 in Appendix.

Example 3.2.2. (*curved domain*) Let Ω_C be the physical domain as shown in Fig.

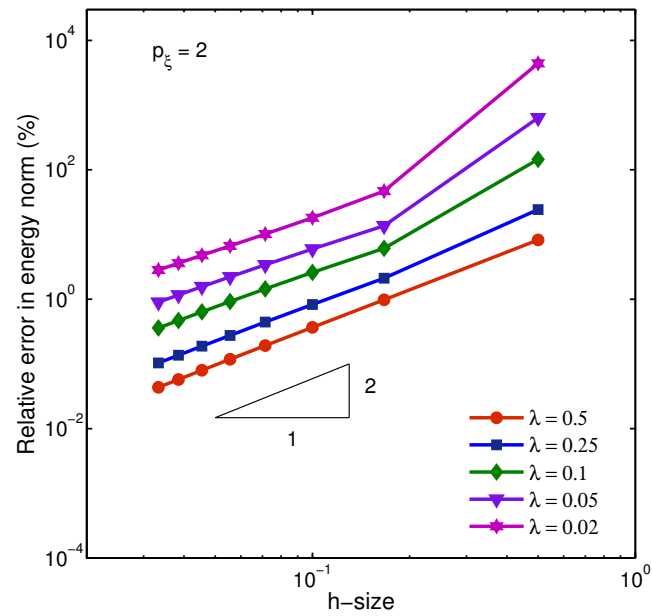
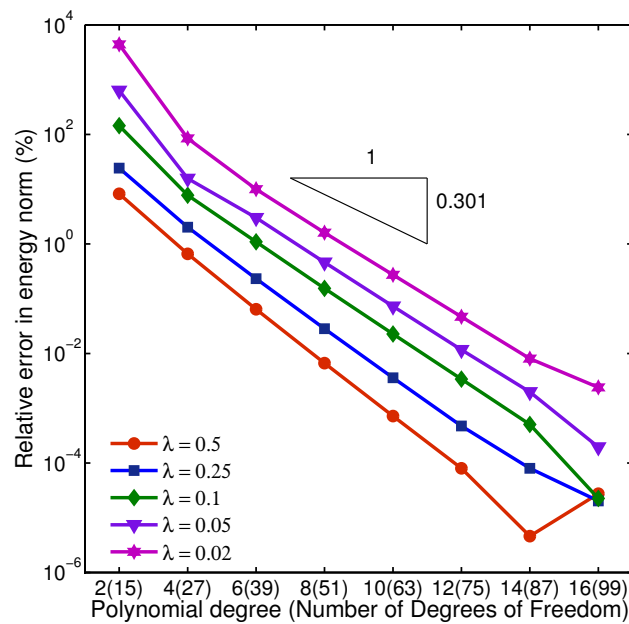
(a) *Rel error in energy norm vs h -size:*(b) *Rel error in energy norm vs polynomial degree:*

Figure 3.2: (a) The relative errors in the energy norm $\times 100$ versus the h -sizes with $p_\xi = 2$ fixed. (b) The relative errors in the energy norm $\times 100$ versus polynomial degree p_ξ (number of degrees of freedom) with $h = 1/2$ fixed.

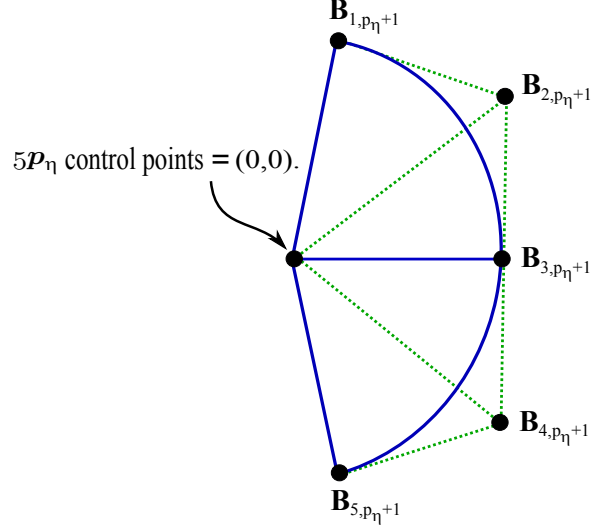


Figure 3.3: The control points for the wedge-shaped domain.

3.4. and let

$$\begin{aligned}
 u(r, \theta) &= r^{1/2} \left\{ \sin\left(\frac{\theta}{2}\right) + \cos\left(\frac{\theta}{2}\right) + \sin\left(\frac{3\theta}{2}\right) + \cos\left(\frac{3\theta}{2}\right) \right\} \\
 v(r, \theta) &= r^{1/2} \left\{ \sin\left(\frac{5\theta}{2}\right) + \cos\left(\frac{5\theta}{2}\right) + \sin\left(\frac{7\theta}{2}\right) + \cos\left(\frac{7\theta}{2}\right) \right\}
 \end{aligned} \tag{3.18}$$

be a displacement field, with Young's modulus $E = 1000$ and Poisson's ratio $\nu = 0.3$.

We assume that the Ω_C is the configuration of an isotropic plane stress plate.

For the numerical solutions of Example 3.2.2, we use the p -refinement in both ξ and η -directions. Therefore, the error bounds in the maximum norm, L_2 -norm, and energy norm for Example 3.2.2 should be expressed in terms of p_{ξ}, p_{η} , and h . Notwithstanding, we observe that the convergence profiles in the maximum norm, L_2 -norm, and energy norm depicted in Figs. 3.5 and 3.6 almost support Theorem 3.1.1 from the following aspects:

1. In Fig. 3.5(a), the convergence profile for relative errors (%) in the maximum norm and L_2 -norm of computed displacement field $\{u, v\}^T$ almost reaches a slope $\log 0.25 = -0.602$, $h = 0.25$

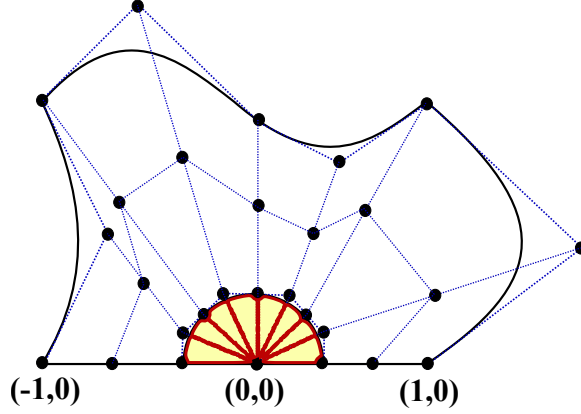


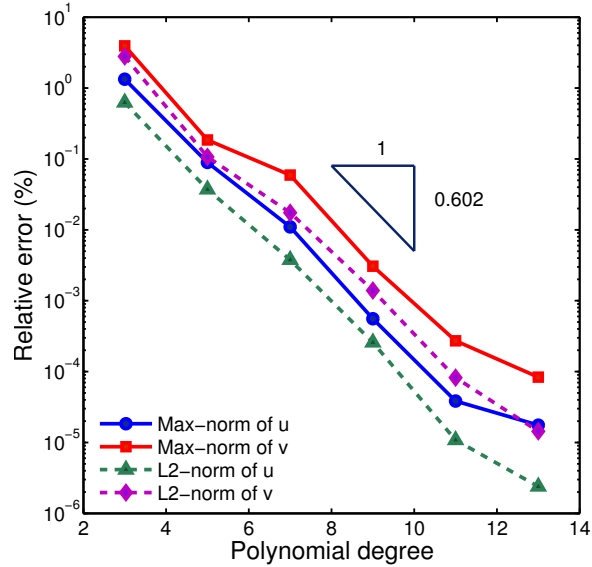
Figure 3.4: Curved physical domain and control net

2. Similarly, The convergence profile for relative errors (%) in the maximum norm of computed stress field $\{\sigma_x, \sigma_y, \tau_{xy}\}^T$ is almost same as a slope $\log 0.25 = -0.602$, $h = 0.25$ in Fig. 3.5(b).
3. In Fig. 3.6, we assume that the computed strain energy at $p_\xi = p_\eta = 14$ is the true strain energy. It is agreeable that the convergence profile for the relative error (%) in energy norm has a slope $\log 0.25 = -0.602$, $h = 0.25$.

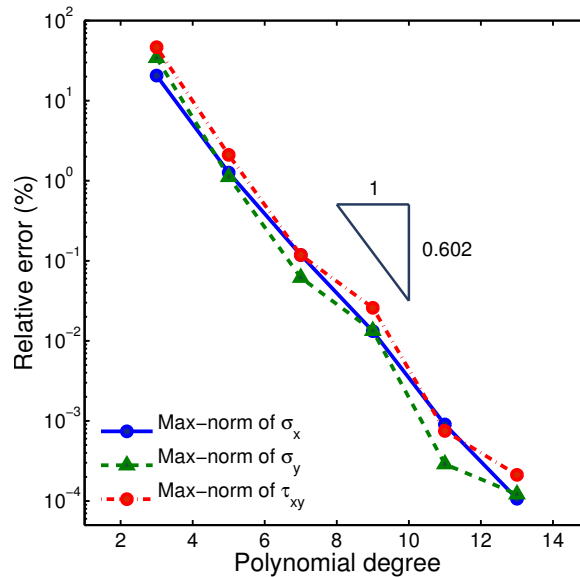
3.2.3 The single edge cracked elastic domain

Example 3.2.3. (*Single edge cracked elastic domain*) Let us consider the equation of elasticity on a domain $\Omega = \{(r, \theta) : r \leq 2, -\pi \leq \theta \leq \pi\}$ with a crack along the negative x -axis. Assume that Young's modulus $E = 1000$, and Poisson's ratio $\nu = 0.3$. We also assume that the following true stresses are imposed along all boundaries of the given domain 3.7(a).

$$\begin{aligned}\sigma_x &= \frac{1}{4\sqrt{r}} \left(3 \cos \frac{\theta}{2} + \cos \frac{5\theta}{2} \right), \\ \sigma_y &= \frac{1}{4\sqrt{r}} \left(5 \cos \frac{\theta}{2} - \cos \frac{5\theta}{2} \right), \\ \tau_{xy} &= \frac{1}{4\sqrt{r}} \left(\sin \frac{5\theta}{2} - \sin \frac{\theta}{2} \right).\end{aligned}$$



(a) *Rel. error of the u and v in curved domain*



(b) *Rel. error of the σ_x , σ_y , and τ_{xy} in curved domain*

Figure 3.5: (a) The relative error (%) in the maximum norm and L_2 -norm of computed displacement field $\{u, v\}^T$ of the elasticity (3.18) in curved domain. (b) The relative error (%) in the maximum norm of computed stress field $\{\sigma_x, \sigma_y, \tau_{xy}\}^T$ of the elasticity (3.18) in curved domain.

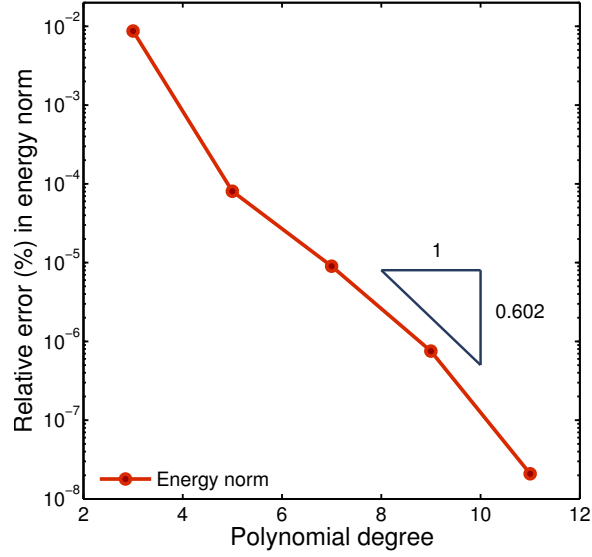


Figure 3.6: The relative error (%) in the strain energy norm of computed displacement field $\{u, v\}^T$ of the elasticity (3.18) in curved domain.

Table 3.2: The relative error in the maximum norm as well as in the L_2 -norm of the computed displacement u and the relative error in the maximum norm of the computed stress σ_x of the elasticity (3.18) in the curved domain Fig. 3.4. The degrees are the polynomial degrees of B-spline functions. Note that the p -refinement is made in the ξ -direction as well as in the η -direction.

(p_ξ, p_η)	dof	$\ u - u^h\ _{\infty, \text{rel}}(\%)$	$\ \sigma_x - \sigma_x^h\ _{\infty, \text{rel}}(\%)$	$\ u - u^h\ _{L_2, \text{rel}}(\%)$
(2, 2)	45	$2.249E - 00$	$2.984E + 01$	$1.619E + 00$
(3, 3)	91	$1.334E - 00$	$2.056E + 01$	$6.254E - 01$
(4, 4)	153	$2.260E - 01$	$1.647E - 00$	$1.144E - 01$
(5, 5)	231	$8.920E - 02$	$1.262E - 00$	$3.720E - 02$
(6, 6)	325	$4.096E - 02$	$6.990E - 01$	$2.108E - 02$
(7, 7)	435	$1.099E - 02$	$1.180E - 01$	$3.776E - 03$
(8, 8)	561	$6.695E - 03$	$1.014E - 01$	$2.180E - 03$
(9, 9)	703	$5.559E - 04$	$1.322E - 02$	$2.577E - 04$
(10, 10)	861	$3.008E - 04$	$8.070E - 03$	$1.140E - 04$
(11, 11)	1035	$3.844E - 05$	$9.042E - 04$	$1.083E - 05$
(12, 12)	1225	$2.165E - 05$	$4.856E - 04$	$9.672E - 06$
(13, 13)	1431	$1.754E - 05$	$1.067E - 04$	$2.393E - 06$
(14, 14)	1653	$5.887E - 06$	$2.131E - 04$	$2.034E - 06$
(15, 15)	1891	$6.795E - 06$	$4.255E - 04$	$1.611E - 07$

Table 3.3: The relative error in the maximum norm as well as in the L_2 -norm of the computed displacement v and the relative error in the maximum norm of the computed stress σ_y of the elasticity (3.18) in the curved domain 3.4. The degrees are the polynomial degrees of B-spline functions. Note that the p -refinement is made in the ξ -direction as well as in the η -direction.

(p_ξ, p_η)	dof	$\ v - v^h\ _{\infty, \text{rel}}(\%)$	$\ \sigma_y - \sigma_y^h\ _{\infty, \text{rel}}(\%)$	$\ v - v^h\ _{L_2, \text{rel}}(\%)$
(2, 2)	45	$9.110E - 00$	$3.765E + 01$	$5.710E + 00$
(3, 3)	91	$3.936E - 00$	$2.056E + 01$	$2.796E - 00$
(4, 4)	153	$7.581E - 01$	$2.546E - 00$	$5.180E - 01$
(5, 5)	231	$1.854E - 01$	$1.117E - 00$	$1.068E - 01$
(6, 6)	325	$1.830E - 01$	$1.265E - 00$	$9.440E - 02$
(7, 7)	435	$5.917E - 01$	$6.163E - 02$	$1.743E - 02$
(8, 8)	561	$2.842E - 02$	$1.641E - 01$	$9.653E - 03$
(9, 9)	703	$3.066E - 03$	$1.336E - 02$	$1.390E - 03$
(10, 10)	861	$1.077E - 03$	$1.108E - 02$	$4.643E - 04$
(11, 11)	1035	$2.718E - 04$	$2.885E - 04$	$8.225E - 05$
(12, 12)	1225	$1.430E - 04$	$3.849E - 04$	$3.941E - 05$
(13, 13)	1431	$8.364E - 05$	$1.212E - 04$	$1.435E - 05$
(14, 14)	1653	$3.361E - 05$	$2.064E - 04$	$8.309E - 06$
(15, 15)	1891	$1.264E - 05$	$3.285E - 04$	$1.550E - 06$

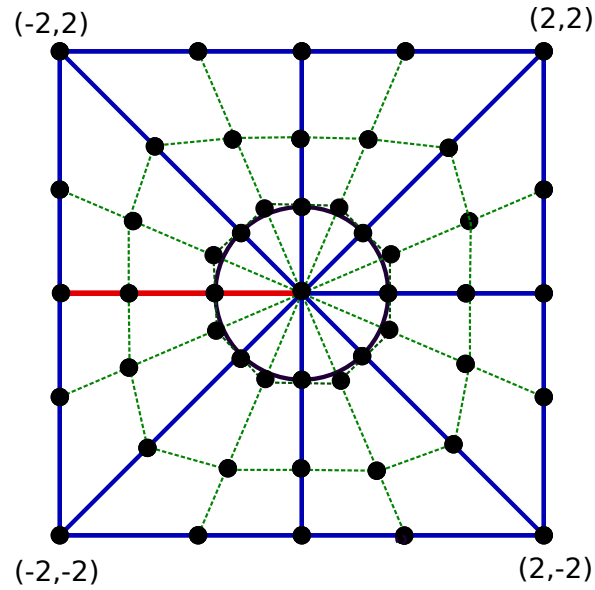
Table 3.4: The relative error(%) in the maximum norm, of the computed stress field (with respect to a p -refinement) of the single edge cracked plate problem are listed.

(p_ξ, p_η)	dof	$\ \sigma_x - \sigma_x^h\ _{\infty, \text{rel}}(\%)$	$\ \sigma_y - \sigma_y^h\ _{\infty, \text{rel}}(\%)$	$\ \tau_{xy} - \tau_{xy}^h\ _{\infty, \text{rel}}(\%)$
(2, 2)	168	$9.963E - 00$	$5.955E - 00$	$1.762E + 01$
(3, 3)	348	$2.525E - 00$	$1.296E - 00$	$2.069E - 00$
(4, 4)	592	$3.376E - 01$	$2.381E - 01$	$4.436E - 01$
(5, 5)	900	$4.691E - 02$	$3.980E - 02$	$4.249E - 02$
(6, 6)	1272	$1.397E - 02$	$1.211E - 02$	$1.517E - 02$
(7, 7)	1708	$4.319E - 03$	$4.914E - 03$	$4.860E - 03$
(8, 8)	2208	$1.435E - 03$	$2.011E - 03$	$1.613E - 03$
(9, 9)	2772	$5.874E - 04$	$8.174E - 04$	$5.740E - 04$
(10, 10)	3400	$2.397E - 04$	$3.304E - 04$	$2.324E - 04$
(11, 11)	4092	$9.754E - 05$	$1.347E - 04$	$9.404E - 05$
(12, 12)	4848	$3.959E - 05$	$5.508E - 05$	$3.803E - 05$
(13, 13)	5668	$1.603E - 05$	$2.246E - 05$	$1.538E - 05$
(14, 14)	6552	$6.490E - 06$	$9.143E - 06$	$6.224E - 06$
(15, 15)	7500	$3.838E - 05$	$6.880E - 05$	$5.119E - 05$
(16, 16)	8512	$1.391E - 04$	$5.340E - 05$	$1.615E - 04$

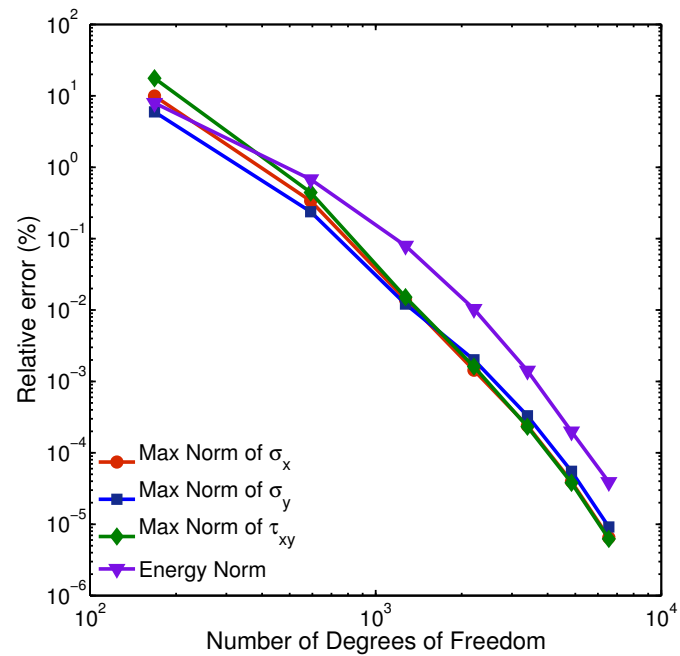
The control points and the corresponding weights to construct the geometrical mapping for the single edge cracked elastic domain are listed in Table C.3 in Appendix.

The relative errors (%) in maximum norm, and energy norm of the computed stress field are shown in Table 3.4 and 3.5.

We observe from Fig. 3.7(b) and Table 3.4 and 3.5 that the mapping method also gives highly accurate analysis for the cracked domain.



(a) *plane stress plate with single edge crack and control points*



(b) *Relative error (%) in max-norm and energy norm*

Figure 3.7: (a) The physical domain and control points of the single edge cracked elastic domain (b) The relative error in the maximum norm for stress field and energy norm versus number of degrees of freedom of computed solutions of the equation of elasticity in the single edge cracked domain Ω .

Table 3.5: The relative error(%) in the energy norm (with respect to a p -refinement) of the single edge cracked plate problem are listed. Note that $\{u\} = \{u_x, u_y\}^T$ is the displacement field.

(p_ξ, p_η)	dof	$\ \{u\} - \{u^h\}\ _{\text{eng,rel}}(\%)$	Computed energy
(2, 2)	168	$7.956E - 00$	$7.181515817987409E - 03$
(3, 3)	348	$2.225E - 00$	$7.223684698964165E - 03$
(4, 4)	592	$6.766E - 01$	$7.226932551320604E - 03$
(5, 5)	900	$2.267E - 01$	$7.227226265109549E - 03$
(6, 6)	1272	$7.953E - 02$	$7.227258841977250E - 03$
(7, 7)	1708	$2.847E - 02$	$7.227262827382460E - 03$
(8, 8)	2208	$1.034E - 02$	$7.227263336186676E - 03$
(9, 9)	2772	$3.807E - 03$	$7.227263403083560E - 03$
(10, 10)	3400	$1.415E - 03$	$7.227263412112890E - 03$
(11, 11)	4092	$5.298E - 04$	$7.227263413357400E - 03$
(12, 12)	4848	$1.986E - 04$	$7.227263413531741E - 03$
(13, 13)	5668	$7.311E - 05$	$7.227263413556409E - 03$
(14, 14)	6552	$3.891E - 05$	$7.227263413559177E - 03$
(15, 15)	7500	$2.965E - 05$	$7.227263413560908E - 03$
(16, 16)	8512	$3.856E - 05$	$7.227263413561346E - 03$
∞			$7.227263413560272E - 03$

CHAPTER 4: ENRICHMENT OF NURBS BASIS FUNCTIONS FOR IGA

4.1 Enrichment of NURBS for IGA with singular functions generated by NURBS geometric mapping

It was stated in the previous Chapter that the mapping method to deal with elliptic problems containing singularities are not effective for NURBS basis functions. It was also pointed out that the mapping methods do not yield optimal results for neither the k -refinement nor the h -refinement. The p -refinement of B-spline (piecewise polynomials) is most suitable for the mapping method. Since NURBS functions used in IGA are generally non-polynomial functions, and the mapping method use the B-spline functions (piecewise polynomials), a direct use of the mapping method in IGA is not expected to yield optimal results.

In this section, we thus consider how to use the proposed mapping method in IGA of elliptic problems containing singularities without changing the design mapping. For this end, we embed the mapping methods into the standard IGA that use NURBS basis functions for which h - p - k -refinements are applicable for improved computational solution. In other words, the mapping methods will be used to enrich NURBS basis functions around neighborhood of singularities so that they can capture the singular behaviors of the function to be approximated. It is similar to that of X-FEM in IGA [45], however we do not introduce any singular functions in the following enrichment method:

Step 1. Selection of subdomains to be enriched and choice of mapping sizes:

Suppose the function to be approximated has singularities at P_k of type $\mathcal{O}(r^{q_k})$

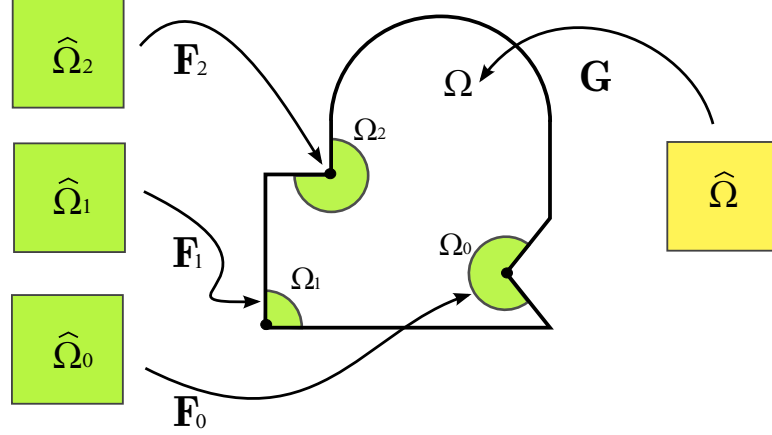


Figure 4.1: \mathbf{G} is a design mapping and $\mathbf{F}_k, k = 0, 1, 2$, are the singular geometrical mappings for the enrichment to capture corner singularities.

with $0 < q_k = \frac{n_k}{m_k} < 1, k = 0, 1, \dots, k_N$, as shown in Fig. 4.1.

- In Fig. 4.1, $\mathbf{G} : \hat{\Omega} \rightarrow \Omega$ is the design mapping and $\mathbf{F}_k : \hat{\Omega} \rightarrow \Omega_k$ is the proposed geometrical mapping constructed in Chapter 3 which maps the parameter space onto a neighborhood Ω_k of a point singularity P_k :

$$\Omega_k = [\{(x, y) \mid \|(x, y) - P_k\| \leq r_k\} \cap \Omega] \setminus \partial\Omega,$$

where $0 < r_k \leq 1$ is not too small so that the solution outside Ω_k has no influence from the singularity at P_k .

- For each k , we choose $p_\eta = m_k$ for control points and weights in Table 4.1 as well as in the knot vector (4.1) for the construction of \mathbf{F}_k .

In what follows, we present the construction of the auxiliary singular mapping \mathbf{F}_0 . The constructions of the remaining $\mathbf{F}_k, k = 1, \dots, k_N$, are similar.

Step 2. Construction of singular mapping \mathbf{F}_0 from the parameter space onto Ω_0 :

Without loss of generality, we assume $\Omega_0 = \{(r, \theta) : r \leq r_0, 0 \leq \theta < 3/2\pi\}$. We modify the singular geometrical mapping $\mathbf{F}_0 : [0, 1] \times [0, 1] \rightarrow \Omega_0$ introduced in Chapter 3 by using the control points, the weights in Table 4.1 as shown in Fig. 4.2

and the following knot vectors:

$$\Xi_\xi = \{0, 0, 0, 1/3, 1/3, 2/3, 2/3, 1, 1, 1\}; \quad (4.1)$$

$$\Xi_\eta = \underbrace{\{0, \dots, 0\}}_{p_\eta+1}, \underbrace{\{\eta_1, \dots, \eta_1\}}_{p_\eta}, \underbrace{\{1, \dots, 1\}}_{p_\eta+1}, \quad \eta_1 = 2/3. \quad (4.2)$$

The B-spline functions corresponding to the knot vector (4.2) are altered to the following $p_\eta + 2$ piecewise polynomials of degrees p_η and 1:

$$\begin{aligned} \widehat{M}_t(\eta) &= M_{t, p_\eta+1}(\eta) \\ &= \binom{p_\eta}{t-1} \left(1 - \frac{\eta}{\eta_1}\right)^{p_\eta-t+1} \left(\frac{\eta}{\eta_1}\right)^{t-1}, \quad \text{if } 1 \leq t \leq p_\eta, 0 \leq \eta \leq \eta_1 \\ \widehat{M}_{p_\eta+1}(\eta) &= \begin{cases} \left(\frac{\eta}{\eta_1}\right)^{p_\eta} & \text{for } 0 \leq \eta \leq \eta_1 \\ \frac{1-\eta}{1-\eta_1} & \text{for } \eta_1 \leq \eta \leq 1, \end{cases} \\ \widehat{M}_{p_\eta+2}(\eta) &= \begin{cases} \frac{\eta-\eta_1}{1-\eta_1} & \text{for } \eta_1 \leq \eta \leq 1 \\ 0 & \text{for } 0 \leq \eta \leq \eta_1. \end{cases} \end{aligned}$$

Note that $\widehat{M}_t, 1 \leq t \leq p_\eta + 1$, are the Bernstein polynomials of degree p_η on $[0, \eta_1]$, and \widehat{M}_t , for $p_\eta + 1 \leq t \leq p_\eta + 2$, are the Bernstein polynomials of degree 1 on $[\eta_1, 1]$.

The partition of unity property of the Bernstein polynomials shows that the total weight is a function of ξ only, and the corresponding NURBS functions are as follows:

$$\begin{aligned} W(\xi, \eta) &= \sum_{s=1}^7 \sum_{t=1}^{p_\eta+2} N_{s,3}(\xi) \widehat{M}_t(\eta) w_{s,t} \\ &= \sum_{s=\text{odd}}^7 \sum_{t=1}^{p_\eta+2} N_{s,3}(\xi) \widehat{M}_t(\eta) w_{s,t} + \sum_{s=\text{even}}^6 \sum_{t=1}^{p_\eta+2} N_{s,3}(\xi) \widehat{M}_t(\eta) w_{s,t} \\ &= \sum_{s=\text{odd}}^7 N_{s,3}(\xi) \sum_{t=1}^{p_\eta+2} \widehat{M}_t(\eta) + \frac{1}{\sqrt{2}} \sum_{s=\text{even}}^6 N_{s,3}(\xi) \sum_{t=1}^{p_\eta+2} \widehat{M}_t(\eta) \end{aligned}$$

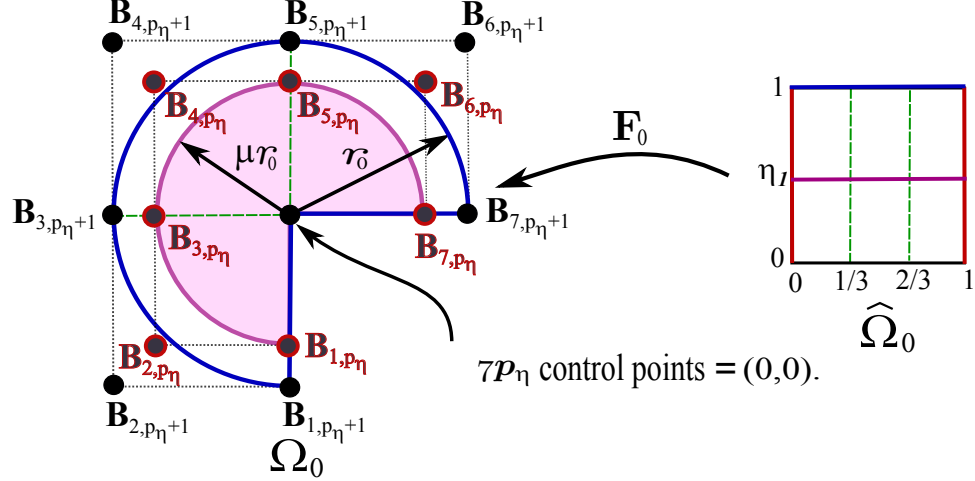


Figure 4.2: The NURBS geometrical mapping that generates singular functions on $\Omega_0 = [0, r_0] \times [0, 3/2\pi]$ from the parameter space $\hat{\Omega}_0 = [0, 1] \times [0, 1]$ to the singular zone Ω_0 . Note that μ is fixed real number with $0.5 \leq \mu \leq 0.9$.

$$\begin{aligned}
 &= \sum_{s=\text{odd}}^7 N_{s,3}(\xi) + \frac{1}{\sqrt{2}} \sum_{s=\text{even}}^6 N_{s,3}(\xi) = w(\xi); \quad (4.3) \\
 R_{i,j}(\xi, \eta) &= N_{i,3}(\xi) \widehat{M}_j(\eta) w_{i,j} / w(\xi), \quad 1 \leq i \leq 7, \quad 1 \leq j \leq p_{\eta} + 2.
 \end{aligned}$$

Thus, by the choice of the control points in Table 4.1, the geometrical mapping becomes

$$\begin{aligned}
 \mathbf{F}_0(\xi, \eta) &= \sum_{i=1}^7 \sum_{j=1}^{p_{\eta}+2} R_{i,j}(\xi, \eta) \mathbf{B}_{i,j} \\
 &= \sum_{i=1}^7 \{ \mathbf{B}_{i,p_{\eta}+1} R_{i,p_{\eta}+1}(\xi, \eta) + \mathbf{B}_{i,p_{\eta}+2} R_{i,p_{\eta}+2}(\xi, \eta) \} \\
 &= \left[\frac{\widehat{M}_{p_{\eta}+1+1}(\eta)}{w(\xi)} \right] \sum_{i=1}^7 N_{i,3}(\xi) w_{i,p_{\eta}+1} \mathbf{B}_{i,p_{\eta}+1} + \\
 &\quad \left[\frac{\widehat{M}_{p_{\eta}+1+2}(\eta)}{w(\xi)} \right] \sum_{i=1}^7 N_{i,3}(\xi) w_{i,p_{\eta}+2} \mathbf{B}_{i,p_{\eta}+2}.
 \end{aligned}$$

Hence, we have

$$\mathbf{F}_0(\xi, \eta) = (x(\xi, \eta), y(\xi, \eta)) = \phi(\eta) \left(\frac{X(\xi)}{w(\xi)}, \frac{Y(\xi)}{w(\xi)} \right),$$

where $X(\xi)$ and $Y(\xi)$ are

$$\begin{cases} X(\xi) = (1 + \mu) \left[-r_0 N_{2,3}/\sqrt{2} - r_0 N_{3,3} - r_0 N_{4,3}/\sqrt{2} + r_0 N_{6,3}/\sqrt{2} + r_0 N_{7,3} \right] (\xi) \\ Y(\xi) = (1 + \mu) \left[r_0 N_{1,3} - r_0 N_{2,3}/\sqrt{2} + r_0 N_{4,3}/\sqrt{2} + r_0 N_{5,3} + r_0 N_{6,3}/\sqrt{2} \right] (\xi), \end{cases} \quad (4.4)$$

and

$$\phi(\eta) = \begin{cases} \phi_1(\eta) = \mu r_0 \left(\frac{\eta}{\eta_1} \right)^{p_\eta}, & \text{if } \eta \in [0, \eta_1], \\ \phi_2(\eta) = \mu r_0 \left[\frac{1 - \eta}{1 - \eta_1} \right] + r_0 \left[\frac{\eta - \eta_1}{1 - \eta_1} \right], & \text{if } \eta \in [\eta_1, 1] \end{cases}$$

Moreover, the determinant of Jacobian of \mathbf{F}_0 is

$$\begin{aligned} |\det(J(\mathbf{F}_0))| &= \left| \frac{\partial x}{\partial \xi} \frac{\partial y}{\partial \eta} - \frac{\partial x}{\partial \eta} \frac{\partial y}{\partial \xi} \right| = \frac{h(\eta) |X'(\xi)Y(\xi) - X(\xi)Y'(\xi)|}{(w(\xi))^2} \\ h(\eta) &= \begin{cases} \phi_1 \frac{d\phi_1}{d\eta} = [\mu r_0]^2 \frac{p_\eta}{\eta_1} \left(\frac{\eta}{\eta_1} \right)^{2p_\eta - 1}, & \text{if } \eta \in [0, \eta_1], \\ \phi_2 \frac{d\phi_2}{d\eta} = \left[\frac{(1 - \mu)r_0}{1 - \eta_1} \right] \left[\mu r_0 \left[\frac{1 - \eta}{1 - \eta_1} \right] + r_0 \left[\frac{\eta - \eta_1}{1 - \eta_1} \right] \right], & \text{if } \eta \in [\eta_1, 1]. \end{cases} \end{aligned}$$

Therefore, the NURBS geometrical mapping corresponding to the knot vectors, control points, and weights of Table 4.1 with $\eta_1 = 2/3$, $\mu = 0.8$, $p_\eta = 3$, is given by

$$\mathbf{F}_0(\xi, \eta) = \phi(\eta) \left(\frac{X(\xi)}{w(\xi)}, \frac{Y(\xi)}{w(\xi)} \right),$$

where

$$\phi(\eta) = \begin{cases} \phi_1(\eta) = [0.8r_0(\frac{3}{2})^2]\eta^3, & \text{if } \eta \in [0, 2/3], \\ \phi_2(\eta) = 0.8r_0 \left[\frac{1-\eta}{1-2/3} \right] + r_0 \left[\frac{\eta-2/3}{1-2/3} \right] & \text{if } \eta \in [2/3, 1] \end{cases}$$

and $X(\xi), Y(\xi), w(\xi)$ are the same as those in (4.3) and (4.4).

Table 4.1: Control points $\mathbf{B}_{i,j}$ and weights $w_{i,j}$. μ is a fixed real number with $0.5 \leq \mu \leq 0.9$.

	$1 \leq j \leq p_\eta$		$j = p_\eta + 1 (0.5 \leq \mu \leq 0.9)$		$j = p_\eta + 2$	
i	$\mathbf{B}_{i,j}$	$w_{i,j}$	$\mathbf{B}_{i,j}$	$w_{i,j}$	$\mathbf{B}_{i,j}$	$w_{i,j}$
1	(0, 0)	1	(0, $-\mu r_0$)	1	(0, $-r_0$)	1
2	(0, 0)	$\frac{1}{\sqrt{2}}$	($-\mu r_0, -\mu r_0$)	$\frac{1}{\sqrt{2}}$	($-r_0, -r_0$)	$\frac{1}{\sqrt{2}}$
3	(0, 0)	1	($-\mu r_0, 0$)	1	($-r_0, 0$)	1
4	(0, 0)	$\frac{1}{\sqrt{2}}$	($-\mu r_0, \mu r_0$)	$\frac{1}{\sqrt{2}}$	($-r_0, r_0$)	$\frac{1}{\sqrt{2}}$
5	(0, 0)	1	(0, μr_0)	1	(0, r_0)	1
6	(0, 0)	$\frac{1}{\sqrt{2}}$	($\mu r_0, \mu r_0$)	$\frac{1}{\sqrt{2}}$	(r_0, r_0)	$\frac{1}{\sqrt{2}}$
7	(0, 0)	1	($\mu r_0, 0$)	1	($r_0, 0$)	1

In addition to NURBS basis functions constructed through the design mapping, we are going to enrich it with singular approximation functions constructed through the singular mapping \mathbf{F}_0 , constructed in Step 2. From now on, the geometric mapping \mathbf{F}_0 is fixed and so does p_η used for the construction of \mathbf{F}_0 .

Step 3. Selecting B-spline functions that are compatible with NURBS functions:

Consider the B-spline functions corresponding to the open knot vector

$$\Xi_\eta = \{\underbrace{0, \dots, 0}_{p+1}, \underbrace{\eta_1, \dots, \eta_1}_p, \underbrace{1, \dots, 1}_{p+1}\}, \quad \eta_1 = 2/3, \mu = 0.8. \quad (4.5)$$

It is important to note that the p in (4.5) is different from the degree p_η in Table 4.1 that is fixed throughout computation. In other words, the p is the degree of

basis functions for approximations, whereas the p_η represents the degree of B-spline functions to be used for the construction of the NURBS geometrical mapping $\mathbf{F}_0 : [0, 1] \times [0, 1] \longrightarrow \Omega_0$.

Now, in order to make the enriched functions compatible with NURBS basis function constructed through the design mapping \mathbf{G} and to minimize the number of enriched functions, we remove the B-spline functions whose supports are $[\eta_1, 1]$ among the B-spline functions corresponding to the knot vector Ξ_η . Then the remaining B-spline functions are

$$M_j(\eta) = \binom{p}{j-1} g_1(\eta)^{j-1} (1 - g_1(\eta))^{p-j+1} \text{ for } j = 1, \dots, p,$$

$$M_{p+1}(\eta) = \begin{cases} g_1(\eta)^p & \text{if } \eta \in [0, 2/3] \\ (1 - g_2(\eta))^p & \text{if } \eta \in [2/3, 1] \end{cases}$$

where g_1 and g_2 are the scaling mappings defined by

$$g_1(\eta) = (3/2)\eta : [0, 2/3] \longrightarrow [0, 1]; \quad g_2(\eta) = 3(\eta - 2/3) : [2/3, 1] \longrightarrow [0, 1].$$

Let $\hat{\mathcal{S}}_\xi^h$ be the set of B-spline functions corresponding to the open knot vector $\Xi_\xi = \{0, 0, 0, 1/3, 1/3, 2/3, 2/3, 1, 1, 1\}$ or the h -refinement or the p -extension of these functions. Then, for all $\psi = N_i(\xi)M_j(\eta)$, $1 \leq j \leq p+1$, $N_i(\xi) \in \hat{\mathcal{S}}_\xi^h$, we have

$$\psi \circ \mathbf{F}_0^{-1} = 0, \text{ (compatibility condition)}$$

along the internal boundary $[\partial\Omega_0 \setminus \partial\Omega]$ of a disk neighborhood Ω_0 of the singularity point.

Step 4. Calculation of Stiffness matrix:

Suppose $\hat{\mathcal{S}}_{F_0}^h = \text{span}\{N_i(\xi) \times M_j(\eta) : N_i(\xi) \in \hat{\mathcal{S}}_\xi^h, j = 1, \dots, p+1\}$ is an approximation space of B-spline basis functions on $\hat{\Omega}_0 = [0, 1] \times [0, 1]$ in the (ξ, η) -coordinate sys-

tem, that is the parameter space of the singular mapping \mathbf{F}_0 for enrichment. Suppose $\hat{\mathcal{S}}_G^h$ is an approximation space spanned by NURBS basis functions on $\hat{\Omega}_G = [0, 1] \times [0, 1]$ in the $(\bar{\xi}, \bar{\eta})$ -coordinate system that denotes the parameter space of the design mapping \mathbf{G} .

Then our approximation space enriched around a singularity P_0 by $\hat{\mathcal{S}}_F^h$ is the span of $\hat{\mathcal{S}}_G^h \cup \hat{\mathcal{S}}_{F_0}^h$. Thus, we have to consider the following three cases:

- (Bilinear form for two rational NURBS functions)

If $R_{i,j}, R_{s,t} \in \mathcal{S}_G^h$, and $u = R_{i,j} \circ \mathbf{G}^{-1}, v = R_{s,t} \circ \mathbf{G}^{-1}$, then

$$\begin{aligned} \mathcal{B}(u, v) &= \int_{\Omega} (\nabla_x v)^T \cdot (\nabla_x u) dx dy \\ &= \int_{\hat{\Omega}_G} (\nabla_{\bar{\xi}} R_{s,t})^T \cdot [(J(\mathbf{G})^{-1})^T \cdot J(\mathbf{G})^{-1} |J(\mathbf{G})|] \\ &\quad (\nabla_{\bar{\xi}} R_{i,j}) d\bar{\xi} \bar{\eta}, \end{aligned} \quad (4.6)$$

where $\hat{\Omega}_G = \text{supp}(R_{i,j}) \cap \text{supp}(R_{s,t})$.

- (Bilinear form for two non-rational B-spline functions)

If $B_{i,j}, B_{s,t} \in \hat{\mathcal{S}}_F^h$, and $u = B_{i,j} \circ \mathbf{F}_0^{-1}, v = B_{s,t} \circ \mathbf{F}_0^{-1}$, then

$$\begin{aligned} \mathcal{B}(u, v) &= \int_{\Omega} (\nabla_x v)^T \cdot (\nabla_x u) dx dy \\ &= \int_{\hat{\Omega}_{F_0}} (\nabla_{\xi} B_{s,t})^T \cdot [(J(\mathbf{F}_0)^{-1})^T \cdot J(\mathbf{F}_0)^{-1} |J(\mathbf{F}_0)|] \\ &\quad (\nabla_{\xi} B_{i,j}) d\xi d\eta, \end{aligned} \quad (4.7)$$

where $\hat{\Omega}_{F_0} = \text{supp}(B_{i,j}) \cap \text{supp}(B_{s,t})$.

- (Bilinear form for mixed functions: NURBS function and B-spline function) If

$R_{i,j} \in \hat{\mathcal{S}}_G^h, B_{s,t} \in \hat{\mathcal{S}}_F^h$, and $u = R_{i,j} \circ \mathbf{G}^{-1}, v = B_{s,t} \circ \mathbf{F}_0^{-1}$, then

$$\begin{aligned}
\mathcal{B}(u, v) &= \int_{\Omega} (\nabla_x(B_{s,t} \circ \mathbf{F}_0^{-1}))^T \cdot (\nabla_x(R_{i,j} \circ \mathbf{G}^{-1})) dx dy \\
&= \int_{\Omega} (\nabla_x(B_{s,t} \circ \mathbf{F}_0^{-1}))^T \cdot (\nabla_x(R_{i,j} \circ \mathbf{G}^{-1})) \circ \mathbf{G} \circ \mathbf{G}^{-1} dx dy \\
&= \int_{\Omega} (\nabla_x(B_{s,t} \circ \mathbf{F}_0^{-1}))^T \cdot (J(\mathbf{G})^{-1} \cdot \nabla_{\bar{\xi}} R_{i,j}) \circ \mathbf{G}^{-1} dx dy \\
&= \int_{\hat{\Omega}_F} (\nabla_{\xi} B_{s,t})^T \cdot [(J(\mathbf{F}_0)^{-1})^T] \cdot [J(\mathbf{G})^{-1} \circ (\mathbf{G}^{-1} \circ \mathbf{F}_0)] \\
&\quad \cdot [\nabla_{\bar{\xi}} (R_{i,j}) \circ (\mathbf{G}^{-1} \circ \mathbf{F}_0)] |J(\mathbf{F}_0)| d\xi d\eta, \quad (4.8)
\end{aligned}$$

where $\hat{\Omega}_F = \text{supp}(B_{s,t}) \cap \mathbf{F}_0^{-1}(G(\text{supp}(R_{i,j})))$.

Step 5: Gaussian quadrature on the intersection of domains, $\Omega_{mix} = \Omega_0 \cap \text{supp}(B_{st}) \cap \text{supp}(R_{ij})$ of mixed types:

The domain $\mathbf{F}_0^{-1}(\Omega_{mix}) = \hat{\Omega}_F = \text{supp}(B_{s,t}) \cap \mathbf{F}_0^{-1}(G(\text{supp}(R_{i,j})))$ for the integral of functions of mixed type is non-polygonal subset of $\text{supp}(B_{s,t})$. Thus, it is not possible to apply the gaussian quadrature rule in a standard manner.

For all numerical examples presented in this section, we use the following simple procedure in applying quadrature rules:

- I. Divide $\text{supp}(B_{s,t})$ into nine rectangles (or 16 rectangles).
- II. Gaussian quadrature rule is applied on each of nine rectangular subregions of $\text{supp}(B_{s,t})$ as follows: for each gauss point (ξ, η) ,
 - (a) if $\mathbf{G}^{-1} \circ \mathbf{F}_0(\xi, \eta) \in \text{supp}(R_{i,j})$, choose it as an active gauss point.
 - (b) if $\mathbf{G}^{-1} \circ \mathbf{F}_0(\xi, \eta) \notin \text{supp}(R_{i,j})$, discard (ξ, η) and it is a inactive one.
- III. We use ten Gauss points in each variable (total number of gauss points ≤ 900) because integrands are rational functions and piecewise polynomials of high order.

Numerical results in the subsequent sections show that we do not waste gauss points in computing entries of the stiffness matrix.

In the enrichment approach, we joined two different sets of approximation functions: non-polynomial NURBS functions related to the design mapping \mathbf{G} and polynomial B-spline functions corresponding to the singular mapping \mathbf{F} , together. Since a linear combination of polynomial functions can not become a rational function, the mixed approximation functions used in the enrichment approach are linearly independent. Thus, we expect that the condition numbers of stiffness matrices for un-enriched IGA and enriched IGA are not much different as shown in Fig. 4.5, in which the changes of condition numbers in the enrichment process are depicted.

In the following section, we test the proposed enrichment technique in IGA to various singularity problems.

4.2 Numerical tests

In order to show that the proposed enrichment methods are effective for IGA of singularity problems, we test the enrichment method to the elliptic boundary value problems with singularity of type

$$r^\lambda \psi(\theta), \text{ where } 0 < \lambda < 1, \text{ and } \psi \text{ is a smooth function.}$$

For example, the crack singularity and the jump-boundary data singularity have $\lambda = 1/2$ and the interface problems and the elasticity problems with exotic boundary conditions could have λ , close to 0.

Throughout this section, we measure the error $(u - u^h)$ of the computed solutions obtained by the IGA enriched by our mapping method in the following norms: The relative error in L_∞ -norm in percent, the relative error in L_2 -norm in percent, respectively, defined by (2.17) and the relative error in energy norm in percent defined by

(2.15)

For the construction of NURBS and related k -refinement, one can use existing softwares and toolboxes such as GeopDEs, NURBS Toolbox in MATLAB, and so on. However, we used our own codes written by modifying the pseudo codes in [58] for the numerical results in this section. In order to demonstrate that the proposed mapping method for enrichment is more effective than the geometric mesh refinements, we compare the results obtained by applying the 5-radical mesh to each examples in this section. The 5-radical mesh technique is an application of geometric mesh refinement to IGA in order to deal with singularity problems (refer to [66] for details).

4.2.1 The Motz problem

Our first test problem is the Motz problem ([1, 43, 50] and references within) that is a well known benchmark problem which contains a jump boundary data singularity of type $\mathcal{O}(r^{1/2})$ at the origin $(0, 0)$.

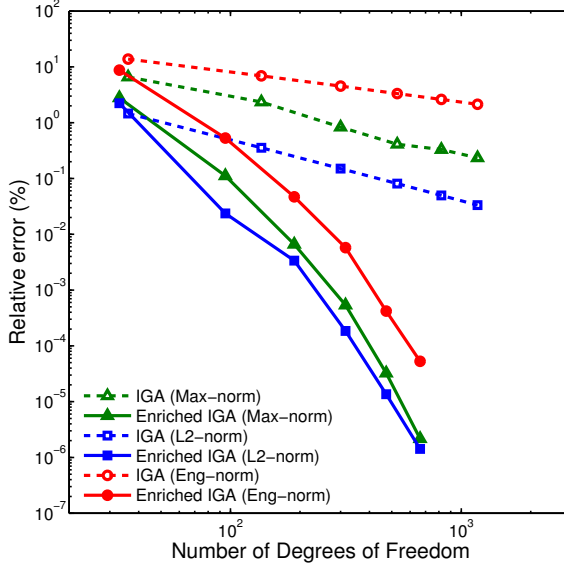
Example 4.2.1. *Let $\Omega = [-1, 1] \times [0, 1]$. Consider the following Laplace's equation with mixed boundary conditions:*

$$\begin{aligned} -\Delta u &= 0 && \text{in } \Omega, \\ u &= 500 && \text{on } \Gamma_2, \\ u &= 0 && \text{on } \Gamma_5, \\ \nabla u \cdot \mathbf{n} &= 0 && \text{on } \Gamma_1 \cup \Gamma_3 \cup \Gamma_4, \end{aligned}$$

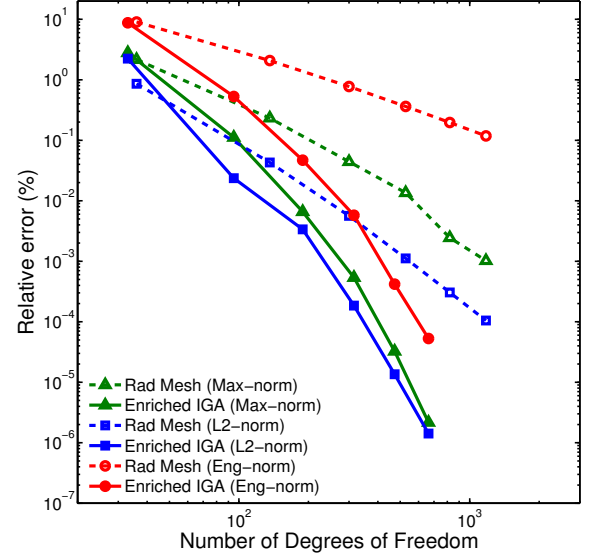
where $\Gamma_1 = [0, 1] \times \{0\}$, $\Gamma_2 = \{1\} \times [0, 1]$, $\Gamma_3 = [-1, 1] \times \{1\}$, $\Gamma_4 = \{-1\} \times [0, 1]$, and $\Gamma_5 = [-1, 0] \times \{0\}$, as shown in Fig. 4.7.

In this test, we assume the following:

1. The true solution of the Motz problem can be expressed asymptotically as



(a) *Rel errors (%) of enriched IGA (solid lines), IGA with no enrichment (dotted lines)*



(b) *Rel errors (%) of enriched IGA (solid lines), IGA with 5-radical mesh (dotted lines)*

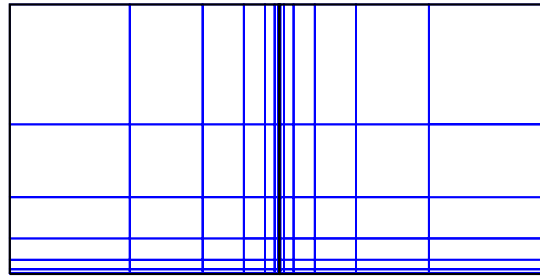
Figure 4.3: Relative errors (%) of the Motz problem in L_∞ , L_2 , and energy norms: (a) Enriched IGA (solid lines) and un-enriched IGA (dotted lines); (b) Enriched IGA (solid lines) and IGA with 5-radical mesh (dotted lines).

follow:

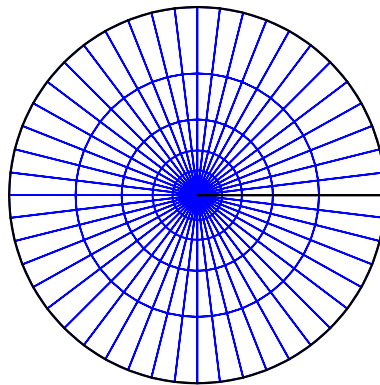
$$u(r, \theta) = \sum_{k=0}^{\infty} A_k r^{(1/2+k)} \cos((1/2+k)\theta). \quad (4.9)$$

Oh et al. [50] introduced a benchmarking numerical solution of this problem by accurately estimating the first 50 coefficients of the asymptotic solution (4.9). We use this computed solution (the partial sum of the first 50 terms of (4.9)) as the true solution of the Motz problem for estimations of the errors of the computed solutions.

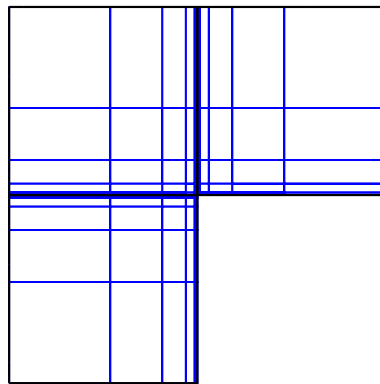
2. The control points and the coarse mesh on the physical domain are illustrated in Fig. 4.6. For the design mapping for the Motz problem, two square patches are put together for the physical domain. Each square patch has uniform mesh for un-enriched IGA and NURBS basis function corresponding to the open knot vector with only one knot insertion in both variables. In other words, for un-



(a) *Motz problem*



(b) *Unit circle*



(c) *L-shaped domain*

Figure 4.4: (a) The 5-radical mesh for the Motz problem, (b) The 5-radical mesh for the Laplace equation in the cracked unit disk and (c) The 5-radical mesh for the Laplace equation in the L -shaped domain.

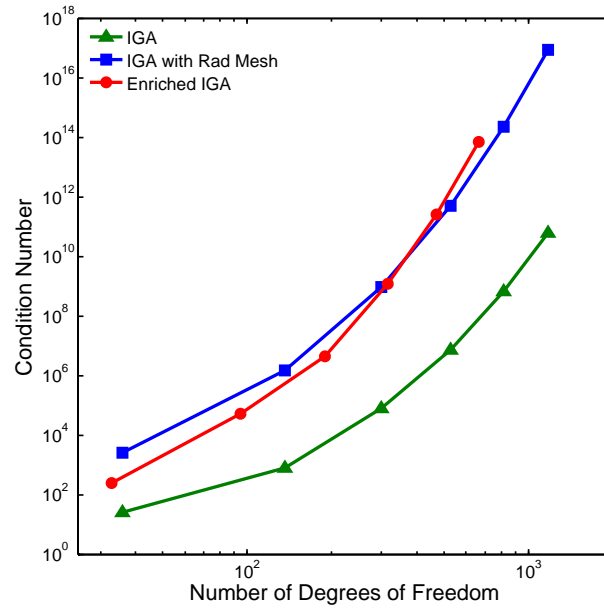


Figure 4.5: Condition numbers of constrained Stiffness matrices for IGA, enriched IGA, and IGA with radical mesh, respectively.

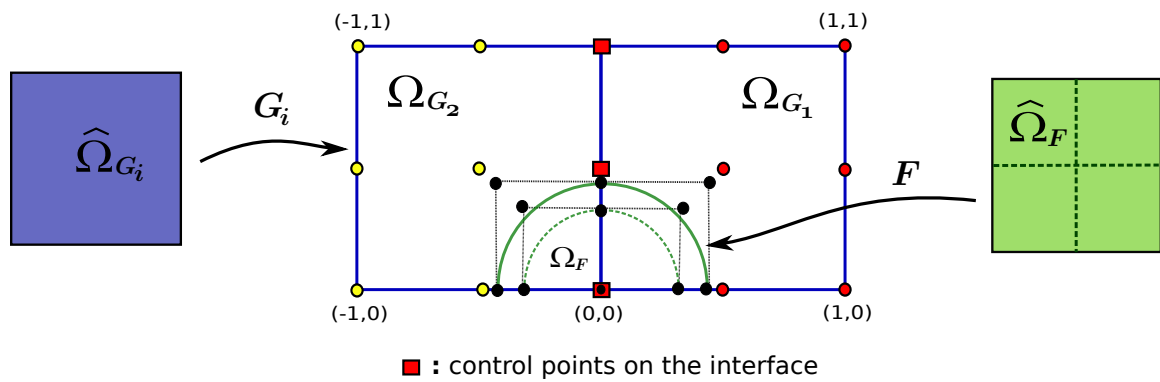


Figure 4.6: Diagram of the Enriched area for Motz problem and control points.

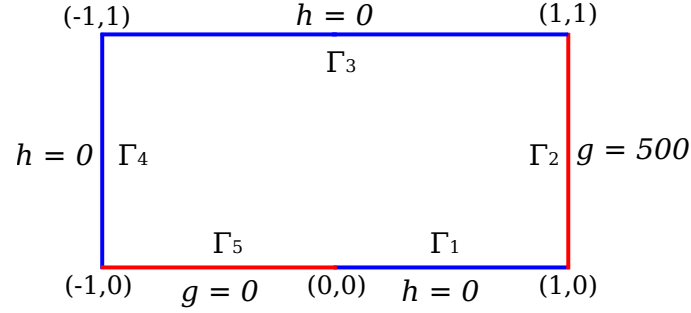


Figure 4.7: The domain of the Motz problem and boundary conditions. Here $g = u$ and $h = \frac{\partial u}{\partial n}$.

enriched IGA for the Motz problem, we use the k -refinement by inserting only one knot into the open knot vector to be $\{0, \dots, 0, 0.5, 1, \dots, 1\}$.

3. The enrichment functions are the B-spline functions of the polynomial degree $p_\xi = p_\eta$ in both variables corresponding to the open knot vectors

$$\{0, \dots, 0, 0.5, \dots, 0.5, 1, \dots, 1\}$$

$\underbrace{\hspace{1.5cm}}_{p_\eta+1} \quad \underbrace{\hspace{1.5cm}}_{p_\eta} \quad \underbrace{\hspace{1.5cm}}_{p_\eta+1}$

and

$$\{0, \dots, 0, 0.5, \dots, 0.5, 1, \dots, 1\}$$

$\underbrace{\hspace{1.5cm}}_{p_\xi+1} \quad \underbrace{\hspace{1.5cm}}_{p_\xi} \quad \underbrace{\hspace{1.5cm}}_{p_\xi+1}$

4. Condition numbers in Fig. 4.5 are calculated by the MATLAB functions from the constrained stiffness matrices.

The relative errors (%) and computed strain energy are shown in Table A.1 for the proposed enrichment approach and in Table A.3 for the 5-radical mesh approach [66] in Appendix. The relative errors (%) of enriched IGA and the relative errors of IGA with 5-radical mesh are plotted in Fig. 4.3, which shows the proposed enrichment method yields superior results over the radical mesh approach. The grid for the 5-radical mesh is shown in Fig. 4.4.

We observe that the proposed enrichment approach yields as accurate solutions

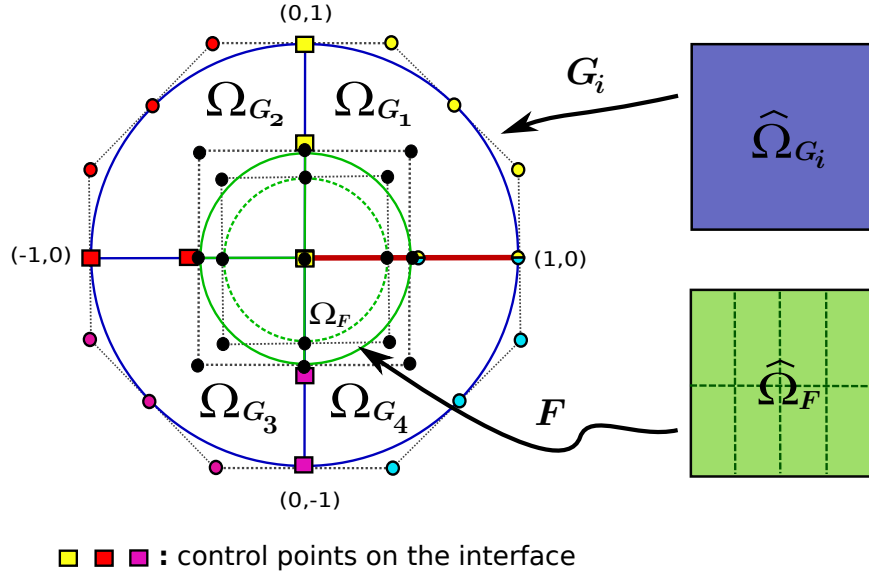


Figure 4.8: Diagram of the Enriched area for the cracked unit disk and control points.

as MAM shown in [43, 50] at lower DOF.

Next, we apply the proposed method to a problem containing singularity of type $r^{1/2}$ in the cracked unit disk:

4.2.2 The cracked unit disk

Example 4.2.2. (*The Laplace equation in the cracked unit disk*) Consider the Laplace equation $\Delta u = 0$ in the unit disk $\Omega = [0, 1] \times [0, 2\pi]$ in the polar coordinate as shown in Fig. 4.8 with Dirichlet boundary conditions: $u(r, \theta) = r^{1/2} \sin \theta / 2$ along $\partial\Omega = \{1\} \times [0, 2\pi] \cup [0, 1] \times \{0, 2\pi\}$.

We compare the performance of IGA with k -refinement, enriched IGA, IGA with radical mesh refinement in Figs. 4.9 and Tables A.4, A.6, and A.5 of Appendix. Here, “enriched IGA” means the relative errors of numerical solutions obtained by enriched IGA with k -refinement, and “IGA with radical meshes” represents the relative errors of numerical solutions obtained by using NURBS with 5-radical mesh [66]. For the details of the 5-radical mesh shown in Fig. 4.4, we refer to [66].

From these figures and Tables, we observe the following:

1. The control points and the coarse mesh on the physical domain are illustrated in Fig. 4.8. For the design mapping of the Laplace equation in the cracked unit disk, four quarter patches are put together for the physical domain. NURBS basis function corresponding to the open knot vector with only one knot insertion is applied in both variables. In other words, for un-enriched IGA for the the Laplace equation in the cracked unit disk, we use the k -refinement by inserting only one knot into the open knot vector to be $\{0, \dots, 0, 0.5, 1, \dots, 1\}$. Here, the suffix p_{nurbs} stands for the degree of NURBS.

2. The enrichment functions are the B-spline functions of the polynomial degree $p_\xi = p_\eta$ in both variables corresponding to the open knot vectors

$$\{0, \dots, 0, 0.5, \dots, 0.5, 1, \dots, 1\}$$

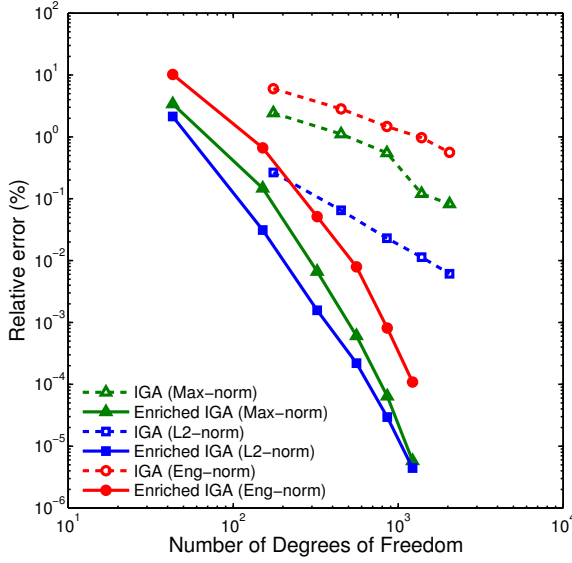
$\underbrace{\hspace{1.5cm}}_{p_\eta+1} \quad \underbrace{\hspace{1.5cm}}_{p_\eta} \quad \underbrace{\hspace{1.5cm}}_{p_\eta+1}$

and

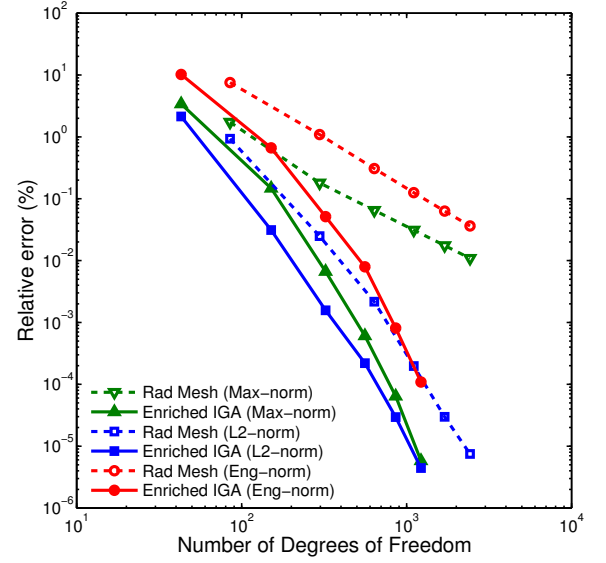
$$\{0, \dots, 0, 0.25, \dots, 0.25, 0.5, \dots, 0.5, 0.75, \dots, 0.75, 1, \dots, 1\}.$$

$\underbrace{\hspace{1.5cm}}_{p_\xi+1} \quad \underbrace{\hspace{1.5cm}}_{p_\xi} \quad \underbrace{\hspace{1.5cm}}_{p_\xi} \quad \underbrace{\hspace{1.5cm}}_{p_\xi} \quad \underbrace{\hspace{1.5cm}}_{p_\xi+1}$

3. Fig. 4.9(a) and Table A.5 show that the h - p , and k - refinement in IGA do not yield accurate approximations to the problem with the singularity of type $r^{1/2}$ at lower degrees of freedom.
4. Even though IGA with radical mesh yield good numerical solutions, Fig. 4.9(b) and Tables A.4 and A.6 show the enriched IGA yields far better results than IGA with 5-radical mesh which is known as an optimal one of the geometrical refinement approaches.
5. As it was shown in Figs. 4.8 and 4.4(b), the cracked unit disk is drawn by combining four one-quarter circular patches when enriched IGA is applied to the problem, whereas the cracked unit disk is designed with one patch when



(a) *Rel errors (%) of enriched IGA (solid lines), IGA without enrichment (dotted lines)*



(b) *Rel errors (%) of enriched IGA (solid lines), IGA with 5-radical mesh (dotted lines)*

Figure 4.9: Relative errors (%) of the computed solutions of the Laplace equation in the cracked unit disk in L_∞ , L_2 , and energy norms: (a) Enriched IGA (solid lines) and un-enriched IGA (dotted lines); (b) Enriched IGA (solid lines) and IGA with 5-radical mesh [66] (dotted lines).

either genuine IGA or IGA with radical mesh is applied.

- The Diagram for enriched IGA is depicted in Fig. 4.8, in which the cracked unit disk is designed by joining four one-quarter circular patches together.

Next, we apply the proposed enrichment approach to a Laplace equation containing corner singularities:

4.2.3 The L -shaped domain

Example 4.2.3. (*The Laplace equation in the L -shaped domain*) Consider the Laplace equation $\Delta u = 0$ in the L -shaped domain $\Omega = [-1, 1] \times [0, 1] \cup [-1, 0] \times [-1, 0]$ as shown in Fig. 4.10 with Dirichlet boundary conditions: $u(r, \theta) = r^{3/2} \sin 3\theta/2$ along $\partial\Omega$.

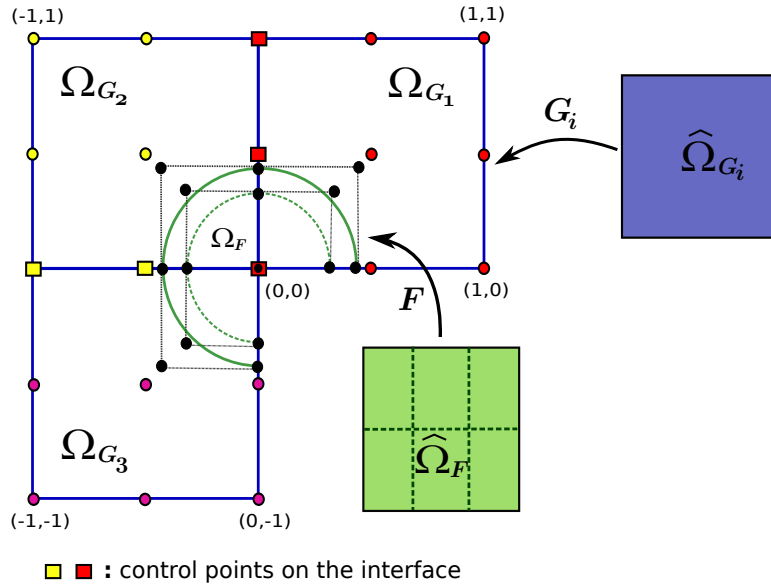


Figure 4.10: Diagram of the Enriched area for the L -shaped domain and control points

In similar to the Example 4.2.2, we compare the performance of IGA with h -refinement, enriched IGA, IGA with radical mesh refinement in Figs. 4.11 and Tables A.7, A.9, A.8 of Appendix.

From these figures and Tables, we observe the following:

1. Fig. 4.11(a) and Table A.8 show that the h - p , and k - refinement in IGA do not yield accurate approximations to the problem with corner singularity at lower degrees of freedom.
2. IGA with radical mesh yields more accurate numerical solutions than IGA without radical mesh in Fig. 4.11(a). However Fig. 4.11(b) and Tables A.7 and A.9 show the enriched IGA yields better results than IGA with 5-radical mesh [66] at lower DOF.
3. As it was shown in Fig. 4.10, the L -shaped domain is drawn by combining three square patches. Three patches construction is for IGA as well as IGA with radical mesh.

4. The Diagram for enriched IGA is depicted in Fig. 4.10, in which the L -shaped domain is designed by joining three square patches together.

4.3 Blending NURBS and B-splines through Partition of Unity (PU) with flat-top

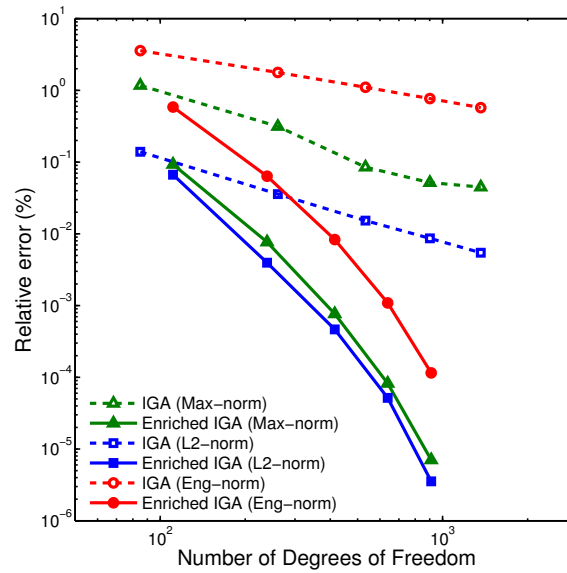
In Section 4.1, we discussed how to enrich NURBS basis functions generated from genuine IGA, with singular functions using the proposed mapping method in [30] and saw some examples in Section 4.2.1. In this section, we consider IGA combined with the proposed mapping techniques in [30] through PU functions with flat-top [53]. In order to deal with analysis of propagating cracks without altering original design mappings, we cut off NURBS basis functions, which are continuous along the cross faces, multiplying by PU functions with flat-top. Geometrically, it can be viewed that we cut out singular zones from a physical domain using PU functions with flat-top, paste back B-spline basis functions generated by the mapping method, that produce singular functions, into the singular zones. Due the supports of cut out PU and pasting back PU functions at non-void sets which are non flat-top ares, we have blending areas between NURBS and B-spline basis functions. To handle the blending regions, we newly design NURBS geometrical mapping that not only generates singular functions but also covers non flat-top belt areas of PU functions. Because of PU functions, we do not need to consider the compatibility condition in this blending of NURBS and B-splines.

4.3.1 Two dimensional Partition of Unity with flat-top

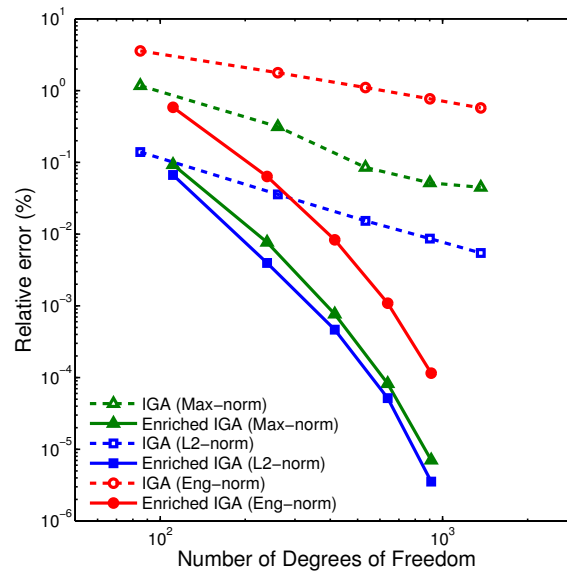
Let a and b real numbers with $0 < a < b \leq 1$ and

$$\delta_1 = \frac{b-a}{2}; \quad \delta_2 = \frac{a+b}{2}$$

We define a right step function by



(a) *Rel errors (%) of enriched IGA (solid lines), IGA without enrichment (dotted lines)*



(b) *Rel errors (%) of enriched IGA (solid lines), IGA with 5-radical mesh (dotted lines)*

Figure 4.11: Relative errors (%) of the computed solutions of the Laplace equation in the L -shaped domain in L_∞ , L_2 , and energy norms: (a) Enriched IGA (solid lines) and un-enriched IGA (dotted lines); (b) Enriched IGA (solid lines) and IGA with 5-radical mesh [66] (dotted lines)

$$\begin{aligned}
\psi_{(-\infty, b]}^R(x) &= \begin{cases} 1 & \text{if } x \in (-\infty, a], \\ \varphi_{g_n}^R\left(\frac{(x-\delta_2)+\delta_1}{2\delta_1}\right) & \text{if } x \in [a, b], \\ 0 & \text{if } x \in [b, \infty), \end{cases} \\
\psi_{[-b, \infty)}^L(x) &= \begin{cases} 0 & \text{if } x \in (-\infty, -b], \\ \varphi_{g_n}^L\left(\frac{(x+\delta_2)-\delta_1}{2\delta_1}\right) & \text{if } x \in [-b, -a], \\ 1 & \text{if } x \in [-a, \infty), \end{cases} \\
\psi_{[-b, b]}(x) &= \begin{cases} \varphi_{g_n}^L\left(\frac{(x+\delta_2)-\delta_1}{2\delta_1}\right) & \text{if } x \in [-b, -a], \\ 1 & \text{if } x \in [-a, a], \\ \varphi_{g_n}^R\left(\frac{(x-\delta_2)+\delta_1}{2\delta_1}\right) & \text{if } x \in [a, b], \\ 0 & \text{if } x \in (-\infty, -b] \cup [b, \infty), \end{cases}
\end{aligned}$$

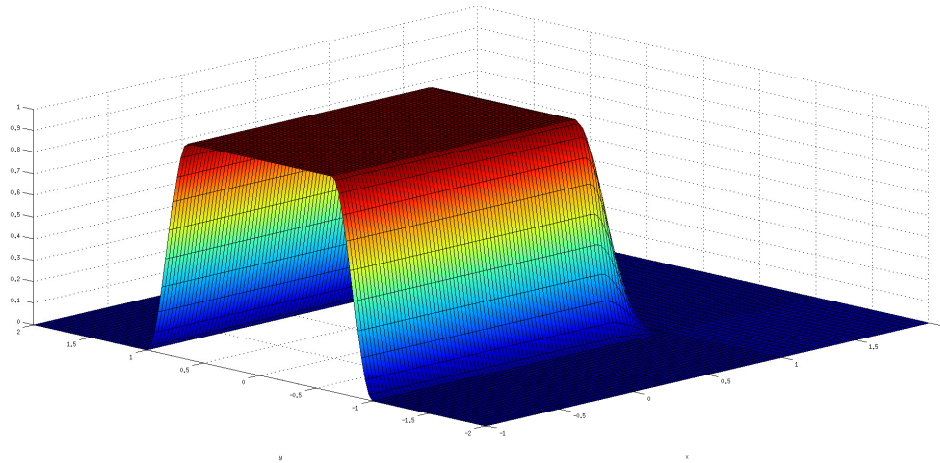
where $\varphi_{g_n}^R$ and $\varphi_{g_n}^L$ are \mathcal{C}^{n-1} -piecewise polynomial basic PU functions defined by (2.13). We then define two dimensional \mathcal{C}^{n-1} -partition of unity functions with flat-top as follows:

$$\hat{\Psi}^{out}(x, y) = 1 - \hat{\Psi}^{in}(x, y); \quad \hat{\Psi}^{in} = \psi_{(-\infty, b]}^R(x) \times \psi_{[-b, b]}(y), \text{ for all } (x, y) \in \mathbb{R}^2. \quad (4.10)$$

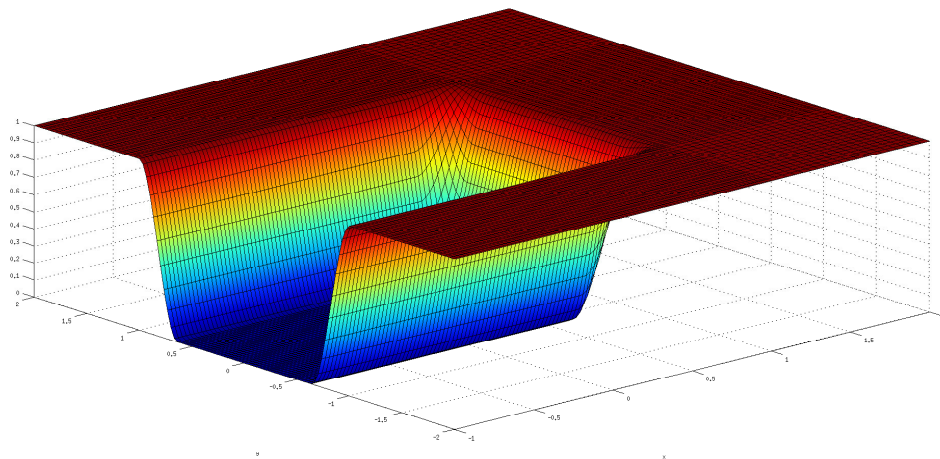
An examples of PU functions defined by Eq. (4.10) on the domain represented in Fig. 4.16 are shown in Fig. 4.12.

4.3.2 A design of a singular mapping that maps onto a neighborhood of a crack

In this subsection, we newly design a NURBS geometrical mapping $\mathbf{F}_1(\xi, \eta)$ that maps the parameter space into the support of $\hat{\Psi}^{in}$, and generates singular functions.



(a) An example of PU function $\hat{\Psi}^{in}$



(b) An example of PU function $\hat{\Psi}^{out}$

Figure 4.12: (a) An examples of PU functions with flat-top $\hat{\Psi}^{in}$ and (b) $\hat{\Psi}^{out}$ in the domain shown in Fig. 4.16 with $b = 1$

For the construction of this singular mapping, we assume the following:

1. Let

$$\begin{aligned}\hat{\Omega}_{\mathbf{F}_1} &= \hat{\Omega}_{\mathbf{G}} = [0, 1] \times [0, 1], \\ \Omega_{\mathbf{G}} &= \Omega = \mathbf{G}(\hat{\Omega}_{\mathbf{G}}) \\ \Omega_{\mathbf{F}_1} &= (-\infty, b] \times [-b, b] \cap \Omega_{\mathbf{G}} = \mathbf{F}_1(\hat{\Omega}_{\mathbf{F}_1})\end{aligned}$$

2. Let $\mathbf{F}_1 : \hat{\Omega}_{\mathbf{F}_1} \rightarrow \Omega_{\mathbf{F}_1}$ be a singular mapping corresponding to the knot vectors

$$\begin{aligned}\Xi_{\mathbf{F}_1, \xi} &= \{0, 0, 0, \frac{1}{8}, \frac{1}{8}, \frac{2}{8}, \frac{2}{8}, \frac{3}{8}, \frac{3}{8}, \frac{4}{8}, \frac{4}{8}, \frac{5}{8}, \frac{5}{8}, \frac{6}{8}, \frac{6}{8}, \frac{7}{8}, \frac{7}{8}, 1, 1, 1\} \text{ and} \\ \Xi_{\mathbf{F}_1, \eta} &= \{\underbrace{0, \dots, 0}_{p_{\eta+1}}, \underbrace{\eta_1, \dots, \eta_1}_{p_{\eta}}, \underbrace{\eta_2, \dots, \eta_2}_{p_{\eta}}, \underbrace{1, \dots, 1}_{p_{\eta+1}}\},\end{aligned}$$

where $0.5 \leq \eta_1 < \eta_2 < 1$.

3. Let $\mathbf{G} : \hat{\Omega}_{\mathbf{G}} \rightarrow \Omega_{\mathbf{G}}$ be a design mapping corresponding to the knot vectors $\Xi_{\mathbf{G}, \xi}$ and $\Xi_{\mathbf{G}, \eta}$.

4. Ω has a crack along the negative x -axis with crack tip at $(0, 0)$.

5. $\Omega_{\mathbf{F}_1} = Q_{\mathbf{F}_1}^{nft} \cup Q_{\mathbf{F}_1}^{ft}$, where $Q_{\mathbf{F}_1}^{nft}$ and $Q_{\mathbf{F}_1}^{ft}$ mean non flat-top area and flat-top area of the support $\hat{\Psi}^{in} = \psi_{(-\infty, b]}^R(x) \times \psi_{[-b, b]}(y)$, respectively. For example,

$$Q_{\mathbf{F}_1}^{nft} = \bigcup_{i=1}^5 Q_{\mathbf{F}_1, i}^{nft} \text{ as shown in Fig. 4.13.}$$

6. $\Omega_{\mathbf{G}} = \bigcup_{i=1}^{n_G} \omega_{\mathbf{G}, i}$, where $\omega_{\mathbf{G}, i} = \mathbf{G}(\hat{\omega}_{\mathbf{G}, i})$, and $\hat{\omega}_{\mathbf{G}, i}$'s are meshes corresponding to knot vectors $\Xi_{\mathbf{G}, \xi}$ and $\Xi_{\mathbf{G}, \eta}$.

7. $\partial\Omega_{\mathbf{G}} \cap \partial\Omega_{\mathbf{F}_1}$ is a straight line, and for each $k = 1, 2, \dots, 5$, $\mathbf{G}^{-1}(Q_{\mathbf{F}_1, k}^{nft}) = \hat{Q}_{\mathbf{G}, k}^{nft}$ is integral areas corresponding to non flat-top areas of PU functions $\hat{\Psi}^{in}$ and

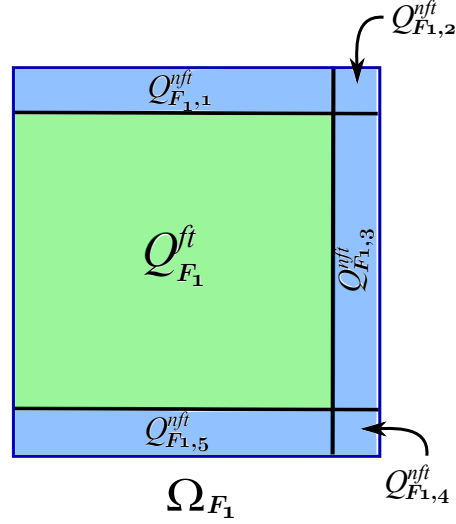


Figure 4.13: Integral areas of the PU function $\hat{\Psi}^{in}$ on the singular zone

$\hat{\Psi}^{out}$ on the parameter space $\hat{\Omega}_{\mathbf{G}}$. An example of $\hat{Q}_{\mathbf{G},k}^{nft}$ is shown in Fig. 4.14.

8. $\hat{\Omega}_{\mathbf{F}_1} = \bigcup_{i=1}^{n_F=24} \hat{\omega}_{\mathbf{F}_1,i}$, where $\hat{\omega}_{\mathbf{F}_1,i}$ are meshes corresponding to knot vectors $\Xi_{\mathbf{F}_1,\xi}$ and $\Xi_{\mathbf{F}_1,\eta}$. Then $\Omega_{\mathbf{F}_1} = \bigcup_{i=1}^{n_F} \omega_{\mathbf{F}_1,i}$, where $\omega_{\mathbf{F}_1,i} = \mathbf{F}_1(\hat{\omega}_{\mathbf{F}_1,i})$.

We use the control points and weights from Table C.3 in first two Bézier segments $[0, \eta_1]$ and $[\eta_1, \eta_2]$. Then our singular mapping $\mathbf{F}_1(\xi, \eta)$ generates singular functions of type $\mathcal{O}(r^{1/p_\eta})$. For the third Bézier segment, we choose control points and weights such that

$$\bigcup_{i=17}^{24} \omega_{\mathbf{F}_1,i} = Q_{\mathbf{F}_1}^{nft}$$

as shown in Fig. 4.15.

Once we design the singular mapping \mathbf{F}_1 that maps onto a neighborhood $\Omega_{\mathbf{F}_1}$ of a crack, we must consider intersection areas

$$\omega_{\mathbf{G},j} \cap Q_{\mathbf{F}_1,k}^{nft} \cap \omega_{\mathbf{F}_1,i},$$

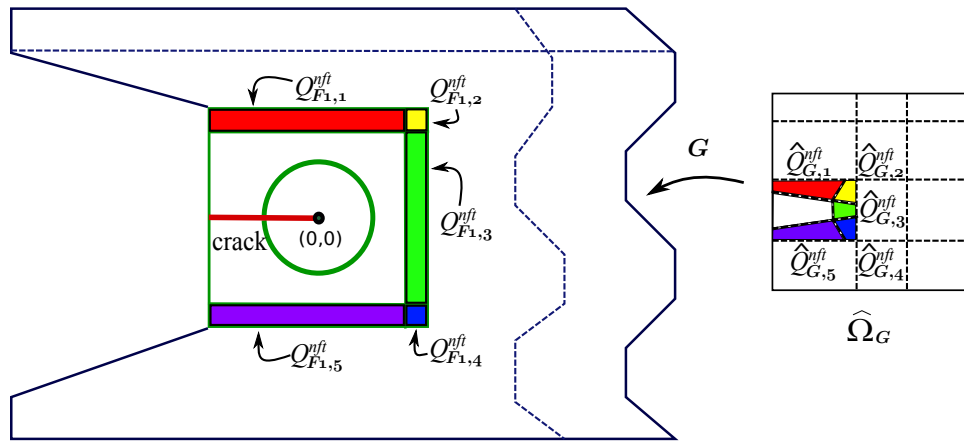


Figure 4.14: An example of $\hat{Q}_{G,k}^{nft}$ for given $Q_{F_1,k}^{nft}$, $k = 1, \dots, 5$

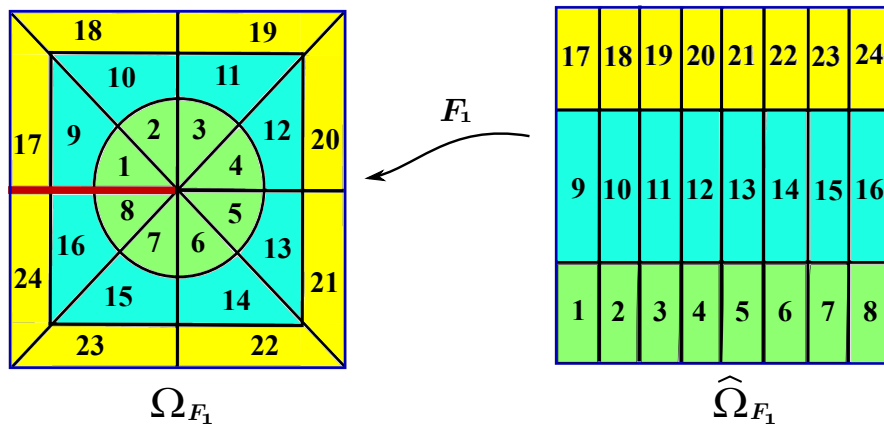


Figure 4.15: Integral areas of Ω_{F_1} and $\hat{\Omega}_{F_1}$

where $\omega_{\mathbf{G},j} = \mathbf{G}(\hat{\omega}_{\mathbf{G},j})$ and $\omega_{\mathbf{F}_1,i} = \mathbf{F}_1(\hat{\omega}_{\mathbf{F}_1,i})$, $i = 1, \dots, 24$, $j = 1, \dots, n_G$, $k = 1, \dots, 5$.

First, let us consider intersection areas $\omega_{\mathbf{F}_1,i} \cap Q_{\mathbf{F}_1,k}^{nft}$. Then we divide $\omega_{\mathbf{F}_1,i}$ into two areas, for each $i = 17, \dots, 24$ as shown in Fig. 4.17. Actually, we do not need to divide $\omega_{\mathbf{F}_1,18}$ and $\omega_{\mathbf{F}_1,23}$ into two areas because

$$\omega_{\mathbf{F}_1,18} \cap Q_{\mathbf{F}_1,1}^{nft} = \omega_{\mathbf{F}_1,18} \text{ and } \omega_{\mathbf{F}_1,23} \cap Q_{\mathbf{F}_1,5}^{nft} = \omega_{\mathbf{F}_1,23},$$

But we divide each of them into two for the convenience of coding.

Next, we divide integral areas $\hat{\omega}_{\mathbf{G},j}$ on the parameter space $\hat{\Omega}_{\mathbf{G}}$, to satisfy the following:

$$\exists J_k = \{j_{k,1}, \dots, j_{k,m_k}\} \subset \mathbb{N} \text{ such that } \bigcup_{j=j_{k,1}}^{j_{k,m_k}} \hat{\omega}_{\mathbf{G},j} = \hat{Q}_{\mathbf{G},k}^{nft}, \quad (4.11)$$

for each k , $k = 1, \dots, 5$,

Now, then,

$$\omega_{\mathbf{G},j} \cap Q_{\mathbf{F}_1,k}^{nft} \cap \omega_{\mathbf{F}_1,i} = \omega_{\mathbf{G},j} \cap \omega_{\mathbf{F}_1,i},$$

because for each i , $i = 1, \dots, 32$, $\exists k$ such that $\omega_{\mathbf{F}_1,i} \subseteq Q_{\mathbf{F}_1,k}^{nft}$.

If either

$$(\omega_{\mathbf{G},j} \cap \omega_{\mathbf{F}_1,i}) \subset \omega_{\mathbf{F}_1,i} \text{ or } (\omega_{\mathbf{G},j} \cap \omega_{\mathbf{F}_1,i}) \subset \omega_{\mathbf{G},j},$$

for $i = 1, \dots, 32$ and $j = 1, \dots, n_G$, then we employ the procedures (I), (II), and (III) in Section 4.1. Otherwise, we compute numerical integrations on

$$\text{either } \omega_{\mathbf{F}_1,i} \text{ or } \omega_{\mathbf{F}_1,i}^{\hat{}}, \text{ if } \omega_{\mathbf{G},j} \cap \omega_{\mathbf{F}_1,i} = \omega_{\mathbf{F}_1,i}, \text{ and} \quad (4.12)$$

$$\text{either } \omega_{\mathbf{G},i} \text{ or } \omega_{\mathbf{G},i}^{\hat{}}, \text{ if } \omega_{\mathbf{G},j} \cap \omega_{\mathbf{F}_1,i} = \omega_{\mathbf{G},i},$$

For PU functions $\hat{\Psi}^{in}$ and $\hat{\Psi}^{out}$, and two global basis functions, B-spline $B_{i,j}$ and NURBS $R_{s,t}$,

$$(B_{i,j} \circ \mathbf{F}_1^{-1}) \cdot \hat{\Psi}^{in} \text{ and } (R_{s,t} \circ \mathbf{G}^{-1}) \cdot \hat{\Psi}^{out},$$

become the mixed type approximation functions, whose supports have the non-void intersection on the strip with width $(b - a)$ along the inside boundary of $\Omega_{\mathbf{F}_1}$.

Calculation of stiffness matrix is also different from that of Step 4 in Section 4.1:

- (Bilinear form for two rational NURBS functions)

If $R_{i,j}, R_{s,t} \in \mathcal{S}_{\mathbf{G}}^h$, and $u = R_{i,j} \circ \mathbf{G}^{-1} \cdot \hat{\Psi}^{out}$, $v = R_{s,t} \circ \mathbf{G}^{-1} \cdot \hat{\Psi}^{out}$, then

$$\begin{aligned} \mathcal{B}(u, v) &= \int_{\Omega} (\nabla_x v)^T \cdot (\nabla_x u) dx dy \\ &= \int_{\Omega} [\nabla_x (R_{s,t} \circ \mathbf{G}^{-1}) \cdot \hat{\Psi}^{out} + R_{s,t} \circ \mathbf{G}^{-1} \cdot \nabla_x \hat{\Psi}^{out}]^T \cdot \\ &\quad [\nabla_x (R_{i,j} \circ \mathbf{G}^{-1}) \cdot \hat{\Psi}^{out} + R_{i,j} \circ \mathbf{G}^{-1} \cdot \nabla_x \hat{\Psi}^{out}] dx dy \\ &= \int_{\Omega} [\nabla_x (R_{s,t} \circ \mathbf{G}^{-1}) \cdot \hat{\Psi}^{out}]^T \cdot [\nabla_x (R_{i,j} \circ \mathbf{G}^{-1}) \cdot \hat{\Psi}^{out}] + \\ &\quad [\nabla_x (R_{s,t} \circ \mathbf{G}^{-1}) \cdot \hat{\Psi}^{out}]^T \cdot [R_{i,j} \circ \mathbf{G}^{-1} \cdot \nabla_x \hat{\Psi}^{out}] + \\ &\quad [R_{s,t} \circ \mathbf{G}^{-1} \cdot \nabla_x \hat{\Psi}^{out}]^T \cdot [\nabla_x (R_{i,j} \circ \mathbf{G}^{-1}) \cdot \hat{\Psi}^{out}] + \\ &\quad [R_{s,t} \circ \mathbf{G}^{-1} \cdot \nabla_x \hat{\Psi}^{out}]^T \cdot [R_{i,j} \circ \mathbf{G}^{-1} \cdot \nabla_x \hat{\Psi}^{out}] dx dy \\ &= \int_{\hat{\Omega}_{\mathbf{G}}^{supp}} \left([\nabla_{\bar{\xi}} R_{s,t} \cdot J(\mathbf{G})^{-1} \cdot \hat{\Psi}^{out} \circ \mathbf{G}]^T \cdot [\nabla_{\bar{\xi}} R_{i,j} \cdot J(\mathbf{G})^{-1} \cdot \hat{\Psi}^{out} \circ \mathbf{G}] + \right. \\ &\quad [\nabla_{\bar{\xi}} R_{s,t} \cdot J(\mathbf{G})^{-1} \cdot \hat{\Psi}^{out} \circ \mathbf{G}]^T \cdot [R_{i,j} \cdot \nabla_x \hat{\Psi}^{out} \circ \mathbf{G}] + \\ &\quad [R_{s,t} \cdot \nabla_x \hat{\Psi}^{out} \circ \mathbf{G}]^T \cdot [\nabla_{\bar{\xi}} R_{i,j} \cdot J(\mathbf{G})^{-1} \cdot \hat{\Psi}^{out} \circ \mathbf{G}] + \\ &\quad \left. [R_{s,t} \cdot \nabla_x \hat{\Psi}^{out} \circ \mathbf{G}]^T \cdot [R_{i,j} \cdot \nabla_x \hat{\Psi}^{out} \circ \mathbf{G}] \right) |J(\mathbf{G})| d\bar{\xi} d\bar{\eta} \quad (4.13) \end{aligned}$$

where $\hat{\Omega}_{\mathbf{G}}^{supp} = \text{supp}(R_{i,j}) \cap \text{supp}(R_{s,t})$.

- (Bilinear form for two non-rational B-spline functions)

If $B_{i,j}, B_{s,t} \in \hat{\mathcal{S}}_F^h$, and $u = B_{i,j} \circ \mathbf{F}_1^{-1} \cdot \hat{\Psi}^{in}, v = B_{s,t} \circ \mathbf{F}_1^{-1} \cdot \hat{\Psi}^{in}$, then

$$\begin{aligned}
\mathcal{B}(u, v) &= \int_{\Omega} (\nabla_x v)^T \cdot (\nabla_x u) dx dy \\
&= \int_{\Omega} [\nabla_x (B_{s,t} \circ \mathbf{F}_1^{-1}) \cdot \hat{\Psi}^{in} + B_{s,t} \circ \mathbf{F}_1^{-1} \cdot \nabla_x \hat{\Psi}^{in}]^T \cdot \\
&\quad [\nabla_x (B_{i,j} \circ \mathbf{F}_1^{-1}) \cdot \hat{\Psi}^{in} + B_{i,j} \circ \mathbf{F}_1^{-1} \cdot \nabla_x \hat{\Psi}^{in}] dx dy \\
&= \int_{\Omega} [\nabla_x (B_{s,t} \circ \mathbf{F}_1^{-1}) \cdot \hat{\Psi}^{in}]^T \cdot [\nabla_x (B_{i,j} \circ \mathbf{F}_1^{-1}) \cdot \hat{\Psi}^{in}] + \\
&\quad [\nabla_x (B_{s,t} \circ \mathbf{F}_1^{-1}) \cdot \hat{\Psi}^{in}]^T \cdot [B_{i,j} \circ \mathbf{F}_1^{-1} \cdot \nabla_x \hat{\Psi}^{in}] + \\
&\quad [B_{s,t} \circ \mathbf{F}_1^{-1} \cdot \nabla_x \hat{\Psi}^{in}]^T \cdot [\nabla_x (B_{i,j} \circ \mathbf{F}_1^{-1}) \cdot \hat{\Psi}^{in}] + \\
&\quad [B_{s,t} \circ \mathbf{F}_1^{-1} \cdot \nabla_x \hat{\Psi}^{in}]^T \cdot [B_{i,j} \circ \mathbf{F}_1^{-1} \cdot \nabla_x \hat{\Psi}^{in}] dx dy \\
&= \int_{\hat{\Omega}_{\mathbf{F}_1}^{supp}} \left([\nabla_{\xi} B_{s,t} \cdot J(\mathbf{F}_1)^{-1} \cdot \hat{\Psi}^{in} \circ \mathbf{F}_1]^T \cdot [\nabla_{\xi} B_{i,j} \cdot J(\mathbf{F}_1)^{-1} \cdot \hat{\Psi}^{in} \circ \mathbf{F}_1] + \right. \\
&\quad [\nabla_{\xi} B_{s,t} \cdot J(\mathbf{F}_1)^{-1} \cdot \hat{\Psi}^{in} \circ \mathbf{F}_1]^T \cdot [B_{i,j} \cdot \nabla_x \hat{\Psi}^{in} \circ \mathbf{F}_1] + \\
&\quad [B_{s,t} \cdot \nabla_x \hat{\Psi}^{in} \circ \mathbf{F}_1]^T \cdot [\nabla_{\xi} B_{i,j} \cdot J(\mathbf{F}_1)^{-1} \cdot \hat{\Psi}^{in} \circ \mathbf{F}_1] + \\
&\quad \left. [B_{s,t} \cdot \nabla_x \hat{\Psi}^{in} \circ \mathbf{F}_1]^T \cdot [B_{i,j} \cdot \nabla_x \hat{\Psi}^{in} \circ \mathbf{F}_1] \right) |J(\mathbf{F}_1)| d\xi d\eta \quad (4.14)
\end{aligned}$$

where $\hat{\Omega}_{\mathbf{F}_1}^{supp} = \text{supp}(B_{i,j}) \cap \text{supp}(B_{s,t})$.

- (Bilinear form for mixed functions: NURBS function and non-rational B-spline function) If $R_{i,j} \in \hat{\mathcal{S}}_G^h, B_{s,t} \in \hat{\mathcal{S}}_F^h, u = R_{i,j} \circ \mathbf{G}^{-1} \cdot \hat{\Psi}^{out}, v = B_{s,t} \circ \mathbf{F}_1^{-1} \cdot \hat{\Psi}^{in}$, and

$\omega_{\mathbf{G},l} \cap \omega_{\mathbf{F}_1,k} = \omega_{\mathbf{F}_1,k}$ then

$$\begin{aligned}
\mathcal{B}(u, v) &= \int_{\Omega} [\nabla_x(B_{s,t} \circ \mathbf{F}_1^{-1}) \cdot \hat{\Psi}^{in}]^T \cdot [\nabla_x(R_{i,j} \circ \mathbf{G}^{-1}) \cdot \hat{\Psi}^{out}] dx dy \\
&= \int_{\Omega} [\nabla_x(B_{s,t} \circ \mathbf{F}_1^{-1}) \cdot \hat{\Psi}^{in} + B_{s,t} \circ \mathbf{F}_1^{-1} \cdot \nabla_x \hat{\Psi}^{in}]^T \cdot \\
&\quad [\nabla_x(R_{i,j} \circ \mathbf{G}^{-1}) \cdot \hat{\Psi}^{out} + R_{i,j} \circ \mathbf{G}^{-1} \cdot \nabla_x \hat{\Psi}^{out}] dx dy \\
&= \int_{\Omega} [\nabla_x(B_{s,t} \circ \mathbf{F}_1^{-1}) \cdot \hat{\Psi}^{in}]^T \cdot [\nabla_x(R_{i,j} \circ \mathbf{G}^{-1}) \cdot \hat{\Psi}^{out}] + \\
&\quad [\nabla_x(B_{s,t} \circ \mathbf{F}_1^{-1}) \cdot \hat{\Psi}^{in}]^T \cdot [R_{i,j} \circ \mathbf{G}^{-1} \cdot \nabla_x \hat{\Psi}^{out}] + \\
&\quad [B_{s,t} \circ \mathbf{F}_1^{-1} \cdot \nabla_x \hat{\Psi}^{in}]^T \cdot [\nabla_x(R_{i,j} \circ \mathbf{G}^{-1}) \cdot \hat{\Psi}^{out}] + \\
&\quad [B_{s,t} \circ \mathbf{F}_1^{-1} \cdot \nabla_x \hat{\Psi}^{in}]^T \cdot [R_{i,j} \circ \mathbf{G}^{-1} \cdot \nabla_x \hat{\Psi}^{out}] dx dy \\
&= \int_{\Omega} [\nabla_x(B_{s,t} \circ \mathbf{F}_1^{-1}) \cdot \hat{\Psi}^{in}]^T \cdot [\nabla_x(R_{i,j} \circ \mathbf{G}^{-1}) \circ \mathbf{G} \circ \mathbf{G}^{-1} \cdot \hat{\Psi}^{out}] + \\
&\quad [\nabla_x(B_{s,t} \circ \mathbf{F}_1^{-1}) \cdot \hat{\Psi}^{in}]^T \cdot [R_{i,j} \circ \mathbf{G}^{-1} \cdot \nabla_x \hat{\Psi}^{out}] + \\
&\quad [B_{s,t} \circ \mathbf{F}_1^{-1} \cdot \nabla_x \hat{\Psi}^{in}]^T \cdot [\nabla_x(R_{i,j} \circ \mathbf{G}^{-1}) \circ \mathbf{G} \circ \mathbf{G}^{-1} \cdot \hat{\Psi}^{out}] + \\
&\quad [B_{s,t} \circ \mathbf{F}_1^{-1} \cdot \nabla_x \hat{\Psi}^{in}]^T \cdot [R_{i,j} \circ \mathbf{G}^{-1} \cdot \nabla_x \hat{\Psi}^{out}] dx dy \\
&= \int_{\hat{\Omega}_{\mathbf{F}_1}^{supp}} \left([\nabla_{\xi} B_{s,t} \cdot J(\mathbf{F}_1)^{-1} \cdot \hat{\Psi}^{in} \circ \mathbf{F}_1]^T \cdot \right. \\
&\quad [\nabla_{\bar{\xi}} R_{i,j} \circ (\mathbf{G}^{-1} \circ \mathbf{F}_1) \cdot J(\mathbf{G})^{-1} \circ (\mathbf{G}^{-1} \circ \mathbf{F}_1) \cdot \hat{\Psi}^{out} \circ \mathbf{F}_1] + \\
&\quad [\nabla_{\xi} B_{s,t} \cdot J(\mathbf{F}_1)^{-1} \cdot \hat{\Psi}^{in} \cdot \mathbf{F}_1]^T \cdot [R_{i,j} \circ (\mathbf{G}^{-1} \circ \mathbf{F}_1) \cdot \nabla_x \hat{\Psi}^{out} \circ \mathbf{F}_1] + \\
&\quad [B_{s,t} \cdot \nabla_x \hat{\Psi}^{in} \circ \mathbf{F}_1]^T \cdot [\nabla_{\bar{\xi}} R_{i,j} \circ (\mathbf{G}^{-1} \circ \mathbf{F}_1) \cdot J(\mathbf{G})^{-1} \circ \\
&\quad (\mathbf{G}^{-1} \circ \mathbf{F}_1) \cdot \hat{\Psi}^{out} \circ \mathbf{F}_1] + [B_{s,t} \cdot \nabla_x \hat{\Psi}^{in} \circ \mathbf{F}_1]^T \cdot \\
&\quad \left. [R_{i,j} \circ (\mathbf{G}^{-1} \circ \mathbf{F}_1) \cdot \nabla_x \hat{\Psi}^{out} \circ \mathbf{F}_1] \right) |J(\mathbf{F}_1)| d\xi d\eta \tag{4.15}
\end{aligned}$$

where $\hat{\Omega}_{\mathbf{F}_1}^{supp} = \text{supp}(B_{s,t}) \cap \mathbf{F}_1^{-1}(\mathbf{G}(\text{supp}(R_{i,j})))$.

4.3.3 Numerical test

We test the proceeding method to the following Laplace equation:

Example 4.3.1. *(The Laplace equation containing the crack singularity along neg-*

ative x -axis) Consider the Laplace equation $\Delta u = 0$ in the domain $\Omega_{\mathbf{G}} = [-1, 2] \times [-2, 2]$ with crack along the negative x -axis, as shown in Fig. 4.16 with Dirichlet boundary conditions: $u(r, \theta) = r^{1/2} \cos \theta / 2$ along $\partial\Omega_{\mathbf{G}}$.

From the Figs. 4.16 and 4.18 we observe the following:

1. We choose $\delta_1 = \delta_2 = 0.05$, i.e. the thickness of the non flat-top belt area of PU functions $\hat{\Psi}^{in}$ and $\hat{\Psi}^{out}$ is 0.1, and $\Omega_{\mathbf{F}_1} = (-\infty, -1] \times [-1, 1] \cap \Omega_{\mathbf{G}}$ which is a neighborhood of the crack.
2. Integral areas are originally divided into 24 rectangles on the parameter space of the singular mapping $\hat{\Omega}_{\mathbf{F}_1}$, and then we divide $\hat{\omega}_{\mathbf{F}_1, i}$, $i = 17, \dots, 24$ more to detect the intersection area with non flat-top area of PU functions so that we have 32 integral supports as shown Fig. 4.17.
3. Initially, integral areas of NURBS functions that are used to construct the design mapping \mathbf{G} , are divided to satisfy (4.11). Hence, $\Omega_{\mathbf{G}} = \bigcup_{j=1}^{15} \omega_{\mathbf{G}, j}$.
4. We insert one knot value with multiplicity 1 in $\Xi_{\mathbf{G}, \xi}$ and two knot values with multiplicity 1 in $\Xi_{\mathbf{G}, \eta}$ while performing k -refinement, to satisfy (4.13) as shown in Fig. 4.16.
5. We observe that the proposed combining method of enrichment through PU functions with flat-top yields accurate results in Fig. 4.18.

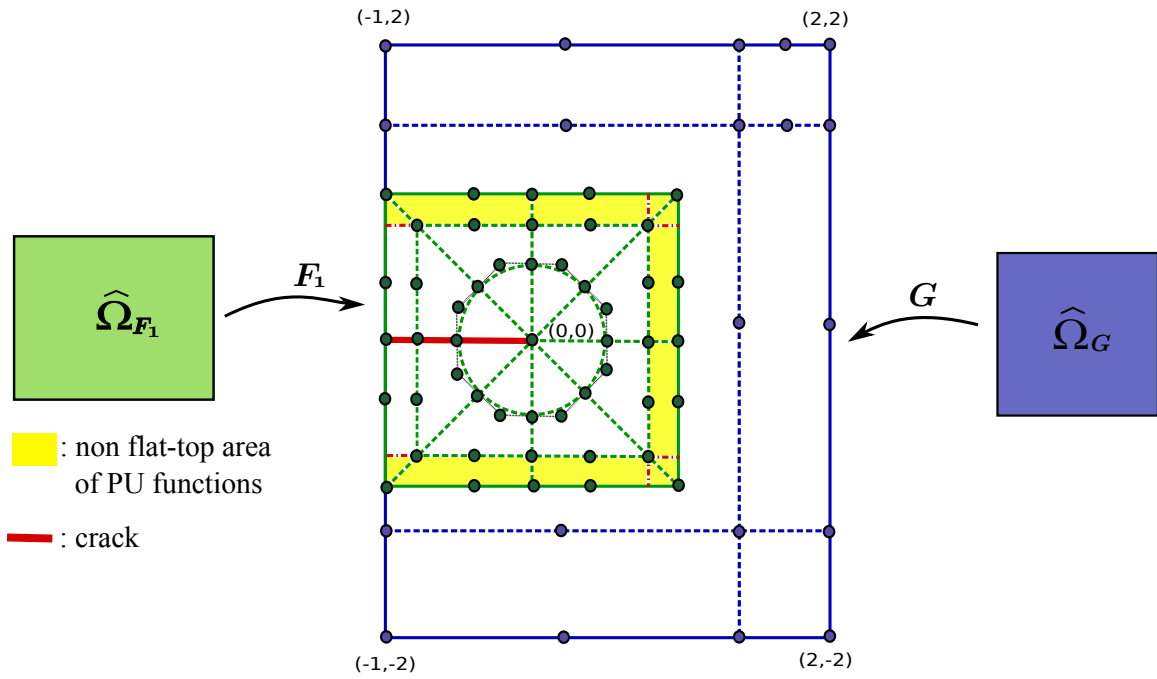


Figure 4.16: The physical domain and control points for each maps F_1 and G of Example 4.3.1.

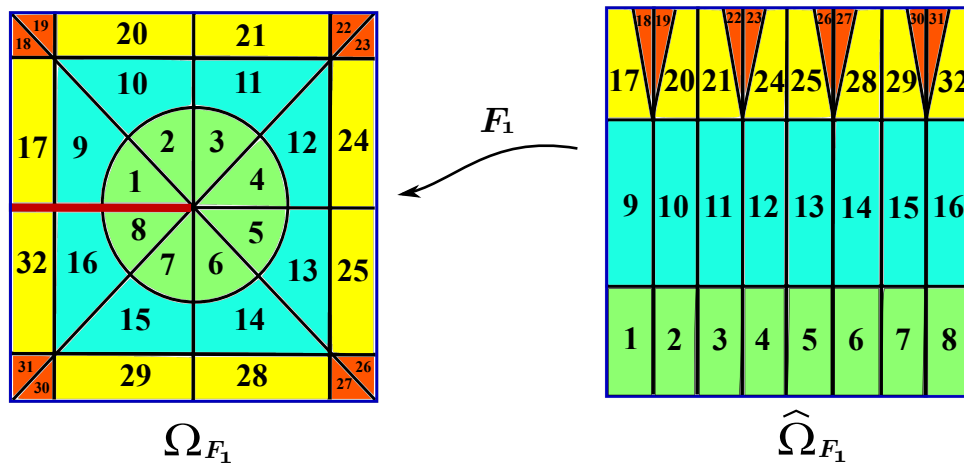


Figure 4.17: Integral areas on the parameter space $\hat{\Omega}_{F_1}$ of the newly designed singular mapping F_1 . Note that Ω_{F_1} corresponding to $\hat{\Omega}_{F_1}$ is the singular zone including non flat-top area of PU functions in the physical domain.

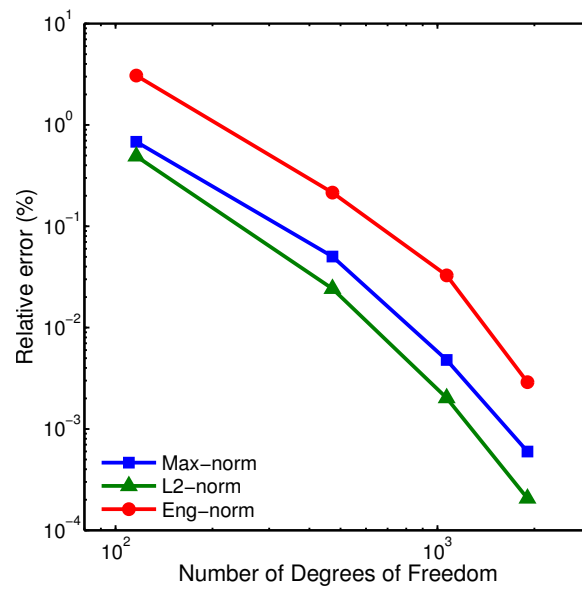


Figure 4.18: Relative errors (%) of the computed solutions of the Laplace equation in Example 4.3.1 in L_∞ , L_2 , and energy norm.

CHAPTER 5: PATCHWISE RPPM FOR THICK PLATES

5.1 Formulations for free vibration and buckling

5.1.1 Governing equations and variational formulation of Reissner-Mindlin plates

Following notations in the book [60], under the Kirchoff hypothesis but relaxing the normality condition, the displacement field of the first order theory can be expressed in the form

$$\begin{aligned}u(x, y, z, t) &= u_0(x, y, t) + z\phi_x(x, y, t), \\v(x, y, z, t) &= v_0(x, y, t) + z\phi_y(x, y, t), \\w(x, y, z, t) &= w_0(x, y, t).\end{aligned}\tag{5.1}$$

(u_0, v_0, w_0) denotes the displacements of a point on the plane $z = 0$ and ϕ_x and ϕ_y are the rotations of a transverse normal about the y - and x - axis as shown in Fig. 5.1, respectively

$$u_{,z} = \phi_x, \quad v_{,z} = \phi_y.\tag{5.2}$$

In the Reissner-Mindlin plate, bending and shear strains are only considered and they can be expressed in the vector form as

$$\{\varepsilon_b\} = \left\{ \begin{array}{c} \phi_{x,x} \\ \phi_{y,y} \\ \phi_{x,y} + \phi_{y,x} \end{array} \right\} \text{ and } \{\varepsilon_s\} = \left\{ \begin{array}{c} w_{0,y} + \phi_y \\ w_{0,x} + \phi_x \end{array} \right\}, \text{ respectively.}\tag{5.3}$$

The Euler-Lagrange equations of the Reissner-Mindlin plate can be derived by using the dynamic version of the principle of virtual displacements as follows:

$$\begin{aligned}
 M_{xx,x} + M_{xy,y} - Q_x &= \frac{\rho h^3}{12} \phi_{x,tt}, \\
 M_{xy,x} + M_{yy,y} - Q_y &= \frac{\rho h^3}{12} \phi_{y,tt}, \\
 Q_{x,x} + Q_{y,y} - \kappa w_0 + q &= \rho h w_{0,tt},
 \end{aligned} \tag{5.4}$$

where M_{xx} , M_{yy} , and M_{xy} are bending moments and Q_x , Q_y are transverse force resultants, defined as follows:

$$\begin{Bmatrix} M_{xx} \\ M_{yy} \\ M_{xy} \end{Bmatrix} = \mathbf{D} \{ \varepsilon_b \}, \quad \begin{Bmatrix} Q_y \\ Q_x \end{Bmatrix} = \mathbf{A} \{ \varepsilon_s \}. \tag{5.5}$$

κ is the force constant, q is the transverse load applied at top and bottom in plate, h is the thickness of plate. In the relations (5.5), the bending stiffness coefficients \mathbf{D} and the extensional stiffness coefficients \mathbf{A} are defined as

$$\mathbf{D} = \begin{bmatrix} D_{11} & D_{12} & 0 \\ D_{12} & D_{22} & 0 \\ 0 & 0 & D_{66} \end{bmatrix}, \quad \mathbf{A} = \begin{bmatrix} A_{44} & 0 \\ 0 & A_{55} \end{bmatrix}, \tag{5.6}$$

where

$$\begin{aligned}
 D_{11} &= \frac{E_1 h^3}{12(1 - \nu_{12}\nu_{21})}, & D_{12} &= \frac{\nu_{12} E_2 h^3}{12(1 - \nu_{12}\nu_{21})}, & D_{22} &= \frac{E_2 h^3}{12(1 - \nu_{12}\nu_{21})} \\
 D_{66} &= \frac{G_{12} h^3}{12}, & A_{44} &= G_{23} h, & A_{55} &= G_{13} h
 \end{aligned}$$

where E_i are Young's moduli, ν_{ij} are Poisson ratios, and G_{ij} is shear moduli.

For an isotropic plate, $E \equiv E_1 = E_2$ and $\nu \equiv \nu_{12} = \nu_{21}$ then (5.6) can be simplified

as follows:

$$\mathbf{D} = \frac{Eh^3}{12(1-\nu^2)} \begin{bmatrix} 1 & \nu & 0 \\ \nu & 1 & 0 \\ 0 & 0 & \frac{(1-\nu)}{2} \end{bmatrix}, \quad \mathbf{A} = \frac{k_s Eh}{2(1+\nu)} \begin{bmatrix} 1 & 0 \\ 0 & 1 \end{bmatrix}.$$

Using the relations (5.3), (5.5), and (5.6) and rewriting the Euler-Lagrange equations (5.4) in terms of the rotational displacements (5.2) , we obtain

$$\begin{aligned} D\left\{\phi_{x,xx} + \nu\phi_{y,yx} + \frac{(1-\nu)}{2}(\phi_{x,yy} + \phi_{y,xy})\right\} - Ah^{-2}(w_{0,x} + \phi_x) &= 0, \\ D\left\{\phi_{y,yy} + \nu\phi_{x,xy} + \frac{(1-\nu)}{2}(\phi_{x,yx} + \phi_{y,xx})\right\} - Ah^{-2}(w_{0,y} + \phi_y) &= 0, \\ -Ah^{-2}(w_{0,xx} + w_{0,yy} + \phi_{x,x} + \phi_{y,y}) &= q, \end{aligned} \quad (5.7)$$

where D is the scaled bending modulus, $E/[12(1-\nu^2)]$, $A = Ek_s/2(1+\nu)$, and k_s is the transverse shear correction factor.

5.1.2 Patchwise RPP approximation form

Patchwise RPPM is a partition of unity finite element method (PUFEM) which uses RPP shape functions as local approximation functions. In this section, we construct local basis functions by using RPP shape functions and PU functions with flat-top constructed in [51].

Let $\Omega \subseteq \mathbb{R}^2$ be a polygonal domain, and let $\delta > 0$ be a real number. Let $\{\Omega_i \mid i = 1, 2, \dots, N\}$ be a convex quadrangular partition of $E_\delta(\Omega)$, where $E_\delta(\Omega)$ is the δ -extension of Ω defined by

$$E_\delta(\Omega) = \bigcup_{\mathbf{x} \in \Omega_i} (\mathbf{x} + [-\delta, +\delta]^2).$$

Ω_i is called a patch. Note that the quadrangular patches Ω_i are allowed to be convex

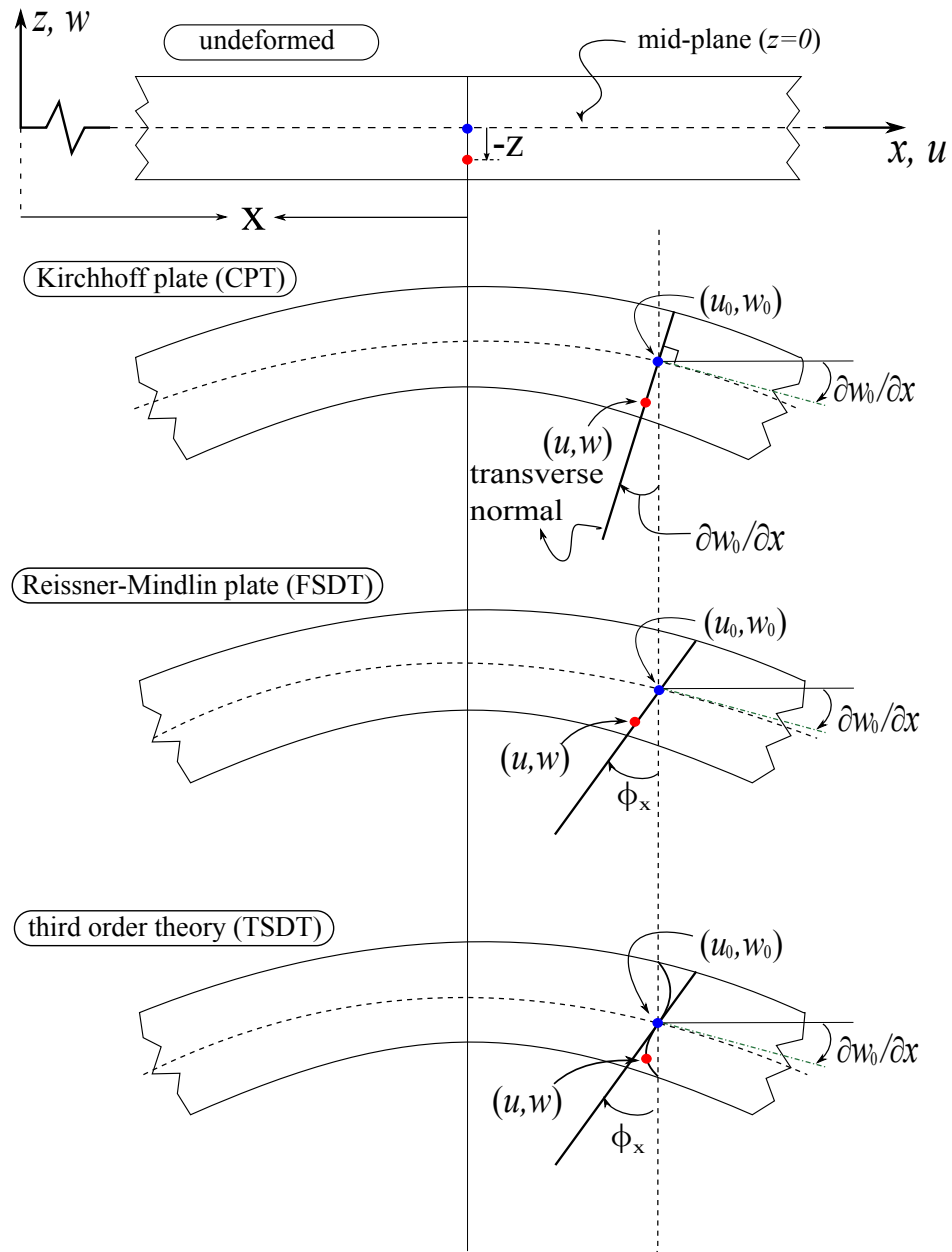


Figure 5.1: Deformation of a transverse normal according to Kirchhoff (classical), Reissner-Mindlin (first order), and third order plate theories

polygons, such as triangles, rectangles, non-rectangular quadrangles, pentagons, and so on.

For each $i = 1, 2, \dots, N$, denote $X_i = \{\mathbf{x}_{i_j} \in \mathbb{R}^2 \mid j \in \Lambda_i\}$ as the particles associated with the patch Ω_i . Note that the particles do not need to be in Ω_i . Let $\{\psi_{i_j} \mid j \in \Lambda_i\}$ be the set of C^r -piecewise polynomial shape functions corresponding to the particles \mathbf{x}_{i_j} .

Now we define the local approximation of the displacement filed as follows:

$$\begin{aligned} w(\mathbf{x}) &\approx w^{h_i}(\mathbf{x}) = \sum_{j=1}^n \Psi_i(\mathbf{x}) \psi_{i_j}(\mathbf{x}) d_{i_j}^{(1)}, \\ \phi_x(\mathbf{x}) &\approx \phi_x^{h_i}(\mathbf{x}) = \sum_{j=1}^n \Psi_i(\mathbf{x}) \psi_{i_j}(\mathbf{x}) d_{i_j}^{(2)}, \\ \phi_y(\mathbf{x}) &\approx \phi_y^{h_i}(\mathbf{x}) = \sum_{j=1}^n \Psi_i(\mathbf{x}) \psi_{i_j}(\mathbf{x}) d_{i_j}^{(3)}, \end{aligned} \quad (5.8)$$

for i -th patch Ω_i , where partition of unity with flat-top $\Psi_i(\mathbf{x})$ is the simple form of (2.13) in two-dimension.

Substituting (5.8) into the variational formulation obtained by Lagrange-Euler equations (5.7) with assumption of free vibration (i.e force vector is zero.), we can get the following matrix form

$$\mathbf{K}\mathbf{d} + \mathbf{M}\ddot{\mathbf{d}} = \mathbf{0}, \quad (5.9)$$

where

$$\mathbf{K} = \begin{bmatrix} [K_{11}] & [K_{12}] & [K_{13}] \\ [K_{12}] & [K_{22}] & [K_{23}] \\ [K_{13}] & [K_{23}] & [K_{33}] \end{bmatrix}, \quad \mathbf{M} = \begin{bmatrix} [M_{11}] & 0 & 0 \\ 0 & [M_{22}] & 0 \\ 0 & 0 & [M_{33}] \end{bmatrix}, \quad \text{and } \mathbf{d} = \begin{Bmatrix} \{d^{(1)}\} \\ \{d^{(2)}\} \\ \{d^{(3)}\} \end{Bmatrix}. \quad (5.10)$$

Note that $\ddot{\mathbf{d}}$ is the accelerations and submatrices $[K_{ij}]$ and $[M_{ii}]$ are symmetric.

Assuming the harmonic motion we obtain the natural frequencies and the modes of

vibration by solving the generalized eigenproblem [21]

$$(\mathbf{K} - \omega^2 \mathbf{M}) \mathbf{X} = \mathbf{0},$$

where ω is the natural frequency and \mathbf{X} the mode of vibration.

For buckling of plate models, the strain energy for in-plane pre-buckling stresses $\hat{\sigma}_x, \hat{\sigma}_y, \hat{\sigma}_{xy}$ without considering external forces is the following:

$$\begin{aligned} U = & \frac{1}{2} \int_{\Omega} \varepsilon_b^T \mathbf{D} \varepsilon_b dx dy + \frac{1}{2} \int_{\Omega} \varepsilon_s^T \mathbf{A} \varepsilon_s dx dy + \frac{1}{2} \int_{\Omega} [w_{0,x} \ w_{0,y}] \hat{\sigma}^0 \begin{Bmatrix} w_{0,x} \\ w_{0,y} \end{Bmatrix} dx dy \\ & + \frac{1}{2} \int_{\Omega} [\phi_{x,x} \ \phi_{x,y}] \hat{\sigma}^0 \begin{Bmatrix} \phi_{x,x} \\ \phi_{x,y} \end{Bmatrix} dx dy + \frac{1}{2} \int_{\Omega} [\phi_{y,x} \ \phi_{y,y}] \hat{\sigma}^0 \begin{Bmatrix} \phi_{y,x} \\ \phi_{y,y} \end{Bmatrix} dx dy, \quad (5.11) \end{aligned}$$

where

$$\hat{\sigma}^0 = \begin{bmatrix} \hat{\sigma}_x & \hat{\sigma}_{xy} \\ \hat{\sigma}_{xy} & \hat{\sigma}_{yy} \end{bmatrix}.$$

We can rewrite the strain energy (5.11) as the following matrix form

$$\mathbf{Kd} + \lambda \mathbf{G} = \mathbf{0},$$

where \mathbf{K} is the global stiffness matrix defined in (5.10),

$$\mathbf{G} = \begin{bmatrix} [G_{11}] & 0 & 0 \\ 0 & [G_{22}] & 0 \\ 0 & 0 & [G_{33}] \end{bmatrix},$$

which is called geometrical stiffness matrix and λ is a constant by which the in-plane loads must be multiplied to cause buckling. Thus the buckling loads can be found by solving the eigenproblem in (5.9).

5.2 Numerical results

In order to show the effectiveness of the proposed meshfree method, we observe Reissner-Mindlin plates in bending, vibration, and buckling by means of the patchwise RPPM. Also, the comparison of our numerical results with other results are described in the following subsections.

5.2.1 A square Reissner-Mindlin plate in bending

One can compare the approximate solutions obtained by the patchwise RPPM with conventional FEM using quadratic basis functions to see the effectiveness of the patchwise RPPM over FEM for the square Reissner-Mindlin plate in bending. To this end, we consider a simply-supported and clamped square plates (side $a = 1$) under uniform transverse pressure ($q = 1$), and thickness h . Other properties of the material are employed by ([21]). The non dimensional transverse displacement is set as

$$\hat{w} = w_{\max} D / qa^4,$$

where D is the flexural rigidity, w_{\max} is the absolute maximum value of transverse deflection and it occurs at center point in this problem. The numerical results in Table 5.1 show that RPPM is highly effective than conventional FEM even though we use less DOF for bending problem. Note that SSSS (CCCC) means that simply (clamped) supported boundary conditions are imposed along four sides of the square Reissner-Mindlin plate.

It verifies that the maximum transverse displacement w_{\max} occurs at the center of the plate as shown in Fig. 5.2(a). Moreover, the rotational displacement ϕ_y is zero at the pair of two edges corresponding to the lines $y = 0$ and $y = 1$ because of the simply supported boundary conditions as shown in Fig. 5.2(b). In Fig. 5.2(c), twisting moment M_{xy} is shown in skew-symmetric form because of the simply supported

boundary conditions.

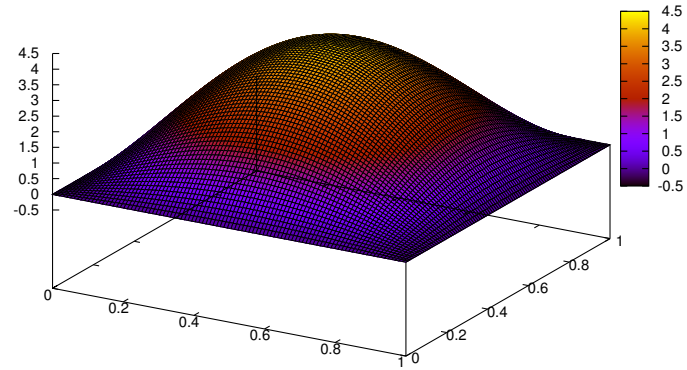
Table 5.1: non dimensional transverse displacement \hat{w} of a square Reissner-Mindlin plate for two different ratios of a/h and boundary conditions under uniform transverse pressure ($q = 1$). \hat{w}_k means RPP approximate solution with order of RPP k . Exact solutions, \hat{w}_{exact} 's are Navier solutions with 1000×1000 terms for each solutions [60].

a/h		10		20	
\hat{w}	DOF	SSSS	CCCC	SSSS	CCCC
\hat{w}_2	36	0.00404664880	0.000511155881	0.00355041532	0.00150427733
\hat{w}_4	100	0.00427089918	0.00150075015	0.00405976679	0.00125712238
\hat{w}_6	196	0.00427187070	0.00150406450	0.00406142190	0.00126486890
\hat{w}_{FEM}	961	0.004271	0.001503	0.004060	0.001264
\hat{w}_{exact}	∞	0.004271866	0.00150	0.004061413	0.001260

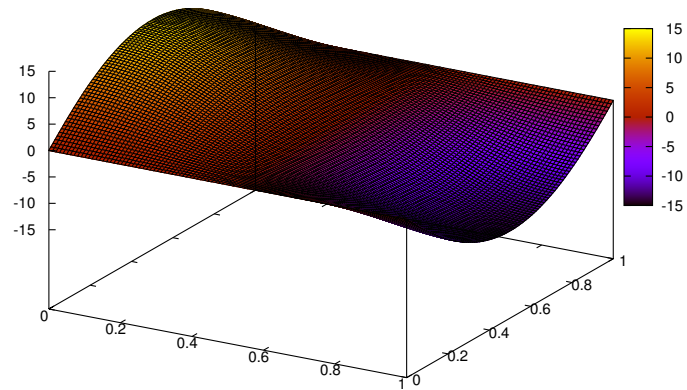
5.2.2 Reissner-Mindlin plates in free vibration and buckling

In this subsection, we demonstrate the effectiveness of the proposed meshfree method (RPPM) in deal with thick plates of various thickness-to-edge ratios for free vibration and buckling. The ratios, RPP order, correction factors, non flat-top areas of PU functions that are used for numerical tests are as follows:

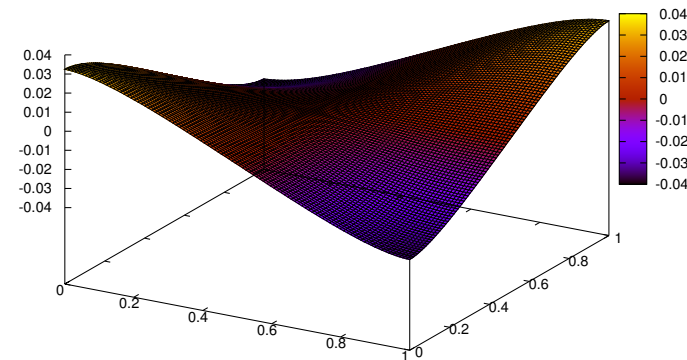
1. we consider a square plate with side a with various thickness-to-width ratios and boundary conditions in Tables 5.2 through 5.7, and a rectangular plate with side a and length b with various length-to-width ratios as well as thickness-to-width ratios in Table 5.8
2. we consider the Rayleigh-Ritz solutions as exact solutions [18, 32] in Tables 5.2, 5.3, and 5.8, and the Reissner-Mindlin solutions as exact solutions [26] in Tables 5.4 through 5.7
3. Thickness-to-edge, h/a is set 0.1 in Tables 5.2, 5.4, and 5.6, and 0.01 in Tables 5.3, 5.5, and 5.7.



(a) Deformed shape of the plate along the displacement w



(b) Deformed shape of the plate along the displacement ϕ_y



(c) Twisting moment M_{xy} of the plate

Figure 5.2: (a) Maximum deflection of transverse displacement w occurs at the center of the plate (b) The rotational displacement ϕ_y is zero at the pair of two edges corresponding to the lines $y = 0$ and $y = 1$ because of the simply supported boundary conditions (c) It occurs in skew symmetric for the twisting moment because of simply supported boundary conditions

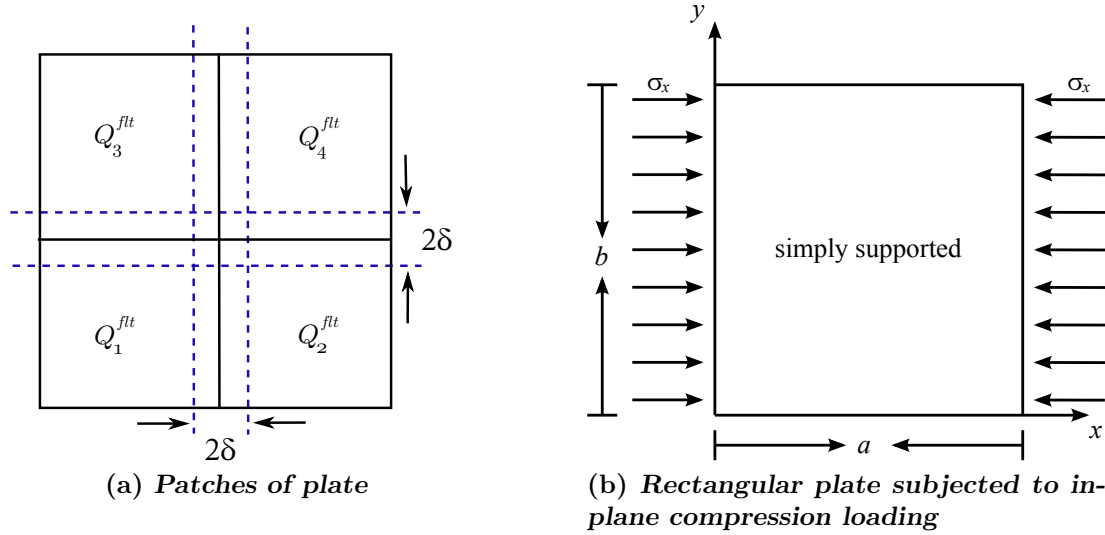


Figure 5.3: (a) Partition of rectangular plate into four patches (b) Simply supported rectangular plates subjected to uniaxial compression

4. we use the transverse shear correction factor, $k_s = 0.8601$ in Table 5.2, 0.833 in Tables 5.3 and 5.4, and 0.822 in Tables 5.5, 5.6 and 5.7.
5. In Tables 5.2 through 5.7, we use RPP order 6, and we use RPP order 4 in Table 5.8. Note that particle shape functions are product of Lagrange interpolation polynomials corresponding to particles x_0, \dots, x_n , n is an order of RPP shape functions.
6. we use four patches with $\delta = 0.05$ in all of Tables as shown in Fig. 5.3(a).

The non-dimensional natural frequency (or fundamental frequency parameter) is given by

$$\bar{\omega} = \omega_{mn} a \sqrt{\rho/G},$$

where ρ is the material density, $G = E/2(1 + \nu)$ is the shear modulus. m and n are the vibration half-waves in axes x and y , respectively.

In Tables 5.2 and 5.3, the clamped boundary conditions are imposed on all sides of the square Reissner-Mindlin plate (CCCC). With the clamped boundary conditions,

Table 5.2: Fundamental frequency parameters $\bar{\omega}_{mn}$ for a CCCC square Reissner-Mindlin plate with $h/a = 0.1$, $k_s = 0.8601$, $\nu = 0.3$

Method	FEM	RKPM	RPPM	Rayleigh-Ritz
DOF	441	289	196	.
Mode no. (m, n)				
1(1,1)	1.5955	1.5582	1.5910	1.594
2(2,1)	3.0662	3.0182	3.0390	3.039
3(1,2)	3.0662	3.0182	3.0390	3.039
4(2,2)	4.2924	4.1711	4.2627	4.265
5(3,1)	5.1232	5.1218	5.0255	5.035
6(1,3)	5.1730	5.1594	5.0731	5.078
7(3,2)	6.1587	6.0178	6.0808	.
8(2,3)	6.1587	6.0178	6.0808	.
9(4,1)	7.6554	7.5169	7.4204	.
10(1,4)	7.6554	7.5169	7.4204	.
11(3,3)	7.7703	7.7288	7.6814	.
12(4,2)	8.4555	8.3985	8.2671	.
13(2,4)	8.5378	8.3985	8.3426	.

Table 5.3: Fundamental frequency parameters $\bar{\omega}_{mn}$ for a CCCC square Reissner-Mindlin plate with $h/a = 0.01$, $k_s = 0.8601$, $\nu = 0.3$

Method	FEM	RKPM	RPPM	Rayleigh-Ritz
DOF	441	289	196	.
Mode no. (m, n)				
1(1,1)	0.175	0.1743	0.1753	0.1754
2(2,1)	0.3635	0.3576	0.3574	0.3576
3(1,2)	0.3635	0.3576	0.3574	0.3576
4(2,2)	0.5358	0.5240	0.5265	0.5274
5(3,1)	0.6634	0.6465	0.6401	0.6402
6(1,3)	0.6665	0.6505	0.6432	0.6402
7(3,2)	0.8266	0.8015	0.8020	.
8(2,3)	0.8266	0.8015	0.8020	.
9(4,1)	1.0875	1.0426	1.0317	.
10(1,4)	1.0875	1.0426	1.0317	.
11(3,3)	1.1049	1.0628	1.0681	.
12(4,2)	1.2392	1.1823	1.1820	.
13(2,4)	1.2446	1.1823	1.1872	.

Table 5.4: Fundamental frequency parameters $\bar{\omega}_{mn}$ for a SSSS square Reissner-Mindlin plate with $h/a = 0.1$, $k_s = 0.833$, $\nu = 0.3$

Method	FEM	RKPM	RPPM	3D solution	Mindlin solution
DOF	256	289	196	.	.
Mode no. (m, n)					
1(1,1)	0.9346	0.922	0.9302	0.932	0.930
2(2,1)	2.2545	2.205	2.2192	2.226	2.219
3(1,2)	2.2545	2.205	2.2192	2.226	2.219
4(2,2)	3.4592	3.377	3.4055	3.421	3.406
5(3,1)	4.3031	4.139	4.1493	4.171	4.149
6(1,3)	4.3031	4.139	4.1493	4.171	4.149
7(3,2)	5.3535	5.170	5.2054	5.239	5.206
8(2,3)	5.3535	5.170	5.2054	5.239	5.206
9(4,1)	6.9413	6.524	6.5237	.	6.520
10(1,4)	6.9413	6.524	6.5237	.	6.520
11(3,3)	7.0318	6.779	6.8338	6.889	6.834
12(4,2)	7.8261	7.416	7.4496	7.511	7.446
13(2,4)	7.8261	7.416	7.4496	7.511	7.446

two different thickness-to-edge ratios, 0.1 and 0.01 are considered. Also, the shear correction factor is taken as $k_s = 0.8601$. We compute the first thirteen modes of vibration for both the plates, and the non-dimensional natural frequencies computed by patchwise RPPM are compared with Rayleigh-Ritz solutions [17] for each plates in Tables 5.2 and 5.3. As you can see the modes from first to sixth in Tables 5.2 and 5.3, RPP solutions are the closest approximations to the Rayleigh-Ritz solutions comparing with other solutions, classical Finite Element solutions using quadrilateral elements [21] and RKP solutions [36] as a comparative numerical result. Moreover, it is worth noticing that the proposed method use much less number of degrees of freedom than the others.

In Tables 5.4 and 5.5, fully simply supported (SSSS) Reissner-Mindlin square plates with different thickness-to-edge ratios, 0.1 and 0.01 are considered. Also the shear correction factor is taken as $k_s = 0.833$. In similar to Table 5.2 and 5.3, first thirteen modes of vibration have been calculated. Our RPP solutions are compared with

Table 5.5: Fundamental frequency parameters $\bar{\omega}_{mn}$ for a SSSS square Reissner-Mindlin plate with $h/a = 0.01$, $k_s = 0.833$, $\nu = 0.3$

Method	FEM	RKPM	RPPM	Mindlin solution
DOF	441	289	196	.
Mode no. (m, n)				
1(1,1)	0.0965	0.0961	0.09628	0.09629
2(2,1)	0.2430	0.2419	0.24057	0.2406
3(1,2)	0.2430	0.2419	0.24057	0.2406
4(2,2)	0.3890	0.3860	0.38470	0.3848
5(3,1)	0.4928	0.4898	0.48077	0.4809
6(1,3)	0.4928	0.4898	0.48077	0.4809
7(3,2)	0.6380	0.6315	0.62463	0.6249
8(2,3)	0.6380	0.6315	0.62463	0.6249
9(4,1)	0.8550	0.8447	0.81910	0.8167
10(1,4)	0.8550	0.8447	0.81910	0.8167
11(3,3)	0.8857	0.8726	0.86410	0.8647
12(4,2)	0.9991	0.9822	0.96229	0.9605
13(2,4)	0.9991	0.9822	0.96229	0.9605

the 3-D elasticity solutions in Table 5.4 and analytical solutions given by Mindlin [26] in both Tables 5.4 and 5.5. The accuracy of our proposed method, patchwise RPPM is more agreeable than other two numerical results, FE solutions using quadrilateral elements [21] and RKP solutions [36] even though patchwise RPPM uses much less number of degrees of freedom than the others.

In Tables 5.6 and 5.7, the clamped and simply supported boundary conditions are imposed on each pairs of opposite sides in the square Reissner-Mindlin plates (SCSC) with the shear correction factor $k_s = 0.822$. RPP solutions are compared with Mindlin solutions [26], and we can see that our RPP solutions return better accuracy than the FE solutions [21].

In the buckling plate models, the non-dimensional buckling load intensity factor (or the critical buckling factor) is defined as

$$K_b = N_{cr} b^2 / (\pi^2 D),$$

Table 5.6: Fundamental frequency parameters $\bar{\omega}_{mn}$ for a SCSC square Reissner-Mindlin plate with $h/a = 0.1$, $k_s = 0.822$, $\nu = 0.3$

Method	FEM	RPPM	Mindlin solution
DOF	256	196	.
1(1,1) ^{Mode no.(m,n)}	1.2940	1.3001	1.302
2(2,1)	2.3971	2.3939	2.398
3(1,2)	2.9290	2.8845	2.888
4(2,2)	3.8394	3.8392	3.852
5(3,1)	4.3475	4.2314	4.237
6(1,3)	5.1354	4.9355	4.936
7(3,2)	5.5094	5.4575	.
8(2,3)	5.8974	5.7897	.
9(4,1)	6.9384	6.5584	.
10(1,4)	7.2939	7.2197	.
11(3,3)	7.7968	7.3062	.
12(4,2)	7.8516	7.5877	.
13(2,4)	8.4308	8.0734	.

Table 5.7: Fundamental frequency parameters $\bar{\omega}_{mn}$ for a SCSC square Reissner-Mindlin plate with $h/a = 0.01$, $k_s = 0.822$, $\nu = 0.3$

Method	FEM	RPPM	Mindlin solution
DOF	256	196	.
1(1,1) ^{Mode no.(m,n)}	0.1424	0.1411	0.1411
2(2,1)	0.2710	0.2667	0.2668
3(1,2)	0.3484	0.3376	0.3377
4(2,2)	0.4722	0.4604	0.4608
5(3,1)	0.5191	0.4977	0.4979
6(1,3)	0.6710	0.6279	0.6279
7(3,2)	0.7080	0.6820	.
8(2,3)	0.7944	0.7524	.
9(4,1)	0.8988	0.8313	.
10(1,4)	1.0228	0.9706	.
11(3,3)	1.0758	1.0069	.
12(4,2)	1.1339	1.0190	.
13(2,4)	1.2570	1.1442	.

Table 5.8: The critical buckling factors, K_b , of simply supported rectangular plates with different length-to-width ratios a/b , and thickness-to-width ratios, t/b , subjected to uniaxial compression

Method		RKPM(Uniform particles)	RPPM	P-ver. Ritz
DOF		289	100	.
a/b	h/b			
0.5	0.05	6.0405	6.0344	6.0372
	0.1	5.3116	5.4604	5.4777
	0.2	3.7157	3.9428	3.9963
1	0.05	3.9293	3.9437	3.9444
	0.1	3.7270	3.7809	3.7865
	0.2	3.1471	3.2353	3.2637
1.5	0.05	4.2116	4.2567	4.2570
	0.1	3.8982	4.0179	4.0250
	0.2	3.1032	3.2705	3.3048
2	0.05	3.8657	3.9441	3.9444
	0.1	3.6797	3.7813	3.7865
	0.2	3.0783	3.2356	3.2637
2.5	0.05	3.9600	4.1213	4.0645
	0.1	3.7311	3.9038	3.8638
	0.2	3.0306	3.2276	3.2421

where b is the edge length of the plate as shown in Fig. 5.3(b), N_{cr} the critical buckling load, and D the flexural rigidity. In Table 5.8, we consider a rectangular Reissner-Mindlin plate with simply supported on each edge as shown in Fig. 5.3(b). Also, three different thickness-to-width ratios, $h/b = 0.05, 0.1, 0.2$, and five width-to-length ratios, $a/b = 0.5, 1, 1.5, 2, 2.5$ are considered. Our results by the proposed method are compared with those of the Ritz method presented by Kitipornchai et al. [31] and RKPM with uniform particles [36], and details tabulated in Table 5.8. The results showed that the RPP solutions are more accurate than the solutions obtained by RKPM with much less number of degrees of freedom.

5.3 Reissner-Mindlin plate with boundary layer

In the small neighborhood of boundaries the solution computed from the Kirchhoff model can differ very substantially from the solutions computed from higher models. This substantially different behavior of solutions in the small neighborhood of the boundary is called the boundary layer effect or edge effect. Boundary layer effects are important from the point of view of engineering analysis, since the goal is often to determine moments and shear forces at the boundary, where the solutions corresponding to various plate models can differ very significantly. For the Reissner-Mindlin plate model, the transverse displacement variable does not exhibit any edge effect, but the rotation vector exhibits a boundary layer for all the boundary value problems which are hard and soft clamped plates, hard and soft simply supported plates, and free plates. In particular, edge effect is strongest for the soft simply supported and free plates, weakest for the soft clamped plates [2, 48].

5.3.1 Reissner-Mindlin Model with Boundary Layer on semi-infinite Plate

Consider one of examples in [2], that is, the Reissner-Mindlin model of a semi-infinite plate which occupies the half space $y > 0$ loaded by $q = c_0 \cos(x/L)$ where L

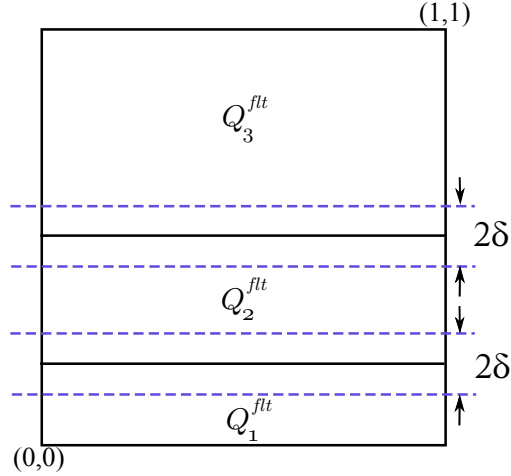


Figure 5.4: Partition of of rectangular plate into three patches

is the length of the side along x -axis, c_0 is a constant.

To capture the edge effect on the boundary layer around $y = 0$, we employ B-spline basis functions with three patch patchwise RPPM as shown in Fig. 5.4 and apply the following Shishkin type knot refinement:

$$\Xi_\xi = \{\underbrace{0, \dots, 0}_{p_\xi+1}, \xi_1, \dots, \xi_{n_\xi}, \underbrace{1, \dots, 1}_{p_\xi+1}\} \text{ and } \Xi_\eta = \{\underbrace{0, \dots, 0}_{p_\eta+1}, \eta_1, \dots, \eta_{n_\eta}, \underbrace{1, \dots, 1}_{p_\eta+1}\},$$

where $\xi_i = 1 - (n_\xi + 1 - i) \frac{0.5hp_\xi}{n_\xi}$, $\eta_j = j \frac{0.5hp_\eta}{n_\eta}$, and $h = 0.01$ is the thickness of the plate. At the Table 5.9, the coefficients c_1, c_2, c_3, c_4 , which are defined for various boundary conditions below and $\gamma = \sqrt{12k_s + (h/L)^2}$. Although this is a very special problem, it illustrates well the boundary layer effects for cases where the boundary and the loading are smooth.

In Tables 5.10 and 5.11, we reduce the domain into $[0, 1] \times [0, 1]$, and increase both the degree of B-spline and number of knots inserted up to 8. Soft simply supported boundary condition and free boundary condition on which edge effect strongly occurs, is imposed in Tables 5.10 and 5.11, respectively. As we expect that, the patchwise RPPM gives us good computational solutions with large rate of convergence. The

Table 5.9: Solution of the Reissner-Mindlin model of the semi-infinite plate problem with $q = c_0 \cos(x/L)$ ([2])

$w = \frac{c_0 L^6}{h^3} \left[\frac{h^3}{D_{11} L_2} + \frac{h^2}{k_s G L^4} + c_1 e^{-y/L} + c_2 \left(\frac{2D_{11}}{k_s G L_2 h} + \frac{y}{L} \right) e^{-y/L} - c_3 \frac{h^2 e^{-y/L}}{k_s G L^4} \right] \cos(x/L)$	
$\phi_x = \frac{c_0 L^5}{h^3} \left[-\frac{h^3}{D_{11} L_2} - c_1 e^{-y/L} - c_2 \frac{y}{L} e^{-y/L} + c_3 \frac{h^2 e^{-y/L}}{k_s G L^4} - c_4 \frac{\gamma h e^{-\gamma y/d}}{k_s G L^3} \right] \sin(x/L)$	
$\phi_y = \frac{c_0 L^5}{h^3} \left[-c_1 e^{-y/L} + c_2 \left(1 - \frac{y}{L} \right) e^{-y/L} + c_3 \frac{h^2 e^{-y/L}}{k_s G L^4} - c_4 \frac{h^2 e^{\gamma y/L}}{k_s G L^4} \right] \cos(x/L)$	
hard clamped	$c_1 = -h^3/(D_{11} L_2)$
	$c_2 = \{-\gamma k_s G h^3/D_{11} - \gamma(h/L)^2 + (h/L)^3\}/f$
	$c_3 = -\gamma k_s G L_2/f$
	$c_4 = -k_s G h L/f$
	$f = \gamma k_s G L_2 + 2\gamma D_{11}/h - 2D_{11}/L$
hard simply supported	$c_1 = -h^3/(D_{11} L_2)$
	$c_2 = -h^3/(2D_{11} L_2)$
	$c_3 = 0$
	$c_4 = 0$
soft simply supported	$c_1 = -h^3/(D_{11} L_2)$
	$c_2 = [2\gamma k_s G \nu h^4/(D_{11} L) + (h/L - \gamma)^2 \{k_s G h^3/D_{11} + (1 - \nu)(h/L)^2\}]/(2f)$
	$c_3 = -\gamma k_s G L h(1 - \nu)/f$
	$c_4 = -k_s G h^3 \{k_s G L_2 + D_{11}(1 - \nu)/h\}/(D_{11} f)$
	$f = -k_s G L_2(\gamma^2 + (h/L)^2) + (1 - \nu)(h/L) \{\gamma k_s G L_2 - (D_{11} L/h^2)(\gamma - h/L)^2\}$
free	$c_1 = \nu \{k_s G h^3/D_{11} - (\gamma^2 + (h/L)^2)\}/f$
	$c_2 = k_s G \nu h^3/(D_{11} f)$
	$c_3 = 0$
	$c_4 = 2k_s G \nu L_2/f$
	$f = -2k_s G L_2 + (1 - \nu) \{k_s G L_2 - (D_{11} L_2/h^3)(\gamma - h/L)^2\}$

Table 5.10: Absolute maximum norm error of displacement field (w_0, ϕ_x, ϕ_y) and energy norm error with soft simply supported boundary condition. B-splines with Shishkin type knot refinement are employed.

Order	DOF	$\ w_0 - w_0^h\ _{L_\infty}$	$\ \phi_x - \phi_x^h\ _{L_\infty}$	$\ \phi_y - \phi_y^h\ _{L_\infty}$	$\ \mathcal{U} - \mathcal{U}^h\ _{\text{Energ}}$
2	27	3.404E+01	3.055E+02	2.717E+02	1.735E+02
3	75	1.114E+01	6.591E+01	3.838E+01	2.363E+01
4	147	6.170E-01	3.653E+00	4.049E+00	1.895E+00
5	243	2.781E-02	2.845E-01	2.894E-01	8.748E-02
6	363	1.105E-03	1.732E-02	1.492E-02	5.057E-03
7	507	3.922E-05	3.879E-03	5.223E-04	2.955E-04
8	675	1.461E-06	8.574E-04	2.533E-05	7.127E-05
comparison of exact energy, \mathcal{U} , with approximate energy, \mathcal{U}^h at $p = 8$					
		\mathcal{U}		881.69482301964786	
		\mathcal{U}^h		881.69482302472773	

reason that we use B-spline functions instead of Lagrange interpolation functions, is that because we expect that B-splines work more stably than Lagrange interpolation functions on the boundary layer due to the property of variation diminishing.

Table 5.11: Absolute maximum norm error in displacement field (w_0, ϕ_x, ϕ_y) and absolute energy norm error with free boundary condition. B-splines with Shishkin type knot refinement are employed.

Order	DOF	$\ w_0 - w_0^h\ _{L_\infty}$	$\ \phi_x - \phi_x^h\ _{L_\infty}$	$\ \phi_y - \phi_y^h\ _{L_\infty}$	$\ \mathcal{U} - \mathcal{U}^h\ _{\text{Enrg}}$
2	27	1.112E+02	8.202E+02	5.504E+02	4.470E+02
3	75	2.052E+01	2.067E+02	5.934E+01	5.784E+01
4	147	5.711E-01	5.089E-00	2.526E-00	1.896E-00
5	243	2.720E-02	4.347E-01	3.363E-01	1.372E-01
6	363	6.761E-04	1.559E-02	9.077E-03	5.992E-03
7	507	2.883E-05	2.369E-03	3.544E-04	2.834E-03
8	675	5.252E-07	4.444E-04	2.318E-05	4.185E-03
comparison of exact energy, \mathcal{U} , with approximate energy, \mathcal{U}^h at $p = 8$					
\mathcal{U}				4370.3953408155621	
\mathcal{U}^h				4370.3953232942567	

CHAPTER 6: CONCLUDING REMARKS AND FUTURE CHALLENGES

We have shown numerical tests that mapping techniques using NURBS geometrical mappings constructed by a unconventional choice of control points are effective for numerical solutions of elliptic boundary value problems containing singularities. The mapping method was extended to the enrichment of IGA. Furthermore, the mapping technique was combined with IGA through partition of unity. The numerical results by enriched IGA demonstrate that the approach is effective to deal with elliptic boundary value problems containing singularities. Salient feature of this enrichment approach is that it does not altering design mappings, hence there is no restriction on refinements in IGA.

Even though the proposed mapping technique was only tested to the Poisson equation and elasticity with hypothetical solution containing one singularity, the method can be easily implemented in fracture mechanics of elastic media containing multiple singularities. Especially, engineers are interested in interacting cracks to capture the behavior of singularities and observe the change of stress field between two interacting cracks with respect to the interval of two cracks.

One of examples is an annular plate containing parallel radial cracks originating from one of the boundaries of the plate which is subjected to a prescribed loading.

On the other hands, singular functions built in the proposed mapping technique are in a C^0 approximation space, thus it is not available to apply fourth order PDEs such as Kirchhoff plate theory, and thin shells with Kirchhoff-Love assumptions. One future challenge work is to develop a new numerical method to generate singular functions in a C^1 approximation space.

Also, we expect that the mapping techniques presented to deal with 2D singularities in this dissertation can also be extended to the isogeometric analysis of 3D elasticity problems containing singularities by a similar manner to the 3-dimensional method of auxiliary mapping presented in [33].

In this dissertation, we proposed the patchwise Reproducing Polynomial Particle Method to compute the non-dimensional transverse displacement \hat{w} , natural frequency $\bar{\omega}_{mn}$, buckling load intensity factor K_b , and boundary layer problem on infinity domain. All numerical results have been compared with computed solutions by FEM and RKP, and analytical solutions except for the boundary layer problem. They have shown us that RPP approximate solutions are highly effective than other numerical methods. Moreover, the proposed method has achieved accurate solutions with less computational work. These features make the RPPM appealing to obtaining the promising performance on thick plates which have various geometric configuration such as circular, skew or triangular plates. It will be considered in future work.

Another popular topic in solid mechanics is the shell theories. Shells have all the characteristics of plates, along with an additional one curvature. The curvature could be chosen as the primary classifier of a shell because a shell's behavior under an applied loading is primarily governed by curvature. For thin shells based on classical linear elasticity, Kirchhoff-Love assumptions are usually applied. Also the force and moment equilibrium for the shell element results the set of the differential equations of static equilibrium of a shell element of the general theory of thin elastic shells ([67]). The set is coupled system of differential equations in terms of stresses. The governing equations about the membrane forces are second order, about the bending moments are third order, and twist moments are fourth order of differential equations. In order to analyze the behavior of shell material, conventional finite element methods are employed. But it is difficult to construct highly smooth approximation functions as well as generation of meshes in the method. However, patchwise RPPM has no

problem to construct highly smooth trial functions, applying the patchwise RPPM to the shell theory to approximate membrane forces, bending moments, and twist moments could yield accurate analysis of shells.

REFERENCES

- [1] M. Arad, Z. Yosibash, G. Ben-Dor, and A. Yakhot, *Computing flux intensity factors by a boundary method for elliptic equations with singularities*, Communications in Numerical Methods in Engineering **14** (1998), 657–670.
- [2] D.N. Arnold and R.S. Falk, *Edge effects in the reissner-mindlin plate theory*, Analytic and Computational Models of Shells, A.S.M.E., December 1989.
- [3] S. Atluri and S. Shen, *The meshless method*, Tech Science Press, 2002.
- [4] S. N. Atluri and T. Zhu, *A new meshless local petrov-galerkin (MLPG) approach in computational mechanics*, Computational Mechanics **22** (1998), 117–127.
- [5] I. Babūška, U. Banerjee, and J. E. Osborn, *Survey of meshless and generalized finite element methods: A unified approach*, Acta Numerica, Cambridge Press, 2003.
- [6] I. Babūška, U. Banerjee, and J.E. Osborn, *On the approximability and the selection of particle shape functions*, Numer. math **96** (2004), 601–640.
- [7] I. Babūška and H.-S. Oh, *The p-version of the finite element method for domains with corners and for infinite domains*, Numerical Methods for Partial Differential Equations **6** (1990), 371–392.
- [8] Y. Bazilevs, L. Beirao Da Veiga, J.A. Cottrell, T.J.R. Hughes, and G. Sangalli, *Isogeometric analysis: Approximation, stability and error estimates for h-refined meshes*, Mathematical Models and Methods in Applied Sciences **16** (2006), 1031–1090.
- [9] T. Belytschko and T. Black, *Elastic crack growth in finite elements with minimal remeshing*, International Journal for Numerical Methods in Engineering **45** (1999), 601–620.
- [10] T. Belytschko, Y. Y. Lu, and L. Gu, *Element-free galerkin methods*, International Journal for Numerical Methods in Engineering **37** (1994), 229–256.
- [11] T. Belytschko, D. Organ, and Y. Krongauz, *A coupled finite element-element-free galerkin method*, Comput. Mech. **17(3)** (1995), 186–195.
- [12] D. J. Benson, Y. Bazilevs, E. De Lucker, M. C. Hsu, T.J.R. Hughes, and T. Belytschko, *A generalized finite element formulation for arbitrary basis functions: From isogeometric analysis to XFEM*, International Journal for Numerical Methods in Engineering **83(6)** (2010), 765–785.
- [13] C.W. Bert and M. Malik, *The differential quadrature method for irregular domains and application to plate vibration*, International Journal of Mechanical Sciences **38(6)** (1996), 589–606.

- [14] S. Brenner and R. Scott, *The mathematical theory of finite element methods*, Springer, 1994.
- [15] P.G. Ciarlet, *Basic error estimates for elliptic problems*, North-Holland, 1991.
- [16] J.A. Cottrell, T.J.R. Hughes, and Y. Bazilevs, *Isogeometric analysis: Toward integration of CAD and FEM*, 2009.
- [17] D.J. Dawe and O.L. Roufaeil, *Rayleigh-ritz vibration analysis of mindlin plates*, Journal of Sound and Vibration **45(1)** (1980), 113–120.
- [18] ———, *Rayleigh-ritz vibration analysis of mindlin plates*, J. of Sound & Vibration **69(3)** (1980), 345–359.
- [19] D.J. Dawe and S. Wang, *Spline finite strip analysis of the buckling and vibration of rectangular composite laminated plates*, International Journal of Mechanical Sciences **37(6)** (1995), 589–606.
- [20] C.A. Duarte and J.T. Oden, *An hp adaptive method using clouds*, Computer methods in App. Mech. Engrg **139** (1996), 237–262.
- [21] A.J.M. Ferreira, *Matlab codes for finite element analysis (solids and structures)*, Springer, 2009.
- [22] M. Griebel and M.A. Schweitzer, *Meshfree methods for partial differential equations I, Lect. notes in compu. science and engr.*, Springer **57** (2003).
- [23] ———, *Meshfree methods for partial differential equations II, Lect. notes in compu. science and engr.*, Springer **43** (2005).
- [24] ———, *Meshfree methods for partial differential equations III, Lect. notes in compu. science and engr.*, Springer **26** (2007).
- [25] W. Han and X. Meng, *Error analysis of reproducing kernel particle method*, Comput. Meth. Appl. Mech. Engrg. **190** (2001), 6157–6181.
- [26] E. Hinton, *Numerical methods and software for dynamic analysis of plates and shells*, Pineridge Press, Swansea, 1988.
- [27] T.J.R. Hughes, J.A. Cottrell, T.J.R. Hughes, and Y. Bazilevs, *Isogeometric analysis: CAD, finite elements, NURBS, exact geometry and mesh refinement*, Comput. Methods Appl. Mech. Engrg. **194** (2005), 4135–4195.
- [28] T.J.R. Hughes and J.A. Evans, *Ices report 10-18, the institute for computational engineering and sciences*, 2010.
- [29] J. W. Jeong, H.-S. Oh, S. Kang, and H. Kim, *Mapping techniques in isogeometric analysis for elliptic boundary value problems containing singularities*, Comput. Methods Appl. Mech. Engrg. **254** (2013), 334–352.

- [30] J.W. Jeong, H.-S. Oh, S. Kang, and H. Kim, *Mapping techniques for isogeometric analysis of elliptic boundary value problems containing singularities*, Comput. Methods Appl. Mech. Engrg., <http://dx.doi.org/10.1016/j.cma.2012.09.009> (2012).
- [31] S. Kitipornchai, Y. Xiang, C.M. Wang, and K.M. Liew, *Buckling of thick skew plates*, International Journal for Numerical Methods in Engineering **36** (1993), 1299–1310.
- [32] Y. Xiang S. Kitipornchai K.M. Liew, C.M. Wang, *Vibration of mindlin plates*, Elsevier, Amsterdam, 1998.
- [33] S.J. Lee, H.-S. Oh, and J.H. Yun, *Extension of the method of auxiliary mapping for three-dimensional elliptic boundary value problems*, International Journal for Numerical Methods in Engineering **50** (2001), 1103–1129.
- [34] S. Li and W.K. Liu, *Meshfree particle methods*, Springer-Verlag, 2004.
- [35] S. Li, H. Lu, W. Han, W.K. Liu, and D.C.Jr. Simkins, *Reproducing kernel element method: Part II. globally conforming I^m/C^n hierarchies*, Computer Methods in App. Mech. and Engrg **193** (2004), 953–987.
- [36] K.M. Liew, J. Wang, T.Y. Ng, and M.J. Tan, *Free vibration and buckling analyses of shear-deformable plates based on FSDT meshfree method*, J. of Sound & Vibration **276** (2004), 997–1017.
- [37] K.M. Liew, Y. Xiang, and S. Kitipornchai, *Research on thick plate vibration: a literature survey*, Journal of Sound and Vibration **180(1)** (1995), 163–176.
- [38] G.R. Liu and X.L. Chen, *A mesh-free method for static and free vibration analyses of thin plates of complicated shape*, J. Sound and Vibration **241(5)** (2001), 839–853.
- [39] W.K. Liu, W. Han, H. Lu, S. Li, and J. Cao, *Reproducing kernel element method: Part I. theoretical formulation*, Computer Methods in App. Mech. and Engrg **193** (2004), 933–951.
- [40] W.K. Liu, S. Jun, and Y. F. Zhang, *Reproducing kernel particle methods*, International Journal for Numerical Methods in Fluids **20** (1995), 1081–1106.
- [41] W.K. Liu, S. Li, and T. Belytschko, *Moving least square reproducing kernel method part I: Methodology and convergence*, Computer Methods in Applied Mechanics and Engineering **143** (1997), 422–453.
- [42] W.K. Liu, S. Jun Liu, S. Li, J. Adee, and T. Belytschko, *Reproducing kernel particle methods for structural dynamics*, International Journal for Numerical Methods in Engineering **38** (1995), 1655–1679.

- [43] T.R. Lucas and H.-S. Oh, *The method of auxiliary mapping for the finite element solutions of elliptic problems containing singularities*, Journal of Computational Physics **108** (1993), 327–342.
- [44] E. De Lucker, D. J. Benson, T. Belytschko, Y. Bazilevs, and M. C. Hsu, *X-FEM in isogeometric analysis for linear fracture mechanics*, International Journal for Numerical Methods in Engineering **87(6)** (2011), 541–565.
- [45] E. De Luycker, D.J. Benson, T. Belytschko, Y. Bazilevs, and M.C. Hsu, *X-FEM in isogeometric analysis for linear fracture mechanics*, International Journal for Numerical Methethod **87** (2011), 541–565.
- [46] V.V. Meleshko, *Bending of an elastic rectangular clamped palte: Exact versus engineering solutions*, Journal of Elasticity **48** (1997), 1–50.
- [47] A.K. Noor, *Free vibrations of multilayered composite plates*, American Institute of Aeronautics and Astronautics Journal **11(7)** (1973), 1038–1039.
- [48] B. Szabó and I. Babūška, *Finite element analysis*, John Wiley, 1991.
- [49] H.-S. Oh and I. Babūška, *The method of auxiliary mapping for the finite element solutions of plane elasticity problems containing singularities*, Journal of Computational Physics **121** (1995), 193–212.
- [50] H.-S. Oh, C. Davis, G. Kim, and Y. Kwon, *Reproducing polynomial particle methods for boundary integral equations*, Computational Mechanics **48** (2011), 27–45.
- [51] H.-S. Oh and J. W. Jeong, *reproducing polynomial (singularity) particle methods and adaptive meshless methods for two-dimensional elliptic boundary value problems*, Comput. Methods Appl. Mech. Engrg. **198** (2009), 933–946.
- [52] H.-S. Oh and J.W. Jeong, *Almost everywhere partition of unity to deal with essential boundary conditions in meshless methods*, Compt. Meth. Appl. Mech. Eng. **198** (2009).
- [53] H.-S. Oh, J.W. Jeong, and W.T. Hong, *The generalized product partition of unity for the meshless methods*, J. Comp. Phy. **229** (2010), 1600–1620.
- [54] H.-S. Oh, J.W. Jeong, and J. G. Kim, *The reproducing singularity particle shape function for problems containing singularities*, Comput Mech **41** (2007), 135–157.
- [55] H.-S. Oh, J. G. Kim, and W.T. Hong, *The piecewise polynomial partition of unity shape functions for the generalized finite element methods*, Comput. Methods Appl. Mech. Engrg. **197** (2008), 3702–3711.
- [56] H.-S. Oh, J.G. Kim, and J.W. Jeong, *The closed form reproducing polynomial particle shape functions for meshfree particle methods*, Comput. Methods Appl. Mech. Engrg. **196** (2007), 3435–3461.

- [57] ———, *The smooth piecewise polynomial particle shape functions corresponding to patchwise non-uniformly spaced particles for meshfree particles methods*, Computational Mechanics **40** (2007), 569–594.
- [58] Les Piegl and Wayne Tiller, *The NURBS book, second edition*, Springer, 1995.
- [59] J.N. Reddy, *A review of refined theories of laminated composite plates*, The Shock and Vibration Digest **22(7)** (1990), 3–17.
- [60] ———, *Theory and analysis of elastic plates, second edition*, CRC Press, 2006.
- [61] J.N. Reddy and A.A. Khdeir, *Buckling and vibration of laminated composite plates using various plate theories*, American Institute of Aeronautics and Astronautics Journal **27(12)** (1989), 1808–1817.
- [62] D.F. Rogers, *An introduction to NURBS*, Academic Press, 2001.
- [63] T. Stroubolis, K. Copps, and I. Babuska, *Generalized finite element method*, Comput. Methods Appl. Mech. Engrg. **190** (2001), 4081–4193.
- [64] T. Stroubolis, L. Zhang, and I. Babuska, *Generalized finite element method using mesh-based handbooks: application to problems in domains with many voids*, Comput. Methods Appl. Mech. Engrg. **192** (2003), 3109–3161.
- [65] A. Tessler, E. Saether, and T. Tsui, *Vibration of thick laminated composite plates*, Journal of Sound and Vibration **179(3)** (1995), 475–498.
- [66] L. Beirao Da Veiga, D. Cho, and G. Sangalli, *Anisotropic NURBS approximation in isogeometric analysis*, Comput. Methods Appl. Mech. Engrg. **209-212** (2012), 1–11.
- [67] E. Ventsel and T. Krauthammer, *Thin plates and shells, theory, analysis, and applications*, Marcel Dekker Inc.
- [68] H. Zeng and C.W. Bert, *A differential quadrature analysis of vibration for rectangular stiffened plates*, Journal of Sound and Vibration **241(2)** (2001), 247–252.

APPENDIX A: TABLES OF NUMERICAL DATA

A.1 Numerical data (Tables A.1, A.2, A.3) for relative errors of the Motz problem shown in Fig. 4.3

A.2 Numerical data (Tables A.4, A.5, A.6) for relative errors of the Laplace equation in the cracked unit disk shown in Fig. 4.9

A.3 Numerical data (Tables A.7, A.8, A.9) for relative errors of the elasticity equation in the L -shaped domain shown in Fig. 4.11

Table A.1: The relative errors (%) of enriched IGA for the Motz problem: (i) The first column " $(p_{nurb}, \mathcal{C}^k)$ " stands for polynomial degree of NURBS for un-enriched IGA and the regularity of NURBS, respectively. For each k -refinement for IGA, only one knot is inserted. We use two patches for the Motz domain. (ii) The second column " p_{rich} " stands for the polynomial degree of B-spline functions in ξ as well as η for the enriched basis functions. (iii) The last row " ∞ " indicates the strain energy of the true solution.

$(p_{nurb}, \mathcal{C}^k)$	p_{rich}	DOF	$\ \text{Rel err}\ _{\infty}$	$\ \text{Rel err}\ _{L_2}$	$\ \text{Rel err}\ _{eng}$	Strain Energy
(2, 1)	2	33	2.793E-00	2.236E-00	8.756E-00	85731.6392270709
(3, 2)	3	60	4.226E-01	2.507E-01	1.857E-00	85108.6321954957
(4, 3)	4	95	1.114E-01	2.364E-02	5.299E-01	85081.6606970174
(5, 4)	5	138	2.418E-02	1.165E-02	1.981E-01	85079.6058077589
(6, 5)	6	189	6.603E-03	3.364E-03	4.685E-02	85079.2903129675
(7, 6)	7	248	1.209E-03	3.968E-04	1.360E-02	85079.2732083362
(8, 7)	8	315	5.381E-04	1.851E-04	5.758E-03	85079.2719146266
(9, 8)	9	390	1.201E-04	3.926E-05	1.485E-03	85079.2716512708
(10, 9)	10	473	3.246E-05	1.358E-05	4.192E-04	85079.2716339847
(11, 10)	11	564	9.934E-06	3.999E-06	1.426E-04	85079.2716326623
(12, 11)	12	663	2.168E-06	1.420E-06	5.283E-05	85079.2716325129
		∞				85079.2716324892

Table A.2: The relative errors (%) of un-enriched IGA for the Motz problem: The computed strain energy and their relative errors (%) of IGA of the Motz problem. The first column is the number of polynomial degree and the number of knot insertions with multiplicity 1 in the k -refinement of NURBS.

$p_{\xi} = p_{\eta}$	DOF	$\ \text{Rel err}\ _{\infty}$	$\ \text{Rel err}\ _{L_2}$	$\ \text{Rel err}\ _{eng}$	Strain Energy
2	36	6.591E-00	1.455E-00	1.379E+01	86697.267987072875
3	78	3.774E-00	6.424E-01	9.257E-00	85808.467637371214
4	136	2.352E-00	3.547E-01	6.915E-00	85486.130189526768
5	210	1.419E-00	2.219E-01	5.485E-00	85335.283067657336
6	300	8.322E-01	1.505E-01	4.525E-00	85253.507555096570
7	406	5.248E-01	1.080E-01	3.838E-00	85204.624317456488
8	528	4.114E-01	8.092E-02	3.324E-00	85173.276207700925
9	666	3.560E-01	6.261E-02	2.925E-00	85152.075681813716
10	820	3.297E-01	4.972E-02	2.607E-00	85137.127354482538
11	990	2.890E-01	4.033E-02	2.349E-00	85126.226913718347
12	1176	2.344E-01	3.330E-02	2.135E-00	85118.054847937659
	∞				85079.271632489165

Table A.3: The relative errors (%) of IGA with 5-radical mesh for the Motz problem: The computed strain energy obtained by the 5-radical mesh and their relative errors (%) of IGA of the Motz problem. The first column is the number of polynomial degree and the number of knot insertions with multiplicity 1 in the k -refinement of NURBS.

	DOF	$\ \text{Rel err}\ _\infty$	$\ \text{Rel err}\ _{L_2}$	$\ \text{Rel err}\ _{\text{eng}}$	Strain Energy
2	36	2.161E-00	0.860E-00	9.008E-00	85769.7665341624
3	78	0.850E-00	0.160E-00	3.932E-00	85210.8227268314
4	136	0.232E-00	4.291E-02	2.082E-00	85116.1462292704
5	210	0.118E-00	1.476E-02	1.223E-00	85092.0022359220
6	300	4.426E-02	5.628E-03	7.733E-01	85084.3600646084
7	406	1.900E-02	2.387E-03	5.176E-01	85081.5510467469
8	528	1.358E-02	1.115E-03	3.624E-01	85080.3887660094
9	666	4.027E-03	5.643E-04	2.631E-01	85079.8604302578
10	820	2.448E-03	3.053E-04	1.968E-01	85079.6011238803
11	990	1.767E-03	1.748E-04	1.509E-01	85079.4654907304
12	1176	1.022E-03	1.048E-04	1.183E-01	85079.3906139005
	∞				85079.2716324892

Table A.4: The relative errors (%) of enriched IGA: The computed strain energy and the relative errors (%) of the Laplace equation in the cracked unit disk. The entries of the first column are the polynomial degrees of NURBS and regularities at the only one inside knot in the k -refinement. The entries of the second column are the polynomial degrees of the B-spline functions in both variables for the enrichment functions.

$(p_{\text{nurb}}, \mathcal{C}^k)$	p_{rich}	DOF	$\ \text{Rel err}\ _\infty$	$\ \text{Rel err}\ _{L_2}$	$\ \text{Rel err}\ _{\text{eng}}$	Strain Energy
(2, 1)	2	43	3.410E-00	2.140E-00	1.020E+01	0.7935728795624198
(3, 2)	3	89	6.146E-01	2.757E-01	2.341E-00	0.7858286977505032
(4, 3)	4	151	1.477E-01	3.124E-02	6.644E-01	0.7854328358417727
(5, 4)	5	229	4.110E-02	8.615E-03	2.366E-01	0.7854025607948036
(6, 5)	6	323	6.664E-03	1.574E-03	5.135E-02	0.7853983705330601
(7, 6)	7	433	1.572E-03	5.171E-04	1.915E-02	0.7853981922177851
(8, 7)	8	559	6.069E-04	2.194E-04	7.923E-03	0.7853981683280771
(9, 8)	9	701	1.794E-04	7.485E-05	2.448E-03	0.7853981638683610
(10, 9)	10	859	6.416E-05	2.954E-05	8.115E-04	0.7853981634491797
(11, 10)	11	1033	1.676E-05	1.310E-05	2.917E-04	0.7853981634041332
(12, 11)	12	1223	5.797E-06	4.433E-06	1.087E-04	0.7853981633983763
		∞				0.7853981633974482

Table A.5: The relative errors (%) of un-enriched IGA: The computed strain energy and their relative errors (%) of IGA of the Laplace equation on the cracked unit disk. The first column is the number of polynomial degree and the number of knot insertions with multiplicity 1 in the k -refinement of NURBS.

	DOF	$\ \text{Rel err}\ _\infty$	$\ \text{Rel err}\ _{L_2}$	$\ \text{Rel err}\ _{\text{eng}}$	$\ u^h\ _{\text{eng}}^2$
2	85	8.004E-00	7.439E-01	1.000E+01	0.7932576910538956
3	175	5.809E-00	2.660E-01	6.002E-00	0.7882283850506779
4	297	4.611E-00	1.230E-01	4.018E-00	0.7866662238909883
5	451	3.851E-00	6.511E-02	2.834E-00	0.7860291895382055
6	637	3.324E-00	3.752E-02	2.045E-00	0.7857267687488737
7	855	2.937E-00	2.298E-02	1.472E-00	0.7855683849194441
8	1105	2.640E-00	1.480E-02	1.018E-00	0.7854796745154191
9	1387	2.405E-00	1.004E-02	6.123E-01	0.7854276164564003
10	1701	2.214E-00	7.251E-03	1.624E-01	0.7853960919858312
11	2047	2.056E-00	5.630E-03	5.234E-01	0.7853766418278368
12	2425	1.922E-00	4.713E-03	6.540E-01	0.7853645653712779
	∞				0.7853981633974482

Table A.6: The relative errors (%) of IGA with 5-radical mesh: The computed strain energy obtained by the 5-radical mesh and their relative errors (%) of IGA of the Poisson equation in the L -shaped domain. The first column is the number of polynomial degree and the number of knot insertions with multiplicity 1 in the k -refinement of NURBS.

	DOF	$\ \text{Rel err}\ _\infty$	$\ \text{Rel err}\ _{L_2}$	$\ \text{Rel err}\ _{\text{eng}}$	Strain Energy
2	85	1.731E-00	9.342E-01	7.557E-00	0.7898836109537649
3	175	4.895E-01	1.195E-01	2.520E-00	0.7858969275361544
4	297	1.801E-01	2.487E-02	1.091E-00	0.7854917128321975
5	451	1.032E-01	7.722E-03	5.477E-01	0.7854217287032445
6	637	6.512E-02	2.163E-03	3.075E-01	0.7854055945769168
7	855	4.396E-02	6.035E-04	1.897E-01	0.7854009906349790
8	1105	3.119E-02	1.976E-04	1.254E-01	0.7853993988363200
9	1387	2.301E-02	7.270E-05	8.729E-02	0.7853987618739750
10	1701	1.750E-02	2.984E-05	6.322E-02	0.7853984773736880
11	2047	1.365E-02	1.405E-05	4.727E-02	0.7853983389112305
12	2425	1.088E-02	7.482E-06	3.627E-02	0.7853982667252557
	∞				0.7853981633974482

Table A.7: The relative errors (%) of enriched IGA: The computed strain energy and the relative errors (%) of the Laplace equation in the L -shaped domain. The entries of the first column are the polynomial degrees of NURBS and regularities at the only one inside knot in the k -refinement. The entries of the second column are the polynomial degrees of the B-spline functions in both variables for the enrichment functions.

$(p_{\text{nurb}}, \mathcal{C}^k)$	p_{rich}	DOF	$\ \text{Rel err}\ _{\infty}$	$\ \text{Rel err}\ _{L_2}$	$\ \text{Rel err}\ _{\text{eng}}$	Strain Energy
(3, 2)	3	65	4.855E-01	3.545E-01	2.063E-00	0.918504156551838
(4, 3)	4	111	9.277E-02	6.677E-02	5.855E-01	0.918144814381293
(5, 4)	5	169	2.759E-02	9.854E-03	1.806E-01	0.918116326108197
(6, 5)	6	239	7.673E-03	3.961E-03	6.356E-02	0.918113701926983
(7, 6)	7	321	2.377E-03	1.103E-03	2.008E-02	0.918113367990180
(8, 7)	8	415	7.671E-04	4.651E-04	8.309E-03	0.918113337277383
(9, 8)	9	521	1.529E-04	1.148E-04	1.976E-03	0.918113331296302
(10, 9)	10	639	8.233E-05	5.165E-05	1.087E-03	0.918113331046222
(11, 10)	11	769	1.427E-05	9.837E-06	2.619E-04	0.918113330943880
(12, 11)	12	911	7.059E-06	3.549E-06	1.151E-04	0.918113330938800
		∞				0.918113330937581

Table A.8: The relative errors (%) of un-enriched IGA: The computed strain energy and their relative errors (%) of IGA of the Laplace equation on the L -shaped domain. The first column is the number of polynomial degree and the number of knot insertions with multiplicity 1 in the k -refinement of NURBS.

	DOF	$\ \text{Rel err}\ _{\infty}$	$\ \text{Rel err}\ _{L_2}$	$\ \text{Rel err}\ _{\text{eng}}$	$\ u^h\ _{\text{eng}}^2$
2	33	2.266E-00	2.909E-01	6.102E-00	0.921532725518123
3	85	1.171E-00	1.391E-01	3.576E-00	0.919287578474505
4	161	6.478E-01	6.710E-02	2.421E-00	0.918651789368805
5	261	3.141E-01	3.574E-02	1.777E-00	0.918403489767528
6	385	1.329E-01	2.201E-02	1.375E-00	0.918286985964129
7	533	8.510E-02	1.528E-02	1.104E-00	0.918225263709970
8	705	7.302E-02	1.131E-02	9.113E-01	0.918189588294503
9	901	5.178E-02	8.666E-03	7.685E-01	0.918167565476224
10	1121	4.966E-02	6.798E-03	6.593E-01	0.918153250947286
11	1365	4.485E-02	5.453E-03	5.737E-01	0.918143551777222
12	1633	3.370E-02	4.457E-03	5.050E-01	0.918136750938375
	∞				0.918113330937581

Table A.9: The relative errors (%) of IGA with 5-radical mesh: The computed strain energy obtained by the 5-radical mesh and their relative errors (%) of IGA of the Poisson equation in the L -shaped domain. The first column is the number of polynomial degree and the number of knot insertions with multiplicity 1 in the k -refinement of NURBS.

	DOF	$\ \text{Rel err}\ _{\infty}$	$\ \text{Rel err}\ _{L_2}$	$\ \text{Rel err}\ _{\text{eng}}$	Strain Energy
2	33	1.150E-00	2.452E-01	4.917E-00	0.920333431266857
3	85	3.508E-01	9.260E-02	1.601E-00	0.918348667387047
4	161	1.002E-01	4.326E-02	7.325E-01	0.918162601078802
5	261	3.991E-02	2.215E-02	3.701E-01	0.918125910923199
6	385	1.376E-02	1.227E-02	2.051E-01	0.918117196208557
7	533	5.854E-03	7.241E-03	1.218E-01	0.918114693701715
8	705	3.840E-03	4.489E-03	7.642E-02	0.918113867216142
9	901	9.885E-04	2.900E-03	5.016E-02	0.918113561971368
10	1121	5.718E-04	1.938E-03	3.420E-02	0.918113438382089
11	1365	4.613E-04	1.334E-03	2.412E-02	0.918113384367126
12	1633	1.294E-04	9.417E-04	1.744E-02	0.918113358893799
	∞				0.918113330937581

APPENDIX B: FIGURES OF NUMERICAL DATA

B.1 The wedge-shaped domain in Example 3.2.1

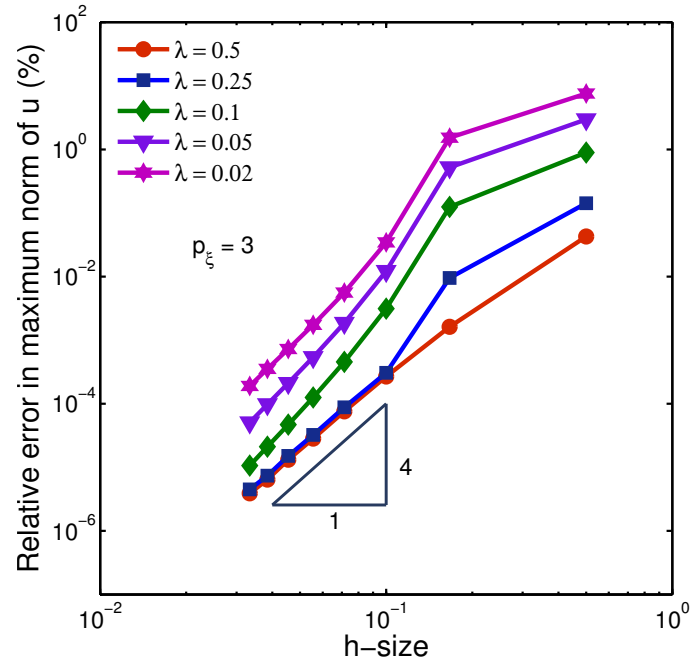


Figure B.1: Relative errors (%) in maximum norm of displacement u versus the h -sizes with various intensity factors and $p_\xi = 3$ fixed.

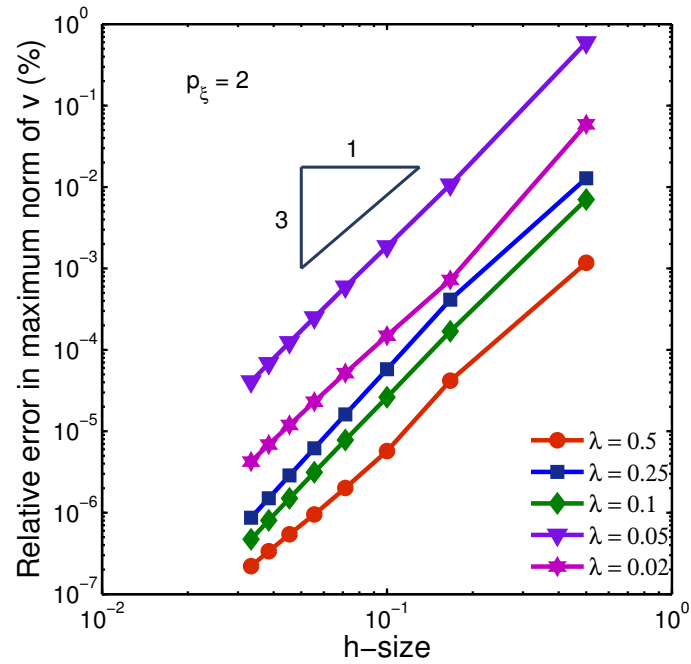


Figure B.2: Relative errors (%) in maximum norm of displacement v versus the h -sizes with various intensity factors and $p_\xi = 2$ fixed.

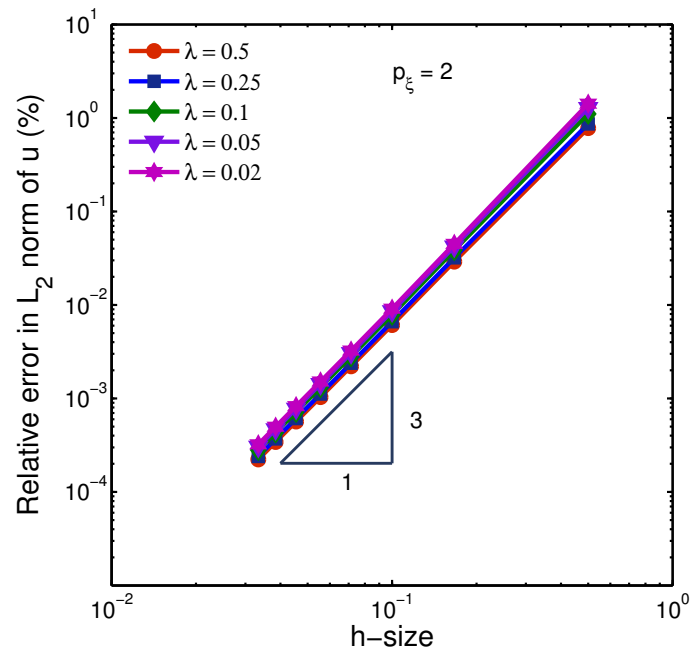


Figure B.3: Relative errors (%) in L_2 -norm of displacement u versus the h -sizes with various intensity factors and $p_\xi = 2$ fixed.

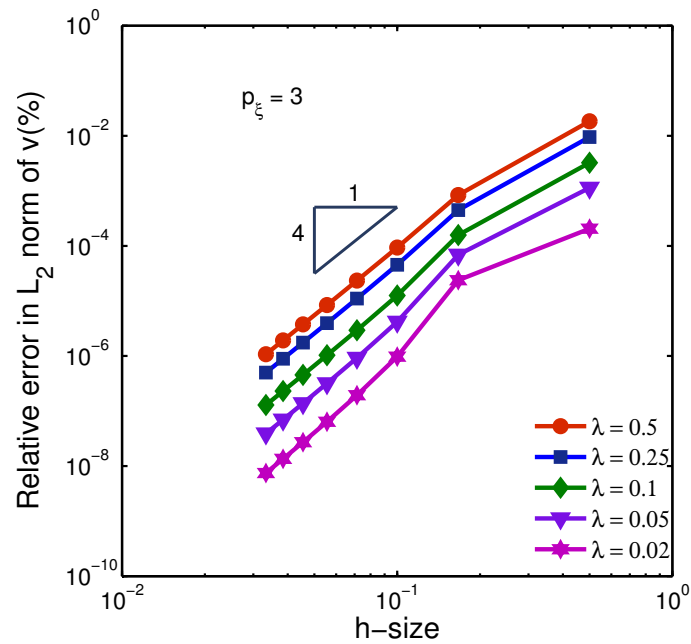


Figure B.4: Relative errors (%) in L_2 -norm of displacement v versus the h -sizes with various intensity factors and $p_\xi = 3$ fixed.

APPENDIX C: TABLES OF CONTROL POINTS AND WEIGHTS

C.1 The wedge-shaped domain in Example 3.2.1

C.2 The curved domain in Example 3.2.2

C.3 The single edge cracked domain in Example 3.2.3

We use the quadratic polynomials for the geometrical mapping because the intensity factor of the plate has $r^{\frac{1}{2}}\varphi(\theta)$. The control points and weights of the geometry in Example 3.2.3 are similar to that of Example 5.4 in [30]. In Table C.3, the control points $\mathbf{B}_{i,j}$ and corresponding weights $w_{i,j}$ for $j = 1, 3, 5$ are given. For the remaining control points and the weights, we use

$$\mathbf{B}_{i,1} = \mathbf{B}_{i,2} = (0, 0) \quad \text{and} \quad w_{i,1} = w_{i,2} = \begin{cases} 1 & \text{if } i \text{ is odd,} \\ w_0 & \text{if } i \text{ is even,} \end{cases}$$

$$\mathbf{B}_{i,4} = \frac{1}{2}(\mathbf{B}_{i,3} + 2\mathbf{B}_{i,5}) \quad \text{and} \quad w_{i,4} = w_{i,5} = 1.$$

Table C.1: Geometric setting for wedge-shaped domain $\Omega^{(\pm\alpha)}$ (Example 3.2.1). (a) The degree of polynomials and knot vectors for variables ξ and η , respectively. Note that there are $p + 1$ zeros and $p + 1$ ones are presented in the knot vector Ξ_η . (b) Control points and corresponding weights.

(a) <i>Knot vectors</i>			
variables	degrees	knot vectors	
ξ	$p_\xi = 2$	$\Xi_\xi = \{0, 0, 0, \frac{1}{2}, \frac{1}{2}, 1, 1, 1\}$	
η	$p_\eta = p$	$\Xi_\eta = \{0, \dots, 0, 1, \dots, 1\}$	

(b) <i>Control points and weights</i>							
i	j	$\mathbf{B}_{i,j}$	$w_{i,j}$	i	j	$\mathbf{B}_{i,j}$	$w_{i,j}$
1	$1, \dots, p$	$(0, 0)$	1	1	$p + 1$	$(\cos(\alpha), \sin(\alpha))$	1
2	$1, \dots, p$	$(0, 0)$	$\cos(\alpha/2)$	2	$p + 1$	$(1, \tan(\alpha/2))$	$\cos(\alpha/2)$
3	$1, \dots, p$	$(0, 0)$	1	3	$p + 1$	$(1, 0)$	1
4	$1, \dots, p$	$(0, 0)$	$\cos(\alpha/2)$	4	$p + 1$	$(1, -\tan(\alpha/2))$	$\cos(\alpha/2)$
5	$1, \dots, p$	$(0, 0)$	1	5	$p + 1$	$(\cos \alpha, -\sin \alpha)$	1

Table C.2: Geometric data to construct the NURBS mapping to deal with the elasticity containing singularity in the curved domain (Example 3.2.2). (a) The open knot vectors. (b) Control points and corresponding weights for $j = 1, 2, 3$. (c) Control points and corresponding weights for $j = 4, 5$. Here, $\beta = \tan(\pi/8)$ and $w_0 = \cos(\pi/8)$.

(a) *Knot vectors*

variables	degrees	knot vectors
ξ	$p_\xi = 2$	$\Xi_\xi = \{0, 0, 0, \frac{1}{4}, \frac{1}{4}, \frac{1}{2}, \frac{1}{2}, \frac{3}{4}, \frac{3}{4}, 1, 1, 1\}$
η	$p_\eta = 2$	$\Xi_\eta = \{0, 0, 0, \frac{1}{2}, \frac{1}{2}, 1, 1, 1\}$

(b) *Control points and weights for $j = 1, 2, 3$*

i	j	$\mathbf{B}_{i,j}$	$w_{i,j}$	i	j	$\mathbf{B}_{i,j}$	$w_{i,j}$	i	j	$\mathbf{B}_{i,j}$	$w_{i,j}$
1	1	(0,0)	1	1	2	(0,0)	1	1	3	(-1/2, 0)	1
2	1	(0,0)	w_0	2	2	(0,0)	w_0	2	3	(-1/2, $\beta/2$)	w_0
3	1	(0,0)	1	3	2	(0,0)	1	3	3	($-\sqrt{2}/4, \sqrt{2}/4$)	1
4	1	(0,0)	w_0	4	2	(0,0)	w_0	4	3	($-\beta/2, 1/2$)	w_0
5	1	(0,0)	1	5	2	(0,0)	1	5	3	(0, 1/2)	1
6	1	(0,0)	w_0	6	2	(0,0)	w_0	6	3	($\beta/2, 1/2$)	w_0
7	1	(0,0)	1	7	2	(0,0)	1	7	3	($\sqrt{2}/4, \sqrt{2}/4$)	1
8	1	(0,0)	w_0	8	2	(0,0)	w_0	8	3	(1/2, $\beta/2$)	w_0
9	1	(0,0)	1	9	2	(0,0)	1	9	3	(1/2, 0)	1

(c) *Control points and weights for $j = 4, 5$*

i	j	$\mathbf{B}_{i,j}$	$w_{i,j}$	i	j	$\mathbf{B}_{i,j}$	$w_{i,j}$
1	4	$\frac{1}{2}(\mathbf{B}_{1,3} + \mathbf{B}_{1,5})$	1	1	5	(-1, 0)	1
2	4	$\frac{1}{2}(\mathbf{B}_{2,3} + \mathbf{B}_{2,5})$	1.2	2	5	(-0.8, β)	1.2
3	4	$\frac{1}{2}(\mathbf{B}_{3,3} + \mathbf{B}_{3,5})$	1	3	5	(-1, 1)	1
4	4	$\frac{1}{2}(\mathbf{B}_{4,3} + \mathbf{B}_{4,5})$	1	4	5	($-\beta, 1.2$)	1
5	4	$\frac{1}{2}(\mathbf{B}_{5,3} + \mathbf{B}_{5,5})$	1	5	5	(0, 1)	1
6	4	$\frac{1}{2}(\mathbf{B}_{6,3} + \mathbf{B}_{6,5})$	1	6	5	($\beta, 0.8$)	1
7	4	$\frac{1}{2}(\mathbf{B}_{7,3} + \mathbf{B}_{7,5})$	1	7	5	(1, 1)	1
8	4	$\frac{1}{2}(\mathbf{B}_{8,3} + \mathbf{B}_{8,5})$	1.4	8	5	(1.6, β)	1.4
9	4	$\frac{1}{2}(\mathbf{B}_{9,3} + \mathbf{B}_{9,5})$	1	9	5	(1, 0)	1

Table C.3: Geometric setting for the single edge cracked plate (Example 3.2.3). (a) The degree of polynomials and knot vectors for variables ξ and η , respectively. (b) Control points and corresponding weights for $j = 1, 3, 5$. Here, $\beta = \tan(\pi/8)$ and $w_0 = \cos(\pi/8)$.

(a) *Knot vectors*

variables	degrees	knot vectors
ξ	$p_\xi = 2$	$\Xi_\xi = \{0, 0, 0, \frac{1}{8}, \frac{1}{8}, \frac{2}{8}, \frac{2}{8}, \frac{3}{8}, \frac{3}{8}, \frac{4}{8}, \frac{4}{8}, \frac{5}{8}, \frac{5}{8}, \frac{6}{8}, \frac{6}{8}, \frac{7}{8}, \frac{7}{8}, 1, 1, 1\}$
η	$p_\eta = 2$	$\Xi_\eta = \{0, 0, 0, \frac{1}{2}, \frac{1}{2}, 1, 1, 1\}$

(b) *Control points and weights for $j = 1, 3, 5$*

i	j	$\mathbf{B}_{i,j}$	$w_{i,j}$	i	j	$\mathbf{B}_{i,j}$	$w_{i,j}$	i	j	$\mathbf{B}_{i,j}$	$w_{i,j}$
1	1	(0,0)	1	1	3	(-1/2, 0)	1	1	5	(-1, 0)	1
2	1	(0,0)	w_0	2	3	(-1/2, $\beta/2$)	w_0	2	5	(-1, β)	1
3	1	(0,0)	1	3	3	($-\sqrt{2}/4, \sqrt{2}/4$)	1	3	5	(-1, 1)	1
4	1	(0,0)	w_0	4	3	($-\beta/2, 1/2$)	w_0	4	5	($-\beta, 1$)	1
5	1	(0,0)	1	5	3	(0, 1/2)	1	5	5	(0, 1)	1
6	1	(0,0)	w_0	6	3	($\beta/2, 1/2$)	w_0	6	5	($\beta, 1$)	1
7	1	(0,0)	1	7	3	($\sqrt{2}/4, \sqrt{2}/4$)	1	7	5	(1, 1)	1
8	1	(0,0)	w_0	8	3	(1/2, $\beta/2$)	w_0	8	5	(1, β)	1
9	1	(0,0)	1	9	3	(1/2, 0)	1	9	5	(1, 0)	1
10	1	(0,0)	w_0	10	3	(1/2, $-\beta/2$)	w_0	10	5	(1, $-\beta$)	1
11	1	(0,0)	1	11	3	($\sqrt{2}/4, -\sqrt{2}/4$)	1	11	5	(1, -1)	1
12	1	(0,0)	w_0	12	3	($\beta/2, -1/2$)	w_0	12	5	($\beta, -1$)	1
13	1	(0,0)	1	13	3	(0, -1/2)	1	13	5	(0, -1)	1
14	1	(0,0)	w_0	14	3	($-\beta/2, -1/2$)	w_0	14	5	($-\beta, -1$)	1
15	1	(0,0)	1	15	3	($-\sqrt{2}/4, -\sqrt{2}/4$)	1	15	5	(-1, -1)	1
16	1	(0,0)	w_0	16	3	(-1/2, $-\beta/2$)	w_0	16	5	(-1, $-\beta$)	1
17	1	(0,0)	1	17	3	(-1/2, 0)	1	17	5	(-1, 0)	1